UNIVERSIDAD COMPLUTENSE DE MADRID

FACULTAD DE CIENCIAS FÍSICAS

Departamento de Estructura de la Materia, Física Térmica y Electrónica

New developments of High Current Beam Profile Monitors for Ion Accelerators applied to Fusion Material Research
Nuevos desarrollos de Monitores de Perfil de Haces de Alta Corriente para Aceleradores de Iones aplicados a la investigación de Materiales de Fusión

UNIVERSIDAD
COMPLUTENSE
MADRID

Rodrigo Varela Alonso

Memoria para optar al grado de

Doctor en Física

Director

Ivan Podadera Aliseda

Madrid 2019

A quienes han hecho posible que pueda haber llegado hasta aquí

Acknowledgements

Abstract

Nowadays particle accelerators have become key instruments in many areas, ranging from material science to healthcare. As many more areas find in particle accelerators a suitable tool to fulfill their needs, they are becoming more specialized and adapted to produce new and more complicated particle beams. In the case of ion accelerators, the need of higher current and power beams in order to increase the production of secondary particles pushes the classical beam diagnostics to its limits. When measuring the beam profile in those high current and high power, interceptive diagnostics are unable to withstand the high power deposition and are destroyed.

In order to be able to measure and monitor the beam profile for high current beams, several indirect methods exist. In this work we will focus on the fluorescence light emitted by the excited particles of the residual gas. The following work starts with several introduction chapters to the subject, where theoretical and practical aspects of the Fluorescence Profile Monitor are discussed. After the introductory chapters, the results obtained during the LIPAc injector commissioning, where the profiles acquired with an intensified CID and a Doppler spectrometer are discussed and compared with the ones obtained with an Allison scanner. The topic is then shifted to the design of FPM for the high radiation areas of the high power deuteron beam accelerator DONES, as well as the design and results of an experiment required to evaluate the impact of different gases and lithium vapor in the measured profiles. Finally, a study of two different mechanisms of profile distortion is presented, with an special insight in the mechanisms of profile distortion due to the excited particle movement before the light emission took place.

Abstract

Actualmente los aceleradores de partículas se han convertido en instrumentos clave en diferentes áreas, desde la ciencia de materiales hasta la sanidad. Mientras muchas más disciplinas encuentran en ellos una herramienta adecuada a sus necesidades, ellos deben especializarse y adaptarse para producir nuevos y complicados haces de partículas. En el caso de los aceleradores de hadrones, la necesidad de mayores corrientes y potencias para incrementar la producción de partículas secundarias lleva a los diagnósticos clásicos a su límite. Cuando se mide el perfil del haz en esos aceleradores de alta corriente y potencia los diagnósticos interceptivos no son capaces de aguantar la elevada deposición de potencia y son destruidos.

Para poder ser capaces de medir y monitorizar el perfil del haz a alta corriente y potencia existen varios métodos indirectos. En este trabajo nos centraremos en la luz de fluorescencia emitida por las partículas del gas residual que son excitadas por el haz. El trabajo comienza con varios capítulos de introducción sobre la materia, donde se presentan los aspectos teóricos y prácticos de los Monitores de Perfil de Fluorescencia. Después de los capítulos de introducción se analizan las medidas obtenidas durante la puesta en marcha del inyector del acelerador LIPAc, donde los perfiles adquiridos con una cámara CID intensificada y un espectrómetro Doppler se discuten y se comparan con los obtenidos con un "Allison scanner". Después el objeto de la discusión se desplaza y nos centramos en el diseño de FPM para las áreas de elevada radiación del acelerador de deuterones de alta potencia DONES, además del diseño y los resultados obtenidos de un experimento realizado para evaluar el impacto de diferentes gases y vapor de litio en los perfiles adquiridos. Finalmente se ha presentado un estudio de dos mecanismos distintos de distorsión de perfil, con un énfasis especial en la distorsión del perfil del haz debido al movimiento de las partículas excitadas antes de que la emisión de luz se lleve a cabo.

Contents

List of Figures

List of Tables

Acronyms

Chapter 1

Particle Accelerators

1.1   Introduction

Since their beginning particles accelerators have become an indispensable tool in both research and development and in industry. From their birth more than hundred of years ago, they have evolved from simple DC machines that accelerate small currents of charged particles, to complex machines capable of deliver beams of high energy, high beam current and small size [11] . Although they started as a scientific tool to study the atomic nucleus, they have found many uses in other fields without abandoning its initial purposes. It is very common to find them in the medical field for medical imaging and therapy, or radioisotope production, in atom implanters and surface processing for the industry, in material studies, cargo inspection, ... [12]. However, the principles of the particles accelerators has remained unchanged: in a very basic model we can see the accelerators as a charged particle source, an acceleration system, the particle guiding elements, the ancillary systems and (in the majority of cases) a target where the particles collide.

As the only technical possibility to accelerate and guide charged particles is using electromagnetic fields [13], the primary division that we are going to make is based on the accelerated particle, thus we have to separate the electrons from the ions, both negative and positive ions in their different states of charges. Since their difference in mass they are obtained in very different ways: electrons are usually

extracted directly from metals by means of heating, lasers and field emission [14], whilst ions require a plasma [15]. There are also other accelerators that use other particles such as the muon, but they are not common and they are almost exclusively used for research.

The other difference that separates electron and ion machines is also derived from the difference of masses. The electron quickly becomes relativistic and the machines should take this into account, hence even if they are based in the same principles, the technical differences between electron and ions accelerators are very significant.

Going back to the simple model of accelerator, it is possible to make a classification based on the accelerating field. Unlike the electric field, magnetic field does not supply any work to the particles. Therefore, it is only possible to use the electric field to increase the energy of a charged particle. In the beginning, only DC fields were used due to their ease of use, but they limit the maximum energy to several hundreds of kV (although modern DC machines can reach few MV). One of the most important breakthroughs in accelerator technology was the use of RF fields in cavities to accelerate particles, which allowed the construction of higher energy machines or the miniaturization of existing ones. Nowadays we can find two accelerating schemes, the circular and the linear, depending on the particle trajectory. In circular accelerators the particle follows a circular path along the machine, with static or increasing magnetic field depending if we are in a cyclotron or a synchrotron. Meanwhile, in LINACs, particle follow a straight line crossing many RF cavities. In the present day novel accelerating schemes such as plasma or dielectric acceleration has been proposed as methods to replace RF cavities due to their capability to reach accelerating gradients several orders of magnitude higher, but they are still in phase of research and experimentation. Whilst not used for acceleration, magnetic fields are the key in guiding and focusing the charged particles along the machine. Magnets, both normal conducting and superconducting, make possible the travel of the particles from the source up to the target without (considerable) losses, and allow the shape manipulation of the beam profile.

And last but not least and often overlooked, both beam diagnostics and the ancillary systems (vacuum system, the water system, the control system...) integrate the previous systems together and ensure that the required beam is obtained. Without

them would not be possible to have the machine working and the beam with the desired parameters.

1.2 Ion Machines

In this section we will describe in a very generic way the machines in which we are going to focus this dissertation: the ion machines. Under that definition we include the machines that accelerate ions, both positive and negative, regardless of its stability (like radioactive beams) and its charge state. Attending to previous classification, ion machines are found in different flavours. DC its almost used for low energy machines like tandems and ion implanters. The machines that use RF can be further classified in three big categories according to the trayectory of the beam: LINACs are linear machines in which the presence of bending elements (dipole magnets) it is very limited, cyclotrons use one big magnet (or several that simulate a big one) and the particle trajectory is an spiral from the center of the machine, in synchrotrons the trajectory is a circunference of fixed radius and the magnetic field of the bending magnets is increased as the same time the particle energy is increased. More exotic machines that share characteristics from different categories also exist, such as FFAGs, cyclinacs... A review of the accelerator types along with their theory of operation and more advanced topics can be found in [14].

Almost all the ion machines (save the few big colliders) use the accelerated particles to bombard a target. The motives are very different and the energy and the particle are very dependant on the final use. Generally speaking ion accelerators are used when nuclear reactions are needed and when precise energy deposition is required. For example in the medical field we find two different uses: 1) the production of radioisotopes for medical diagnostics require protons with medium energies (tenths of MeV) and not very high currents, and 2) proton/hadrontherapy, which requires higher energy of protons or carbon ions (hundreds of MeV), low current and small and very controlled beam size to damage only the tumor. Ion implanters are extensively used in the semiconductor industry, they use low energy and low current beams of dopant ions. Accelerators for nuclear and high energy physics experiments need higher currents and energies than previous examples, and also more flexibility with the beam parameters for the different experiments of the users. An example of the use of ion beams is as sources of other particles for experiments, in this example for a given

energy (which fixes the cross section of the process), we are interested in having high currents so the secondary particle production is as high as possible.

Compared with electron machines, ion machines have to deal with problems associated with low velocity beams, like higher space charge and longer travel time through cavities. The energy deposition due to beam loses is significantly higher than in electron machines, leading to undesired effects like thermal heating and increase the activation of the machine due to nuclear processes.

1.3   Accelerators for Fusion Energy Research

As the energy demand of the population increases, the need for clean sources of energy to avoid global warming is critical, a goal not possible with our current power generation scheme, which is still heavily based on combustible fuels although the renewable ones are slowly growing, as seen in Fig. 1.1 [16].
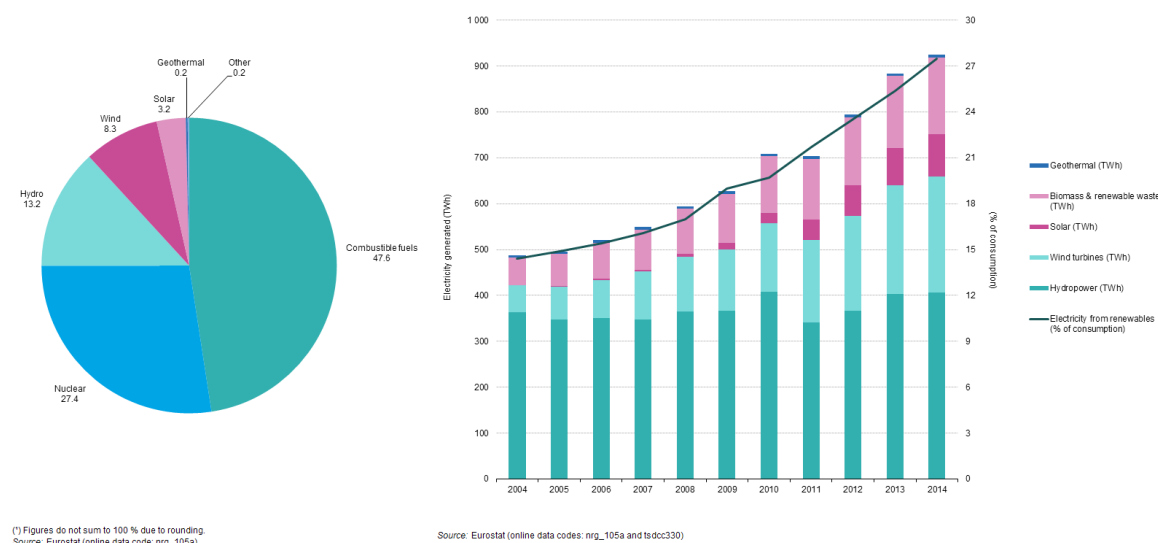
Figure 1.1: EU electricity generation origin (left) and renewable source composition (right) in 2014.

Complementary to existing renewable energies, which are now available and their use is becoming widespread, fusion energy can be a great addition to the energy mix in the future as we seek to eliminate carbon and fuel-based electricity production

and avoid the long term hazards of fission waste from nuclear power plants. Based on light element fusion reactions (Tab. 1.3), the energy production is very high and the primary energy source is easily found in water. The only downside is the activation induced on the reactor wall materials by the neutrons produced in the reaction and material damage. However, there is still a very long path until a fusion reactor will be producing electrical power reliably, and in this long path a particle accelerator is needed in order to produce a high flux of fast neutrons to characterize the materials to be used in the reactor. The actual plan for fusion energy is pictured in 1.2

Reaction	Q released (MeV)
$D + D \rightarrow T + p$	4.04
$D + D \rightarrow 3He + n$	3.27
$D + T \rightarrow \alpha + n$	17.59
$D + 3He \rightarrow \alpha + p$	18.35
$T + T \rightarrow \alpha + 2n$	11.33

Table 1.1: Main fusion reactions for light elements.

The International Fusion Material Irradiation Facility (IFMIF) [17] is a project to build a neutron source for material irradiation and validation for its future use in DEMO, where the materials facing the reactor wall will suffer a huge amount of damage from neutrons ($\sim$30 dpa/year). It is well known that the radiation affects the mechanical and physical properties of the materials via transmutation of its atoms and the creation of point defects. However, the kind of damage is very dependent on the kind of particle and its energy. For fusion reactors the main source of damage are neutrons with a very particular energy spectrum [18], which can be seen on Fig. 1.3 along with other irradiation sources. Furthermore, in fusion applications it has been found that the creation of He bubbles in the material, characterized by the He/dpa ratio, has a huge impact on the grain boundary embrittlement at high temperature in FCC alloys and enhance fracture thoughness at low temperature in BCC alloys. In order to meet the requirements of the DEMO reactor four requirements should be satisfied by the neutron source:

- Intensity large enough to allow fast damage.

- Total damage level above the expected operational time of the component.
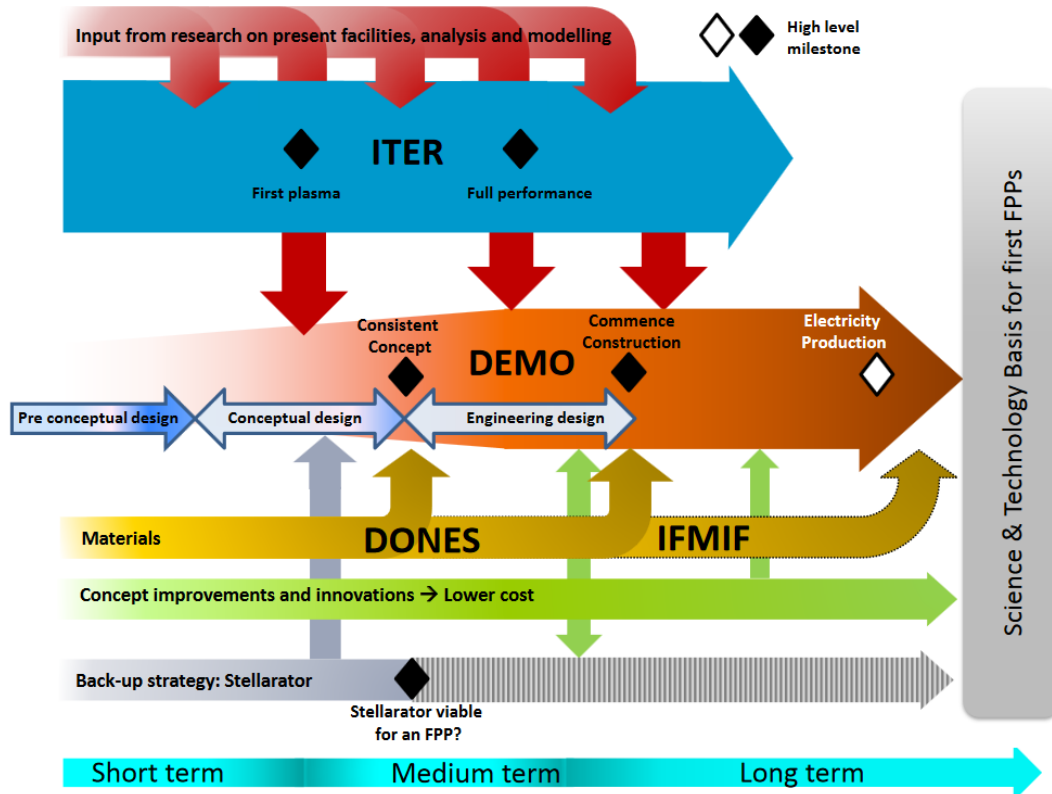
Figure 1.2: Roadmap for fusion energy power plants [1]

- Irradiation volume large enough to characterize macroscopic properties.

- Damage type similar to what it is expected in fusion reactors.

Neutron sources based on Li(d,xn) reactions have been found to be the ones which fulfill the four requirements. In the case of IFMIF, a dual particle accelerator, whose characteristics are resumed in Tab. 1.3, has been proposed, although the facility involves not only the accelerator, but also the liquid lithium loop (the target), the test system and the post irradiation facilities. A plant scheme of IFMIF is shown in Fig. 1.4 Due to budget constraints, a reduced version of IFMIF, named DONES [19], has been proposed as a first step towards the full realization of IFMIF, where the irradiation of the samples will start with only one accelerator.
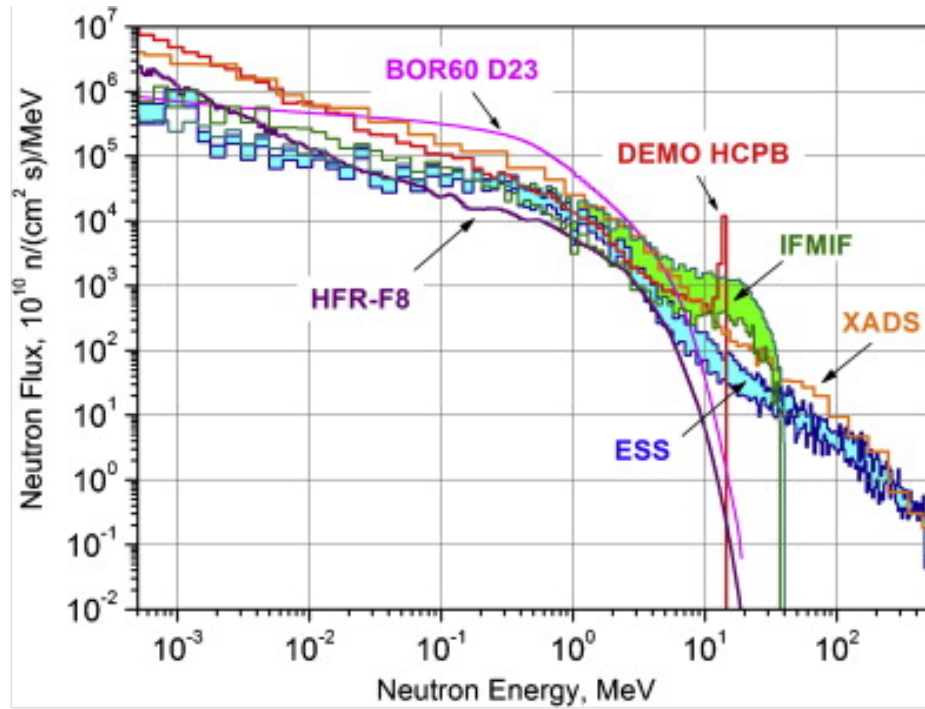
Figure 1.3: Neutron energy spectrum of different sources. Source: ifmif.org.

Particle	D+
Energy (MeV)	40
Average Beam Current (mA)	2 x 125
Average Beam Power (MW)	2 x 5
Reactions	Li(d,xn)
Neutron damage required	>20 dpa/year

Table 1.2: IFMIF accelerator required specifications.

1.3.1 LIPAc

Due to the technical difficulties of a high current and low energy accelerator, it was proposed the construction of a prototype of IFMIF in the frame of EVEDA. LIPAc [20] is the front-end of one of the IFMIF accelerators: injector, RFQ, MEBT but only one of the five cryomodules and a shorter transport line up to a beam dump. It is currently under commissioning in Rokkasho, Japan. The construction of LIPAc is a joint effort between Europe and Japan within the BA signed by both parties.
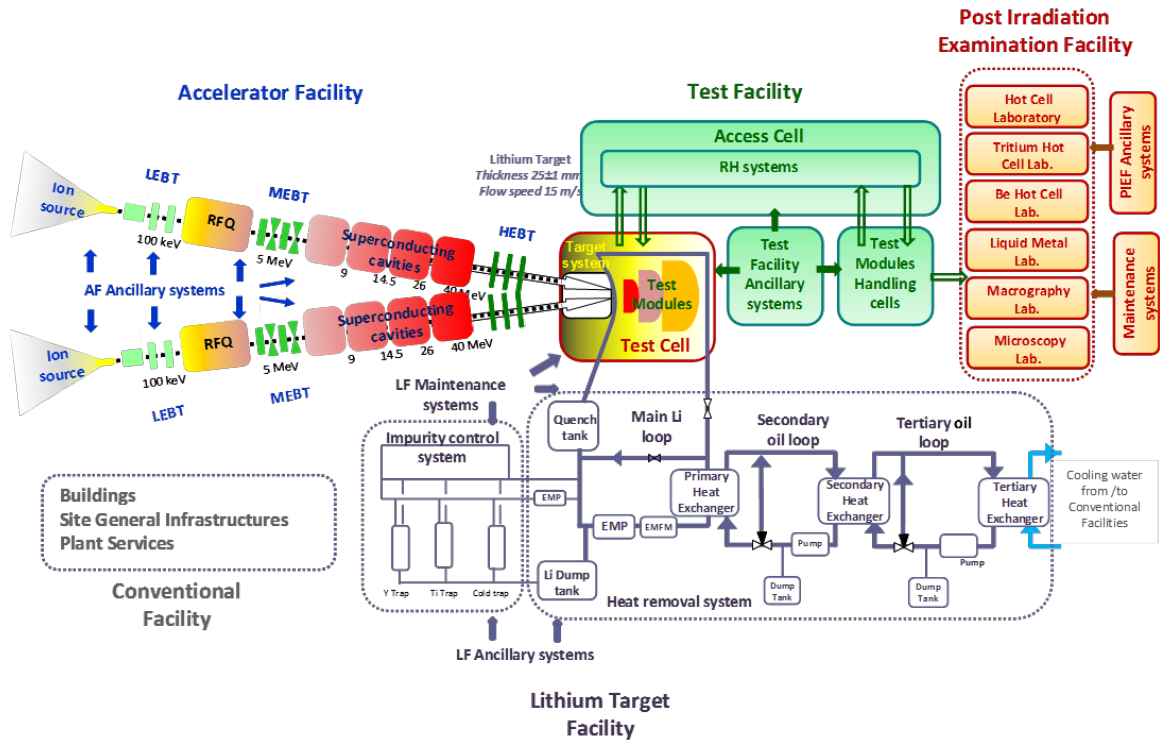
Figure 1.4: IFMIF plant scheme.

The technological difficulties of the IFMIF accelerator are mainly due to the combination of the high beam current and low energy, which produces a very high space charge field. This leads to beam defocussing effects that need to be taken care with the optics, emittance growth and halo formation that yields higher beam losses. Another problem to face from the point of beam diagnostics, low energy leads to debunching effects and low signal intensity for the Beam Position Monitor, or high beam power easily melts the interceptive devices in CW. However, the high beam current offers some opportunities to use of no-interceptive diagnostics based on the interaction with the residual gas, in particular regarding the ones based on light detection, which also have the benefit of not being perturbed by space charge effects. This topic is further disscused in the following chapters.

The LIPAc accelerator follows a scheme typical from high power LINACs. The accelerator starting point is the ion source, in this case an ECR proton/deuteron SILHI source built by CEA Saclay [21]. This kind of source uses multipolar magnets to confine the plasma heated by an RF magnetron. The extraction system is composed of five electrodes installed in the accelerator column that accelerate and focus the

beam at low energy. A LEBT with two normal conducting solenoids matches and transports the beam down to the next section. In order to achieve short beam pulses used for comissioning and tuning of the machine a fast chopper is also installed in the beam line along with some diagnostics.

The next part of the accelerator is a RFQ (currently the longest of the world) made by INFN Legnaro [22]. This 10m long 4-vane RF cavity focuses and bunches the beam during the acceleration. The RF power system is supplied by CIEMAT and delivers a total of 8x200 kW and 8x100 kW of RF power using tethrodes to the RFQ and the SRF LINAC respectively, and another 2 chains of 16 kW each using SSPA supplying the RF power to the rebuncher cavities in the MEBT.

The next section after the RFQ is the MEBT. In only two meters the MEBT [23] (done by CIEMAT) matches the beam parameters to the SRF LINAC parameters. It accomplishes its task in the transverse plane phase space using a quadrupole triplet and doublet combined with correctors with two scrapers for beam purification, and in the longitudinal phase space using two buncher cavities.

Final acceleration is carried out by the SRF LINAC [24], provided by CEA and CIEMAT. It hosts inside eight superconducting HWR to accelerate the beam, and eight solenoids with correctors to provide the transverse focusing and beam steering, and boosts the energy from 5 up to 9 MeV.

The final part is the HEBT and the Beam Dump. Also designed in CIEMAT, it transports the 1.125 MW deuteron beam to a safe stop. Integrated in the HEBT just after the cryomodule the Diagnostics Plate is found [25]. Apart from the LEBT and the several BPM that are scattered along the beam line, as well as several Beam Loss monitors, the D-Plate hosts most of the diagnostics to characterize the beam parameters: current, energy, transverse profile, bunch shape and emittance.

Chapter 2

Beam Diagnostics Overview

Beam diagnostics are a key part of every accelerator. They are the instruments that are going to inform us about the current state of the beam, as they act as the sensing elements of the machine. They are the only way to control the machine and pave the way for the optimization. Beam diagnostics can be classified in many ways, but the most usual classification is according to the beam parameter that they measure without paying attention to the physical principle. Due to the different beams that the particle accelerators are capable of produce we can find that some of the methods employed are not suitable (or impossible) to use in certain circumstances. An extensive review of beam diagnostics is found in [26] [27].

Diagnostics are used in all of the machines, but we can distinguish three different phases when operating the machine:

- Installation and Commissioning: During the assembly and first run of the accelerator special instruments can be used and one tries to gather as much information as possible about the beam characteristics and optics. It can be the case, in particular in LINACs, that dedicated diagnostic benches are built and are integrated during the accelerator commissioning as shown in Fig. 2.1.

- Machine start up and tuning: During the start of the accelerator after each standby period is common to perform tests and measurements in order to check its correct performance and tune the machine parameters if necessary to achieve optimum conditions. These operations can take a lot of time, and usually special
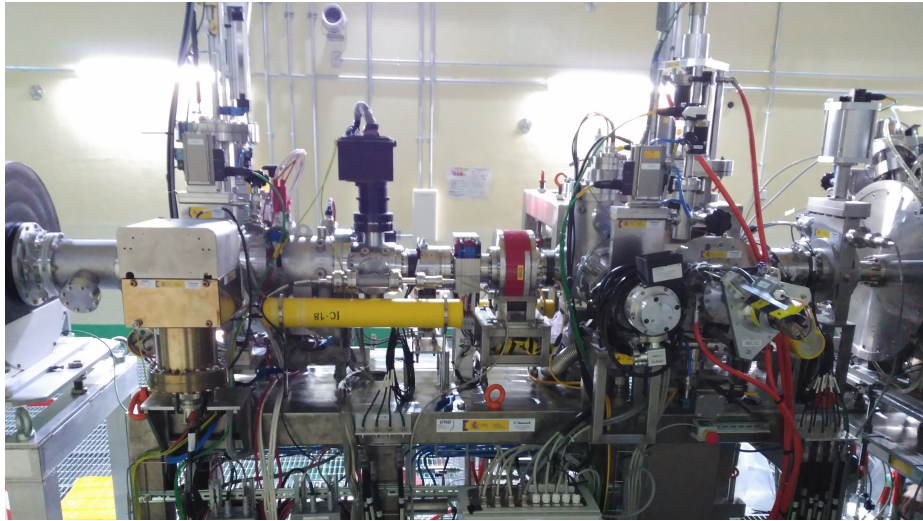
Figure 2.1: Picture of LIPAc Diagnostics Plate.

beam modes are used (smaller duty cycles) which allow to use special techniques (such as quad scans) or diagnostics that destroy the beam (Faraday cups, ...)

- Normal operation: In this category we include the measurements that do not affect the beam parameters (at least not much) and that are needed to ensure the beam delivery with the correct parameters with minimum disturbances. Usually non interceptive diagnostics are employed.

As mentioned earlier, the central role of diagnostics is to provide information about the beam. To do so they need to interact with the charged particles of the beam. Although it can be done in many ways, in the end the information is converted into electric signals that are sent to the data acquisition boards, usually located away from the accelerator for safety reasons. These electronics transform the analog signal into digital ones so they can be sent over ethernet to the control room where the operators and scientists can visualize the information. A general scheme of the diagnostics signal path (of the LIPAc Accelerator) can be seen in Fig. 2.2.

2.1 Beam Current

The beam current is one of the most important parameters of a particle accelerator, since it measures the total number of particles in the beam. Sometimes the beam
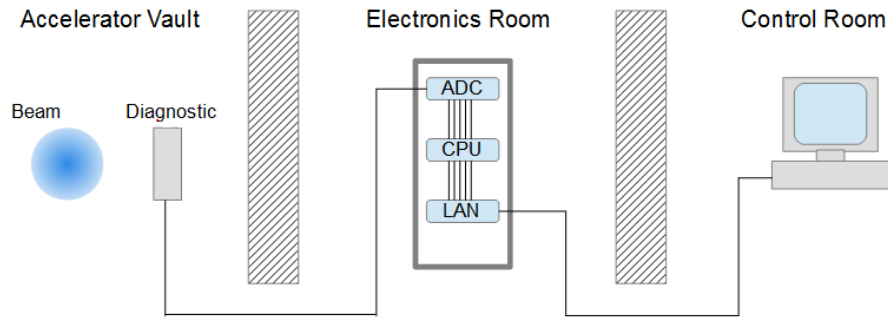
Figure 2.2: Scheme of the signal path in diagnostics.

current can be expressed as the total number of electric particles on the bunch or on the pulse. When speaking in general about the beam current we usually speak about the average current of the beam. It is important to make distinctions between three different currents: 1) the DC current of the beam is the average value of the current over time, 2) the pulse current is the average value of the current in one pulse, only averaging over the pulse duration and, finally, 3) the bunch charge is the electrical charge carried by one bunch. The pulse current and the bunch charge only make sense when the beam is pulsed or bunched respectively. The differences between the three types of current can be seen in Fig. 2.3.
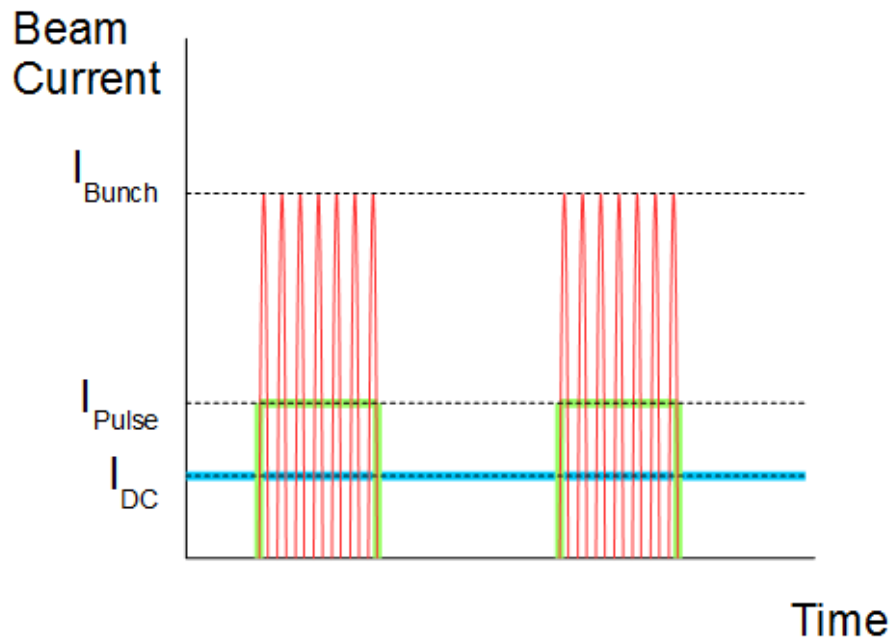
Figure 2.3: DC current (blue), pulse current (green) and bunch charge(red).

2.1.1 Faraday Cups

The Faraday Cup is the simplest method of measuring the beam current. It consists of a piece of metal that stops the beam completely, and then the current is read by means of an ammeter in its return to ground. The Faraday Cup is electrically isolated from the rest of the accelerator, apart from the cable that guides the current to the measuring instrumentation. Although they are generally used for DC or low frequency measurements, they are capable of resolving the bunch time structure if they are carefully designed, as in the case of the Fast/Coaxial Faraday Cups, where the stopping metal part is designed in such a way that forms a coaxial waveguide (50 Ohm generally) with the outer part and it is matched with the outer connector to avoid signal reflections and transmit a faithful time structure replica of the incident bunch.
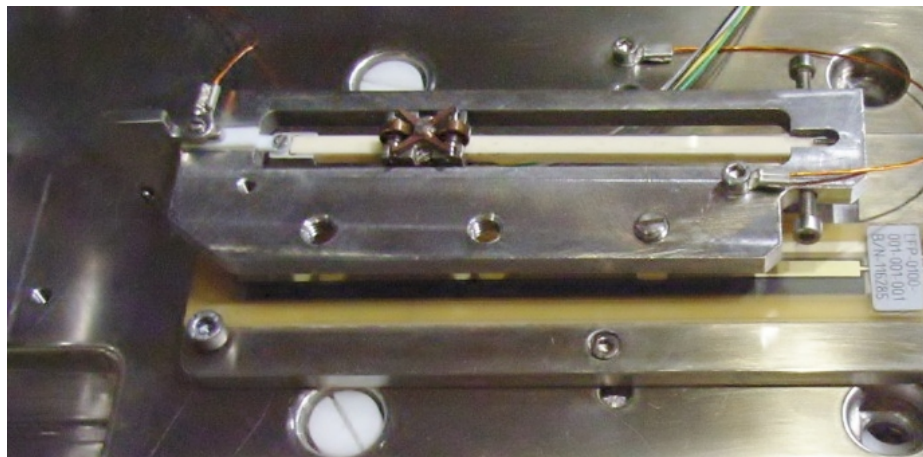
Figure 2.4: AMIT cyclotron Beam Probe. The part that intercepts the beam is the left side small plate.

Faraday Cups have two major problems when it comes to practical design. The first one is the secondary electron emission. As a charged particle moves through a material, it starts to lose energy, and this energy is transferred mainly to the electrons. Some of them gain enough energy to overcome the potential barrier of the surface and escape from the material [28]. The amount of these runaway electrons depends on the energy of the incoming particles and the material properties (mainly the surface). This particle emission essentially can be viewed as an additional current going in the opposite direction superimposed to the beam that is lost to the beam

pipe, and the main problem is that this current also goes through our measuring instrument, thus giving us a wrong lecture of the beam current.

There are several ways to correct this effect. The most immediate of them is just to calculate theoretically the secondary emission yield and do the correction, but this method is not recommended as there can be many factors that make a difference between our case and the simulation/experiment where the tabulated coefficients were obtained. The rest of the methods try to recapture the emitted electrons and therefore the net escaping current is zero. The first one consists of making the Faraday cup very long compared with its transverse size, so after moving almost all of the electrons end up back in the FC. The next one is attaching a repeller electrode on the front of the FC, and polarizing it with enough voltage to turn the electron trajectories back. The required voltage depends on the energy spectrum of the emitted electrons, but in general it is enough with few hundred volts. The last method is the installation of magnets around the FC, usually permanent ones, to avoid the complications of power and cooling of electromagnets. The resultant magnetic field "pin" the electrons trajectories to the field lines that go through the FC metal where the recapture of the electron takes place. Inside a cyclotron the strong magnetic field is already given by the machine, so the moveable Faraday Cup can have a very simple design such as the one in Fig. 2.4.

The second problem of FC is related to the range and energy deposition of charged particles in matter [29]. Here we have to make two disctintions between light particles (electrons) and heavy particles (ions). In the case of electrons at high energy their energy deposition does not have great variations along its trajectory, and it is limited in transverse size, but their range can be very long at moderate to high energies and there is a great emission of secondary particles and bremsstrahlung radiation, hence the need for big FC made of low Z elements. With ions the main problem is the high energy deposition at the end of the ion path, also known as the Bragg peak. Albeit the Bragg peak is of great utility in some cases like ion implantation and protontherapy, in this particular case its existence result in a very high local energy deposition that can lead to very fast local meltdowns. For this reasons the FC used for high power beams usually tend to have liquid cooling and offer oblique surfaces to decrease the surface power densities, as well as using high melting point materials attached to a high heat conductivity one where the heat is removed.

2.1.2 Current transformers

One of the most widespread, reliable and non-invasive methods to measure the beam current is the use of a current transformer. It is based in the detection of the transverse magnetic field generated by the beam. The most basic implementation of this device is a circular ferrite core installed around the beam pipe with a cable wrapped around its circumference. The time varying components of the magnetic field induce a voltage in the wrapped cable, which is read elsewhere. In this basic setup the beam acts as the primary winding of a transformer and the cable as the secondary, with the ferrite ring as the magnetic core. For further refinement of the basic electrical model of our transformer we must include the resistance of the windings, the parasitic capacitance of two sucesive windings and the load effect. A detailed treatment is out of the scope of this work, but detailed information is found in [26]. The final result is that the current transformer will act as a bandpass for the signal generated by the beam, whose central frequency, bandwidth and impedance can be tuned to our needs by playing with the different parameters of the CT: number of windings, material of the core...

As can be noted, the bandpass effect of the current transformer described before has one major drawback: the impossibility of measuring the DC current of the beam. To be able to measure this important beam parameter we have to make a twist to the original transformer design to arrive at the DCCT [30]. In its most basic form it consists in a pair of ferrite cores around the beam with a first winding which injects an AC current that drives the cores into saturation, installed in opposite directions in each core (in one the current goes clockwise and in the other counterclockwise). A second winding which acts as a transformer for the first winding but in the same direction in both of the cores, and a third cable which carries a current in the opposite direction of the beam current which goes through the cores. The working principle is quite tricky but very clever: with no beam the cores are driven symmetrically into saturation by the windings 1 and detected in the windings 2, but with the beam on one of the sides will get before into saturation due to the magnetically polarizing effect of the beam magnetic field. This difference is sensed by the windings number 2 and then it injects in the third cable a current to compensate the effect of the beam. When the signals return to the symmetric state the current on the third cable is equal to the beam DC current, which now can be read from this third cable. An example of an in-flange DCCT is shown in Fig. 2.5.
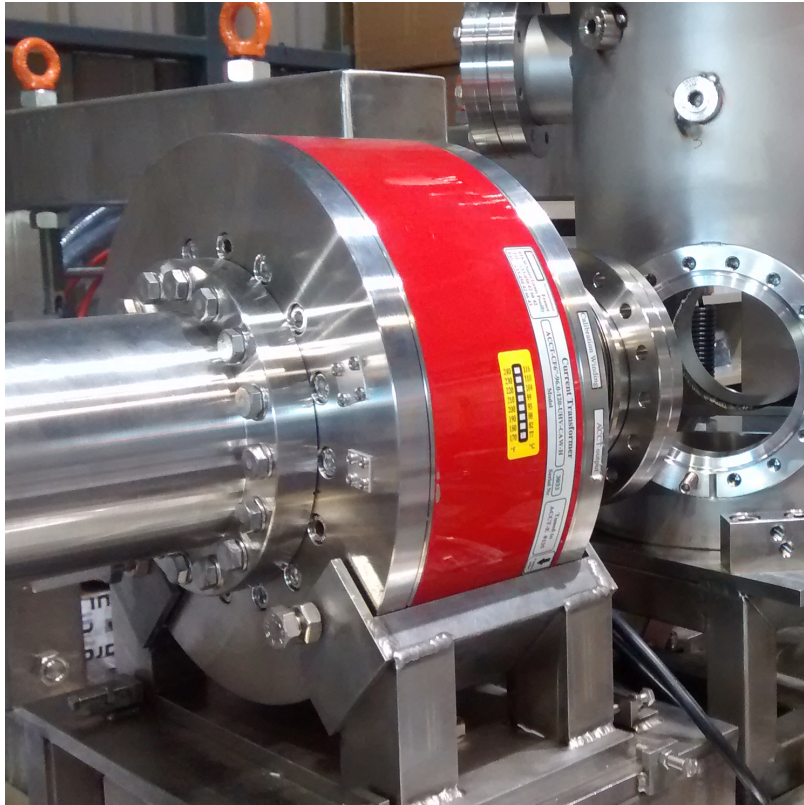
Figure 2.5: Picture of LIPAc DCCT.

2.2 Beam Position

When a beam travels along the beam pipe its transverse position with respect to the geometrical center of the beam pipe is one of the most important parameters to deliver the beam correctly to the target and avoid any collision with the pipe that can lead to beam losses and damage. BPM are one of the most (if not the most) used diagnostics and a big proportion of the total diagnostics of the accelerator. BPM can have several implementations depending on the physical principle that we want to use. In this section we will start with the wire based ones, followed by the residual gas interaction ones and finishing with the most typical: the RF BPM.

The first BPM that we are going to describe are the ones based in the interaction on the beam with wires, typically via secondary electron emission, although more exotic types like photodetachment or compton scattering with laserwires also exist. Those detectors have a secondary role in determine the beam position monitors, as they are mainly used as profile monitors. In this category we can distinguish be-

Figure 2.6: Picture of a wire based Beam Position Monitor.

tween two families: the wire grid and the single wire. In the first family we intercept the beam with several wires in the horizontal and/or vertical direction at the same time and we measure the current in each one of them, either in parallel or sequentially, whilst with the single we move it across the beam and read the data continuously (Fig. 2.6). After the data acquisition we perform some statistical analysis to find the center of the measured distribution and compare it with the calibration data obtained previously, finding the difference in position with respect to the geometrical center of the pipe. It can also happen that instead of the wires a grided scintillating screen is placed, and in this case we compare the distribution recorded in the image with the calibrated data.

The methods based in the interaction of the beam with the residual gas are mainly used (as the methods previously described) mainly in the transverse profile measurement, but also can give a good estimation of the beam position. Here we rely on the electrons/ions generated by the beam in the residual gas, separated by and electrical and/or magnetic field and collected to obtain a distribution, or in the emitted light of the beam. After the data collection one has to do the comparison against the calibration data to obtain the beam position.

Finally, we have the RF pickup based BPM [31], depicted in Fig. 2.7. In this case we use the electromagnetical fields generated by the beam to obtain a measure of the position of the beam. The usual BPM consists of four electrodes placed symmetrically distributed around the longitudinal axis of the beam pipe, each one isolated and with a feedthrough connection to the outer side. Its shape depends on the kind of response that we want to have, and we can find small circular buttons adapted to the pipe contour, striplines and even more complicated geometries like the shoebox. The basic principle of this kind of BPM is to obtain a normalized differential signal between each pair of opposite electrodes, which is a function of the beam distance to the center (linear if that distance is small). The response of the electrodes with respect to a line-like excitation (typically a wire is used) is measured in the laboratory to have calibration data and characterize the deviations with respect to the linear behaviour due to the geometry. This system is the fastest in measuring the beam position and sometimes is used as a ⌐as⌐ feedfordward to other beam correction systems.
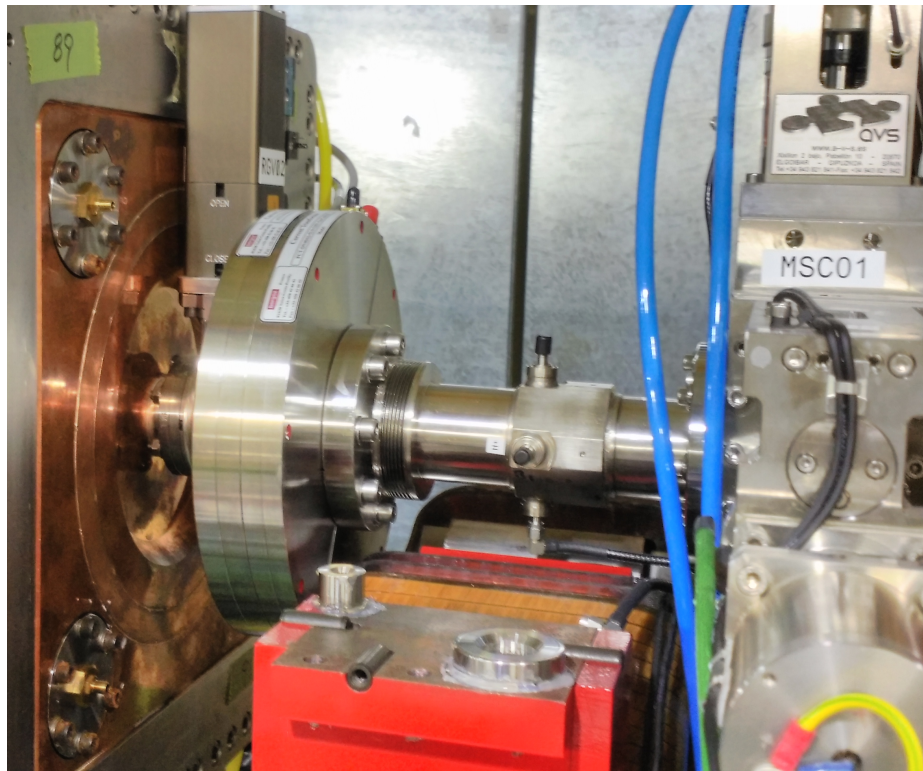
Figure 2.7: Beam Position Monitor assembly in the middle of the first quadrupole magnet of LIPAc Medium Energy Beam Transport Line.

2.3   Beam Transverse Profile Measurement

Another parameter that is important in the characterization of the beam is the transverse profile, which coupled to the beam divergence allows us to determine the beam distribution in the transverse phase space and its emittance. In the previous section we have seen some methods to measure the beam position that are mainly used in the measurement of the transverse profile.

2.3.1   Scintillating screens

The first method is the scintillation screen [32], consisting of a piece of scintillating material that is placed in the path of the beam, and when the charged particles hit the beam the screen emits light. To help in the calibration the screen can be etched with a grid pattern of predefined dimensions. This method completely destroys the beam at low energy, but at high energy with thin screens it can be considered almost non interceptive. The advantage of this method is that it can give us a direct image of the transverse profile of the beam instead of the projected vertical and horizontal profiles.

To be suitable for this application the material needs to have a good scintillating yield in order to give a good image. It also needs to be stable under irradiation for extended periods of time and to temperature changes, as the energy deposition (specially from low energy ions) can be quite high. Linearity with respect to the beam current and high dynamic range are also desired features in order to have a faithful reproduction of the profile [33]. In Fig. 2.8 is shown the scintillator of the AMIT's cyclotron transverse profile monitor designed during this dissertation.

2.3.2   Wire based methods

An alternative to scintillation screens are interceptive wires. Their working principles are quite simple: a moving wire or a grid of them intercepts the beam and the interaction is measured, like the one shown in Fig. 2.9. This kind of interaction is usually the electron emission from the wire from the direct current energy deposition,
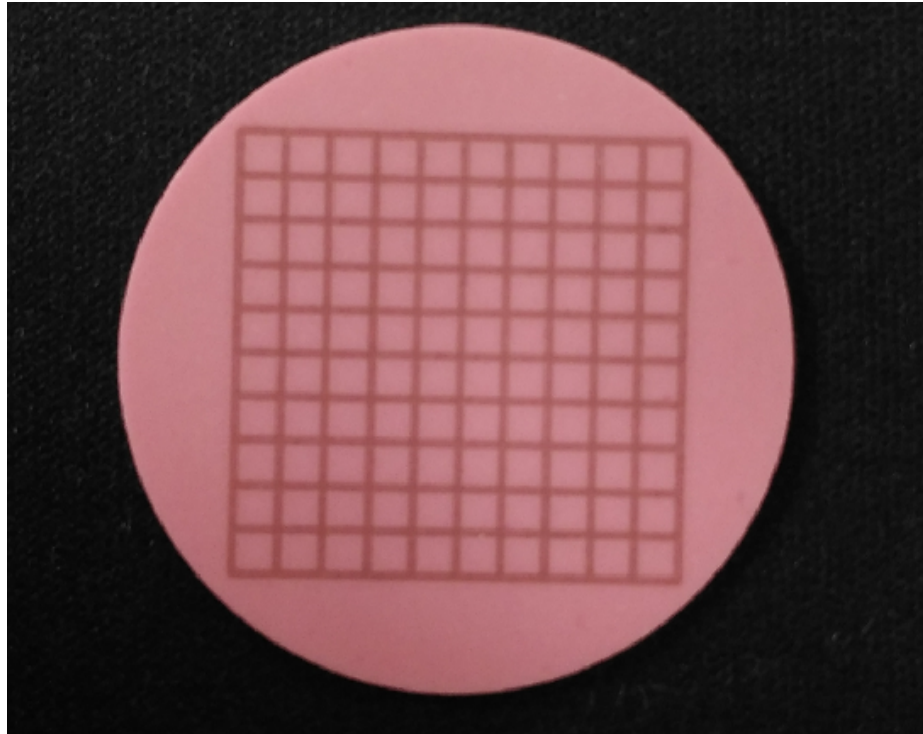
Figure 2.8: Picture of the AMIT cyclotron Cr:Al$_2$O$_3$ screen.

but it can be secondary particle production (in high energy beams) or even Compton scattering or photoneutralized atoms in the case of laser wires.

The main drawback of this method is that only gives us the projection of the beam profile on the scanned axis, so usually a pair of grids or moving wires are employed to obtain the vertical and horizontal projections if it is not possible to use the same wire with two different directions, as in the wire scanner that enters at a 45° angle and first measures one projection and then the other.

2.3.3 Residual gas interaction methods

One important characteristic of the scintillating screen and the wire based transverse profilers is that they need to interact with the beam, leading in some cases to energy losses and emittance increase. There are even some circusmtances, for example in high power, low energy LINACs, where there is no material capable of withstanding the thermal load of the beam without melting. In these cases we can use the interaction of the beam with the residual gas of the beam pipe.

20
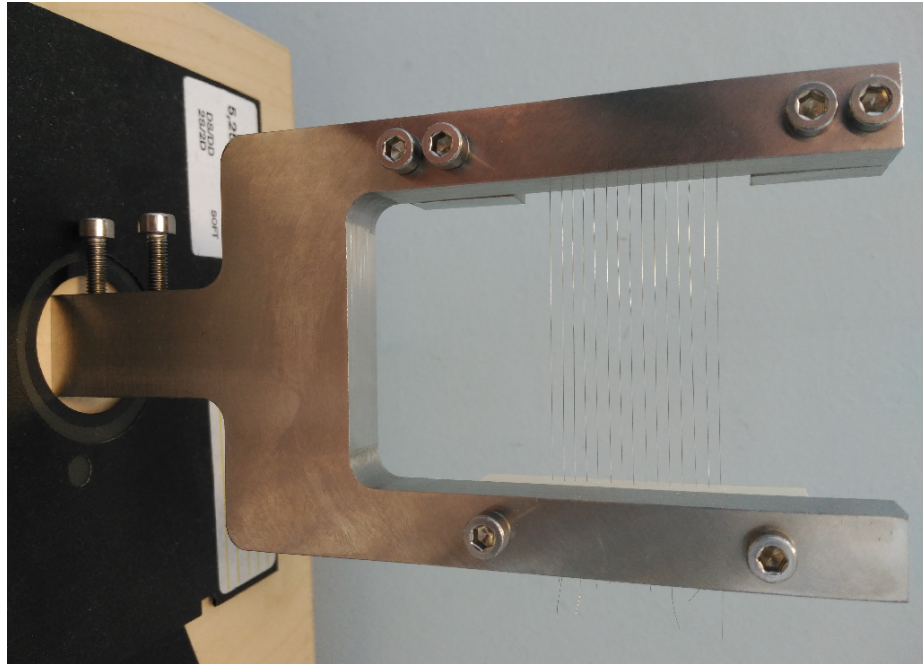
Figure 2.9: Picture of a wire grid transverse profiler.

The interaction of the beam with the atoms/molecules can be used in two ways: with the electron/ion pairs created by ionization and with the light emitted from the excited particles. One inconvenient of these methods is the low cross section associated with the processes, thus high currents, long integration times and/or external pressure bumps are needed for obtaining a useful signal.

The Ionization Profile Monitors [34] collect the positive or negative charges generated by the beam by means of an external electrical field, and sometimes also with a magnetic field. Once the charges have been generated they drift along the field lines and are collected either in conductive strips or in a MCP. After the charge collection (and amplification if MCP are used) the signal is read on dedicated electronics and the projection of the transverse profile.

In the case of FPMs [34] the photons emitted in the decay of excited states form the image of the beam's profile in a high sensitive detector using a lens without the need of external electromagnetic fields. In this case more information can be obtained if we can separate the different wavelengths. Regarding the detector, at higher energies the cross sections drop significantly and camera sensors are not able to read anything but noise, therefore intensified cameras (Fig. 2.10) or even PMT arrays are used.
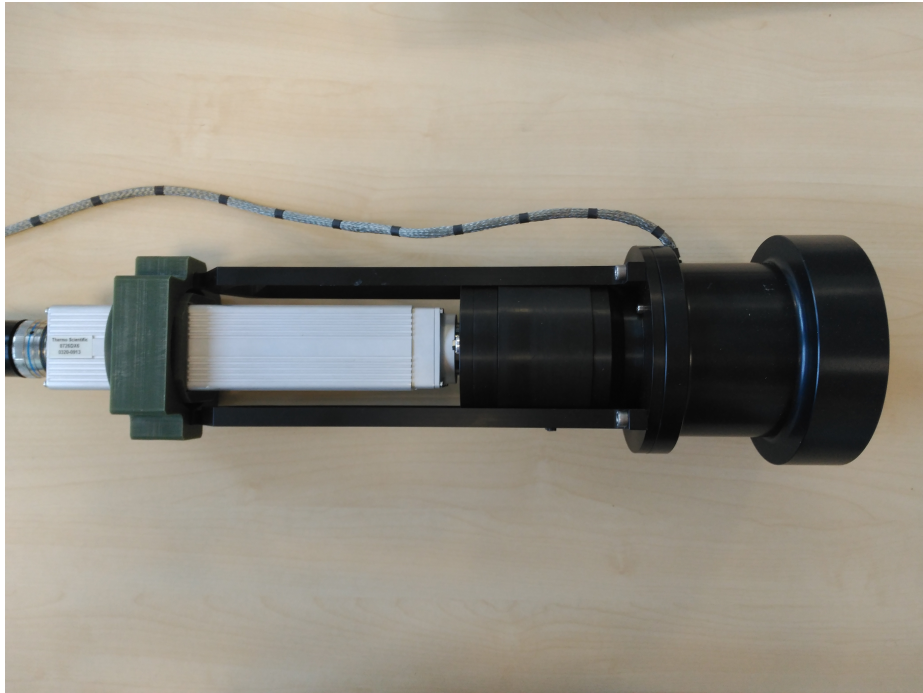
Figure 2.10: Picture of Fluorescence Profile Monitor based on Intensified CID camera.

2.3.4 Synchrotron Radiation Monitors and Optical Transition Radiation

At high energies when the particles are very relativistic new physical effects come into play and we can make good use of them. Due to the low mass of the electrons these methods are mainly used in electron machines. However the same effects also appear with protons at TeV energies.

Synchrotron radiation monitors [35] are located in the bending magnets of the electron accelerators, where synchrotron light is emitted with a spatial structure equal to the beam's transverse profile. In the cases where the beam is so small that the diffraction limit is reached we have to rely on double slit interferometers to get information from the synchrotron light.

Optical Transition Radiation [36] is produced when the relativistic beam approaches to a thin metallic screen and goes through it. The method can be considered non interceptive at very high energies and thin foils. The light is emitted with an angular distribution related to the transverse beam profile, then the image of the radiation pattern is formed in a sensor and the corresponding fit to the image

is performed to obtain the beam size.

2.4   Beam Transverse Emittance

Apart from the beam profile, the other parameter needed to determine the transverse phase space of the beam is the beam divergence. The techniques used in the measure of the emittance determine both the beam profile and the beam divergence. We can distinguish three different methods:

- Slit and Grid: This method is essentially reconstruction of the phase space by taking in each step measurements of different positions. For the Slit and Grid method [37] one focuses on one plane (vertical or horizontal) at a time, and by means of a moveable slit a position scanning in the phase space is done. After the slit the particles travel a distance in the free space and the profile of the passing beam is measured because it is correlated with the momentum distribution in the phase space in the slit position. The process is repeated for both planes with different positions of the slit in order to map completely the beam phase space.

- Pepperpot: The pepperpot principle [37] is based on the same principles as the Slit and Grid, but in this case small holes are drilled in a planar plate to map the vertical and horizontal positions at the same time. After passing through the holes the particles diverge according to their transverse momentum and after some distance they impact on a scintillating screen. The recorded image of the screen shows the distribution of the momentums in the transverse phase space for every position where the holes are placed.

- Quadrupole Scan: The quadrupole scan [26] calculates the beam emittance by varying the focusing strength of a quadrupole magnet, which in turn produces a change in the profile that is measured some distance away from the quadrupole by a transverse profiler. After several measurements the data of the profile is fitted to a curve and the Twiss parameters are obtained, making the calculation of the emittance straightforward. Another variation of this method uses a quadrupole with a fixed strength and then several measures of the profile are taken at different positions.

2.5   Beam Longitudinal Emittance

The last parameter of special importance for every accelerator is the energy of the beam, which determines the velocity of the charged particles and is crucial for the experiments that require the beam. In the case of RF accelerators not only the energy is needed, but also the bunch structure and the energy dispersion.

The most used method for the measurement of the energy relies on TOF measurements between different points of the accelerator placed at a known distance, like the ones shown in Fig. 2.11, either performed with several RF pickups or electron detectors coming from the residual gas ionization, but can only be used in the non relativistic regime. It is possible to measure the energy of the beam also in an indirect way by measuring the amount of energy deposited in materials and use the Bethe-Block formula to relate it to the beam energy.
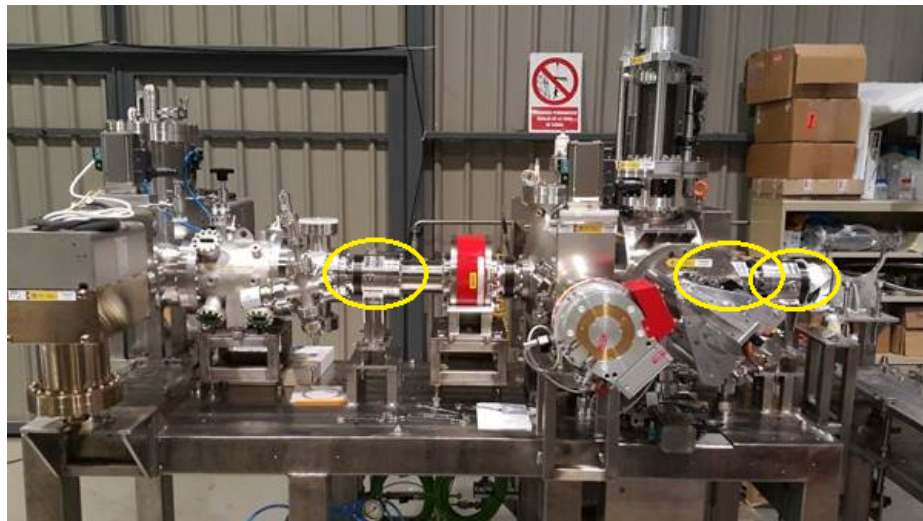
Figure 2.11: Trio of BPMs used for energy measurements in LIPAc D-Plate (inside yellow circles).

In the case of the bunch structure several methods also exist. The Wall Current Monitor [38], RF pickups and the coaxial Faraday Cup can provide a direct measure of the bunch shape if they are designed in a proper way. When these methods are not available due to high power beams or not enough signal the electrons from ionization can also be used as in the determination of the energy, but in this case is necesary to include a RF deflection system to resolve the time structure of this electrons [39]. Finally a method similar to the quadrupole quad scan can be performed

in order to measure the longitudinal emittance, but in this case a buncher with variable voltage takes the role of the quadrupole and a WCM/RF pickup/Coaxial FC measures the time structure of the manipulated bunch [26].

Chapter 3

Fluorescence Profile Monitors

In the previous chapter we have presented a glimpse of the Fluorescence Profile Monitors for transverse beam profile measurements. In order to have a complete picture of the subject we have to pay attention to both practical and theoretical aspects, mainly on how light is produced, the detection and light guiding systems, the uses of the beam induced fluorescence in the field of particle accelerator diagnostics and the errors in the measurements introduced in the process and how to correct them. In this chapter we will deal with the practical aspects of the FPM, paying attention to the detectors and the ways to use the beam fluorescence in our advantage to get information of the beam.

The key part of Fluorescence Profile Monitors is the light detector. It will determine the different parameters of the system, like the precision, accuracy, integration time, spectral response... In general emitted photon flux is orders of magnitude lower than common light sources, like a LED, and usually the individuals photons are detected and used to reconstruct the profile. Hence high integration times and light/signal amplification mechanisms are mandatory. In FPM the light detected typically has wavelengths between 370 nm and 750 nm, which includes all the visible spectrum and small zones of the ultraviolet and infrared. Traditionally the most used system for imaging has been the intensified cameras taking pictures of the horizontal or vertical projected profile, but since the width change of the beam is usually small in the field of view, integration along the beam axis is possible and allows the use of a 1-dimensional scan or array of individual detectors.

Paired to the detector, a image forming element is needed. As the light is emitted isotropically, at least one optical element is needed to form the beam image in the sensor. Depending on the operation conditions, specially in high radiation enviroments like [7], it is not possible to install the detector in the beam pipe, thus the use of optical lines or image fibers is needed. An optical line is a combination of lenses and mirrors that transports the image of the beam from the beam pipe to some other location where the readout electronics are safe with respect to the enviroment. Image fibers are a special kind of optical fibers composed of multitude of small filaments that transport the image projected on one end to the other. Each system has its advantages and drawbacks, on one hand image fibers are easily installed as they are flexible and small, but have higher losses, limited spatial resolution and scintillate and degrade in the presence of radiation. On the other hand optical lines require more careful installation planing and they are quite cumbersome to align correctly, but are most robust against radiation and do not suffer from limited resolution like the image fibers.

The image forming elements are commercially available lenses, which in some cases, like the widespread borosilicates , use materials that are not prepared to withstand radiation damage, leading to shorter lifetimes which force frequent maintenance periods. A good overview with useful links and references can be found in [40]. Due to the low photon count optical systems with as few elements as possible are preferred to minimize insertion losses. However, in the case of the use of image fibers and optical lines the need for relay lenses and several mirrors cannot be avoided.

3.1 State of the art

The process of fluorescence light emission has been a long known process in the field accelerators [41], although its practical use started to receive more attention with the development of high current ion accelerators [42] [43]. Although most of the has been focused on using gases, either residual or injected via valves or jets, developments on metal vapors have also been done [44]. The most recent overview of the field focused on ion machines was done by [45], where the FPMs of different machines were classified.

Each accelerator require tailored diagnostics to operate succesfully. In the case of the FPM of PSI [46] a solution based on a moving PMT was adopted, being its reliability its main strength. In order to increase the number of emitted photons, both LANL [47] and BNL [48] opted for external gas injection, although the former is based on a pulsed valve, whilst the latter employs a gas jet to greatly increase the local pressure at the position of the beam, allowing the use of a plain CCD camera to view a GeV beam. Measurements of fluorescence at even higher energy were done at CERN in the PS and SPS, where valuable information about the cross section of N_2 and Xe was obtained [49] with the use of PMTs, and the characterization of a MCP based detector was done [50]. Extensive work has been done in the UNILAC at GSI [51], where the fluorescence light produced by different gases under the passage of different ions has been extensively studied using a compact spectrometer with an MCP and a CCD camera. A solution based around a PMT array was used in the cyclotron beam line at COSY [52] and CIEMAT [53], allowing parallel acquisition of the beam profile which was not possible with single moving PMTs. In the case of CIEMAT, the design should be able to measure and survive the high radiation enviroment of the LIPAc accelerator. This is also the case of the diagnostics of the SILHI source from CEA [54], where the transverse profile is recorded with cameras and a spectrometer with a cooled CCD camera measures the different beam species using the Doppler shift of the Balmer lines. In that case, the spectrometer is kept away from the radiation using an image fiber. A different approach aimed at obtain the complete transverse profile of the beam in a low energy line was done at IAP [55] using a rotating vacuum chamber and a CCD camera.

Since the publication of [45] research and development on FPM for ion beam has continued. The work done at GSI [51] has confirmed the suitability of fluorescence based transverse profile diagnostics for FAIR [56], and they are still operative in the UNILAC. The developments on Doppler spectroscopy and transverse profile monitors for low energy transport lines have been implemented in the SILHI [57] source, which is the current injector of the IPHI [58] and LIPAc [59] accelerators, and has inspired the design of the ESS injector [60]. Also in the LIPAc the detectors developed at CIEMAT are installed in the high energy sections [25], and are the base design for DONES. New development for the J-Parc high energy accelerator have started in recent years [61], aiming to use optical fibers to overcome the induced attenuation and radioluminescence problems typical of high radiation areas.

However, the most advanced research has been done in the frame of the High Luminosity LHC project [62], where with the combined effort of CERN, GSI and the Cockcroft Institute an FPM for an electron lens [63] is being built. This device uses a gas jet courtain [64] to produce a high amount of photons. After a filtering process spectral lines involving spin flip, only excited by electrons, are selected and its corresponding spatial profile is measured, allowing to separate the contribution of electrons and ions to the luminescence.

3.2   Integrating detectors

In the market it is possible to find many different kinds of image detectors. In the field of particle accelerators only four of them are normally used: Charge Coupled Device, Complementary Metal Oxide Semiconductor, Charge Injection Device and Video Tubes. More information about the different sensors can be found in the following sections an in [65].

3.2.1   Video Camera Tubes

In video tubes, the charge is generated by the photons in a substrate and by means of a scanning electron beam the readout is done. This technology is outdated in performance and are difficult to find outside the nuclear instrumentation world. On the other hand, the radiation resistance of these devices surpasses even the CID sensors.

3.2.2   CCD

CCD sensors [66] have been the workhorse of scientific cameras for several decades. They are based on the trapping of photogenerated electrons in potential wells created by MOS structures, which are shifted sequentially to an analog to digital converter when the amount of generated charge in each pixel is read. The technology has been very refined, but the collect and shift of the charge still remains as an intrisic characteristic.

3.2.3 CID

CID sensors [67] feature single pixel access and they can perform non-destructive readout. Their structure is similar to CCD, but instead of transfering the photo-generated charge they inject it in the substrate. Their most important advantage its inherent radiation resistance, up to several tenths of thousands of Gray in some devices. This comes at expenses of their performance, having slower frame rates and lower pixel density than both CCD and CMOS.

3.2.4 CMOS

CMOS sensors [68] differ from CCD ones in the design of the pixel cell because every cell can be accessed individual.1. In the CMOS case the photogenerated electrons are trapped in a capacitor structure, so the voltage is proportional to the amount of charge stored, and in each read cycle the voltage is read and the capacitor depleted to be ready for the next charge collection cycle. Due to the fabrication techniques the auxiliary electronics needed to perform the voltage readout, select the cells and manage the communications with the external world can be integrated in the same chip.
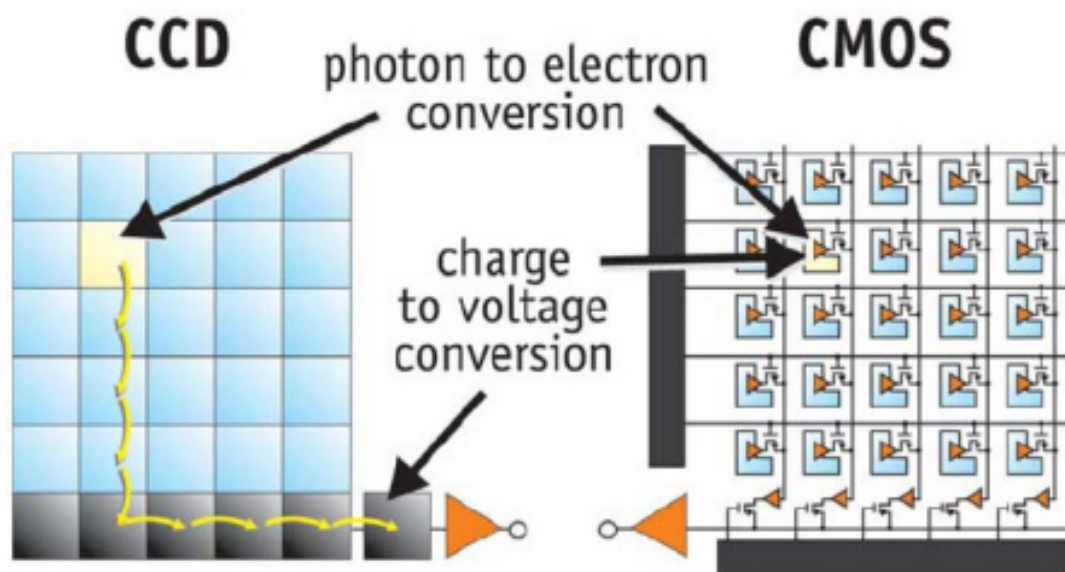
Figure 3.1: CCD vs CMOS sensor operating principle.

3.3 Charge multiplier detectors

At high energies the cross section for fluorescence emission drops significantly according to the Bethe formula, and the light level is so low that even low thermal noise cooled cameras with long integration times are unable to get a good image. In those cases an image intensifier is needed, which can be integrated in the detector if the gain is not extremely high, like Electron Multiplier Charge Coupled Device (EMCCD), or be a separate part, like the Micro Channel Plate. In the case of EMCCD cameras each pixel has associated an electron multiplying device, generally an Avalanche PhotoDiode (APD), which amplifies the signal coming from the photogenerated electrons and holes. The MCP [69], are a bit different, as they consist of a plate with thousands of microperforations packed very close and with a low inclination with respect to the surface.

3.3.1 MCP based image Intensifiers

The working principle of the image intensifier is represented in Fig. 3.2. The photons emitted by the beam hit the surface of the detector, where the photocathode is located, emitting electrons; this photocathode is negatively biased with respect to the perforated plate, so the emitted electrons are accelerated to the surface of the MCP where they enter the microholes. Due to the small angle between the electrons trajectories and the microhole's axis, a collision takes place and more electrons are emitted, which are further accelerated and keep bouncing between the walls, multiplying its number. When they finally leave the MCP they are accelerated towards a phosphor screen, where the same image that was formed in the photocathode appears but its brightness is increased by several orders of magnitude, although a little bit blurred due to the finite size of the holes and the dispersion of the electrons. The phosphor screen image is then recorded with a detector from the types mentioned before. In the image intensifier (Fig. 3.2) there are several parameters to tune: the electron gain changes by varying the voltage across the MCP, synchronization is achieved by pulsing the bias voltage of the photocathode at the same time of the beam arrival. Voltage between the plate and the phosphor screen is usually kept constant.

In the family of photocathodes for the visible range we find three types:

- Bialkali: The most common photocathode. It was originally used for high energy physics, so it is designed for ultraviolet and blue light, with very little quantum efficiency in longer wavelengths. On the other hand it has the least background noise of the three types.

- Multialkali: It is a modification of the bialkali type, increasing background noise at the expense of increasing the quantum efficiency at longer wavelengths.

- GaAs based: The new generation of photocathodes. They are centered in the visible spectrum, with a significant increase in the quantum efficiency. Regarding the noise they improve the values of multialkali, but they are not as good as the bialkali ones.
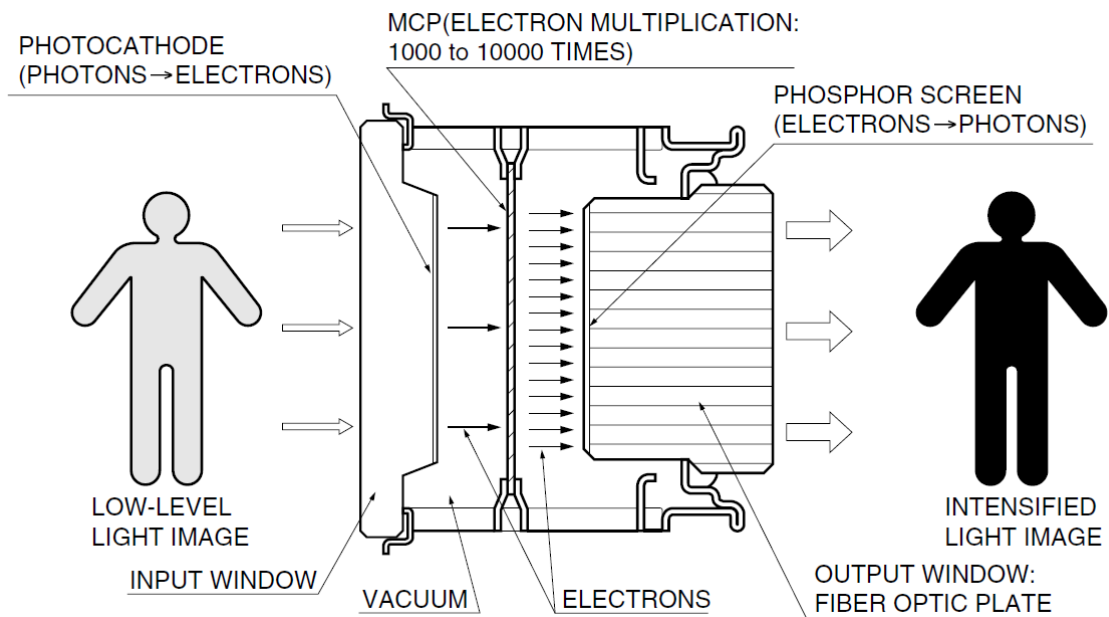
Figure 3.2: Image intensifier working principle [2].

3.3.2 Avalanche detectors

The main feature of image sensors is the fact that we can have additional information apart from the profile. This advantage is particularly useful when there is a variation in the longitudinal axis, such as in the case of a gas jet courtain [64], or when it is necessary to separate the contribution of the different spectral lines to the total

profile [70]. Nevertheless in the majority of the cases it is only required to obtain a projection of the transverse profile. Therefore we can use separate detectors arranged in a linear array to perform a sampling of the beam profile. Depending on the light level we can use different detectors. In the case of high photon flux we can use standard photodiodes [71], and when the light level is not enough we can change to APDs. If APDs are not enough we have to switch to photomultipliers [72]. While photodiodes and APD (normal mode) rely on using longer integration times, PMT and APD in Geiger mode use very high gain to achieve high sensitivity, and are even capable of photon counting. In recent years a lot of effort in the field of detectors for High Energy Physics has been put in the development of silicon photomultipliers [71]. Although having different denominations (SiPM, MPPC, SSPMT,...) the SiPM is basically an array of multiple APD operating in the Geiger mode with integrated quench resistor, where each cell is so small that guarantees very low probability that a photon hits a cell that has been activated before and has not recovered yet from the avalanche and posterior self-quenching.

Figure 3.3: From left to rigth: APD (S5345), PMT (R1450) and SiPM (S13360) [2]

The array detectors share the same optical system for the image forming, where instead of the bidimensional image sensor we put an array of our detectors [53] (or standard optical fibers attached to the detectors [73]) thus the image is sampled at different points.

3.3.3 Spectral measurements

There are also applications of the beam induced fluorescence where only one detector is needed, like the analysis of the different species that come out of an ion source, where

by means of the Doppler shift and their different masses one can distinguish between H^+, H_2^+ and H_3^+ at the exit of an ECR source [74], or determine the proportion of the light coming from recombination of the beam particles with the residual gas by means of charge exchange [54]. In all of these situations the same virtues and defects of the previous detectors are considered, but a spectrometer or some diffractive element should be put between them and the beam to separate the light according to our needs.

3.4   Beam tomography

So far we have only considered the use of fluorescence in the determination of one profile (either vertical or horizontal) of the beam. This is because in its most basic form an FPM is only capable to measure the projection of the total transverse profile in one direction, always under the conditions of small observation angle and field depth enough to cover the whole beam. However it is possible to reconstruct the transverse profile using tomographic techniques based on the Radon transform or sinogram [75]. To obtain a set of images one can place several detectors at different positions in the beam chamber, but this method is costly and the reconstruction from a few directions does not give good results in the case of beam with complex shapes. In that case, a movable detector is preferred. These last techniques have been employed successfully in [76] using a rotating monitor, but they have the inconvenience of requiring a special vacuum chamber to allow the recording of images at different angles.

The issue with the rotating vacuum chamber is partially solved by the use of an optical device called "mirascope" [77] which has the capability of forming the image of the beam outside the vacuum chamber (Fig. 3.4), simplifying greatly the mechanical design of the system. However it has limited range and to have the full information two adjacent mirascopes oriented turned 90 degrees with respect to each other are needed and a correction has to be done to take into account the change in beam shape between the two different positions due to the divergence of the beam.

Another candidate for optical beam tomography, which was studied in the frame of this thesis but was discarded due to the difficult implementation, is a system based on a 4-f lens system (Fig. 3.5) with a movable slit in the intermediate focal plane [78]. By moving the slit we can select the angle of the rays of light and do the
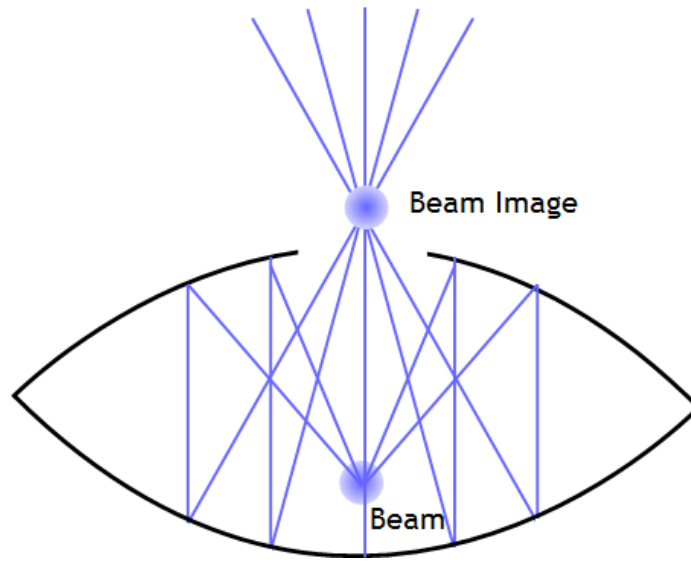
Figure 3.4: Mirascope working principle

different measurements of the profile required for the tomography. This setup has several drawbacks when it comes down to the practical implementation. Due to the slit the light collected is very low and the ratio between the focal length and the lens aperture should be small in order to have a wide angular field (it still need at least another system at 90º), and the beam size should be small with respect to the lens size. For these reasons is very difficult to build a working system based on the 4-f principle, although theoretically the system should be feasible.
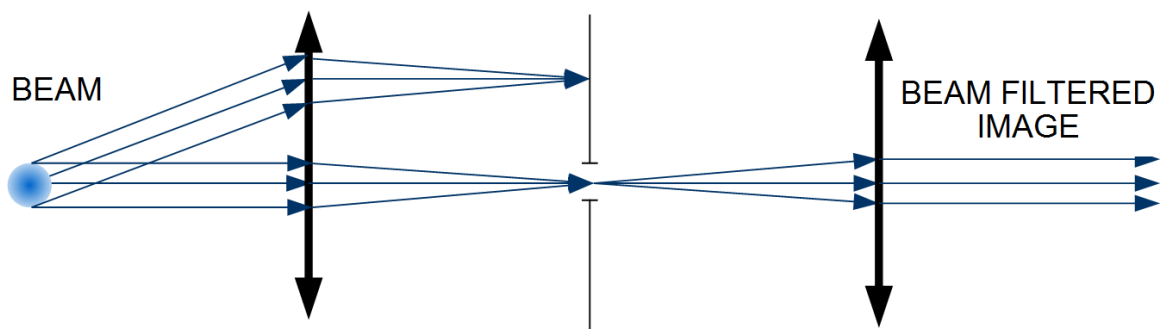
Figure 3.5: 4f system working principle.

Chapter 4

Beam Fluorescence Theory

The main focus of this dissertation are the Fluorescence Profile Monitor. Since they are non-interceptive monitors, they give the possibility to monitor the beam without disturbing it. Additionally, they are less affected by the space charge distortion than IPM and they can be made radiation hard. However, the fluorescence cross section is quite small thus the number of generated photons is very low, making them only suitable for high current beams, such as the IFMIF one (see chapter 7). The working principle of Fluorescence Profile Monitor is the fluorescence radiation emitted by the excited atoms and/or molecules. The spectral characteristics of the emitted light and the yield of the different lines depend mainly on the electronic structure of the target, but the projectile is also important in the characteristics of the emission. Hence the type of the projectile (e.g. electrons, ions,...) should be considered. In this chapter we will make a short review of the theoretical aspects behind the fluorescence profile monitors, starting with the simple quantum mechanical model of the hydrogen atom, following with a brief detour to polyelectronic atoms and molecules. Then, a discussion about the time dependent interactions will follow and we will finish with the interaction between projectile and target.

4.1 Atomic and molecular structure

4.1.1 The Hydrogen atom

The Hydrogen atom, with only one proton and one electron, is the simplest atom we can find in nature. In this particular case we can accurately predict the energy levels of the hydrogen by solving the three dimensional stationary Schrödinger equation without having to rely on approximations and numerical simulations. A complete study of the atomic hydrogen is found in [79]. We will start our short review with the three dimensional Schrödinger equation (Eq. 4.3). After defining the total mass in Eq. 4.1 and reduced mass μ in Eq. 4.2 we can split it (Eq. 4.4) into two different equations, one describing the center of mass of the electron-proton system and one describing the movement of the reduced mass. Due to the difference of mass between the two particles the center of mass almost coincides with the proton position and the reduced mass with the electron "position". The first equation describes the movement of a free particle, which is of little interest for our problem, but the second is what holds all the information, as is written in Eq. 4.4.

$$M = m_1 + m_2 \tag{4.1}$$

$$\mu = \frac{m_1 m_2}{m_1 + m_2} \tag{4.2}$$

$$\left[-\frac{\hbar^2}{2m_1} \nabla_1^2 - \frac{\hbar^2}{2m_2} \nabla_2^2 + V\left(\mathbf{r_1} - \mathbf{r_2}\right) \right] \psi\left(\mathbf{r_1}, \mathbf{r_2}\right) = E\psi\left(\mathbf{r_1}, \mathbf{r_2}\right) \tag{4.3}$$

$$-\frac{\hbar^2}{2\mu} \nabla^2 \psi\left(\mathbf{r}\right) + V\left(\mathbf{r}\right) \psi\left(\mathbf{r}\right) = E\psi\left(\mathbf{r}\right) \tag{4.4}$$

Where $\hbar$ is the reduced Planck constant, μ is the reduced mass, V the potential, E the energy eigenvalues and ψ the wave function. Due to the spherical symmetry of the Coulomb force we can split the wave function (Eq. 4.5) in the radial function (Eq. 4.6) and the angular function, which corresponds to the spherical harmonics. The final solution depends on the quantum numbers n, l and m.

$$\psi_{nlm} = R_{nl}(r) Y_{lm}(\Theta, \phi) \tag{4.5}$$

$$\frac{1}{r^2} \frac{d}{dr} \left(r^2 \frac{dR_{nl}}{dr} \right) + \left[\frac{2\mu}{\hbar^2} \left(E - \frac{Ze^2}{r} \right) - \frac{l(l+1)}{r^2} \right] R_{nl} = 0 \tag{4.6}$$

After solving Eq. (4.6) we obtain the Bohr formula for the energy levels of an atom with a nucleus with charge Z, given by $E_n = -\mu Z^2 e^4 / 2\hbar^2 n^2$. In Fig. 4.1 we can see the distribution of the energy levels of atomic hydrogen. In this simple case the energy is only determined by the principal number n, however, in presence of external fields this degeneracy is broken and the levels are split according to the angular momentum.
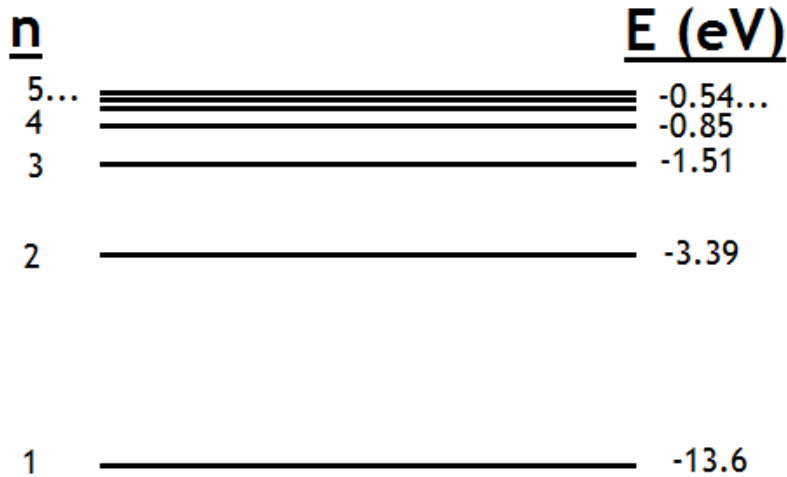
Figure 4.1: Energy levels and principal numbers of atomic hydrogen derived from the Bohr formula.

4.1.2   Polyelectronic Atoms and Molecules

The number of problems that can be solved analytically using the Schrödinger equation is relatively low, being the atomic hydrogen one of them. When more than two particles are involved the Hamiltonian of the system depends on the relative distances of the different particles, and the number of variables to be solved start

growing fast. Along the years different methods have been developed to solve the problem numerically, such as perturbative and variational methods, or the Hartree-Fock Self-Consistent model [80].

The main difference when dealing with polyelectronic atoms is the role that plays the Pauli Exclusion Principle [81], which states that two or more identical fermions cannot occupy the same quantum state within a quantum system simultaneously. This principle lead to the well known electron distribution in shells around the nucleus [80], where only two electrons with opposite spin number can have the same quantum numbers. In Fig. 4.2 we can see the levels of the Helium atom, separated into two systems, one corresponding to Parahelium (singlet), with two electrons of opposite spins, and Ortohelium (triplet), with electrons of parallel spin. Atoms with higher number of electrons present even more complex structures.
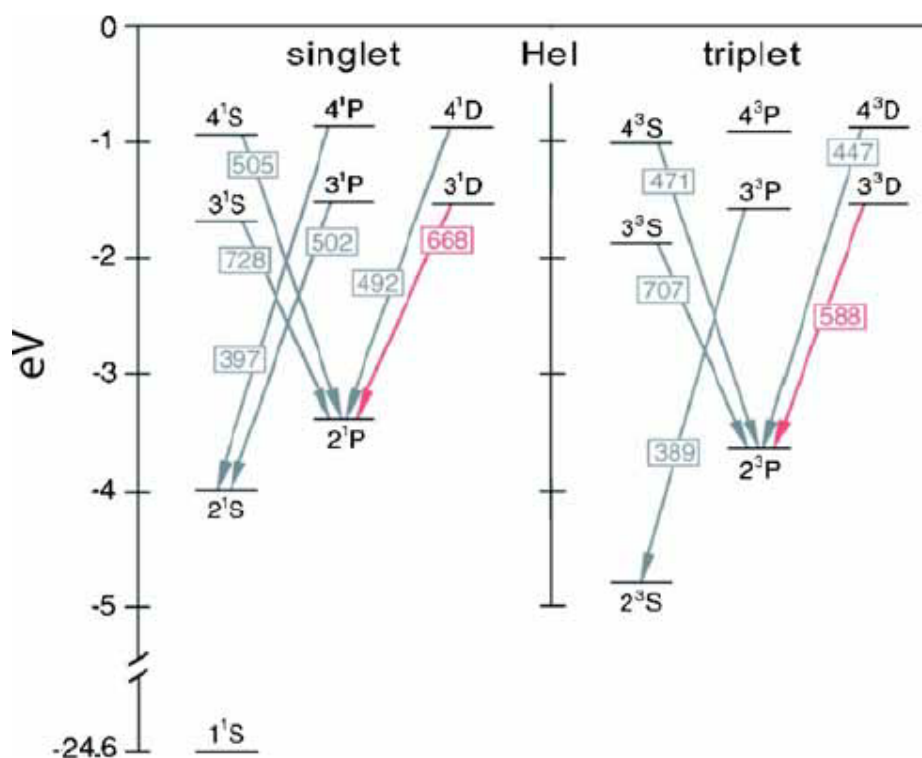
Figure 4.2: Energy levels of atomic helium.

In the case of molecules, their study is even more complex due to the presence of several nucleous, in which the relative movement between them has to be taken into account. This leads to the appearance of vibrational and rotational modes [80]. Nevertheless good results can be obtained using simplified models due to the different

time scale (orders of magnitude) between the movement of electrons and the vibration and rotation of nucleus [80]. Fig. 4.3 represents the energy level diagram as a function of the internuclear distance for the diatomic hydrogen molecule.
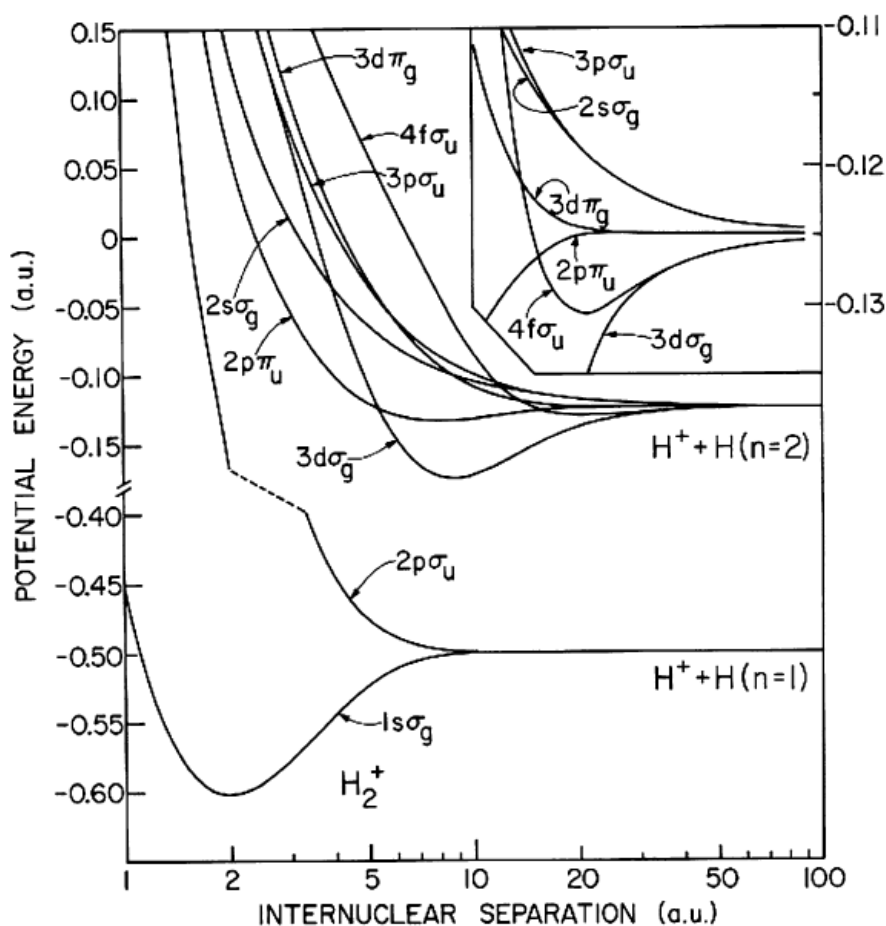
Figure 4.3: Energy levels as a function of internuclear distance in diatomic ionized hydrogen H_2^+.

While studying atomic and molecular structure, the measurements of the spectrum of emitted light is one of the most useful tools, because it allows us to directly measure the energy difference between two different levels, which corresponds to the energy of the photons emitted in the corresponding transition, as we can see in Fig. 4.4.
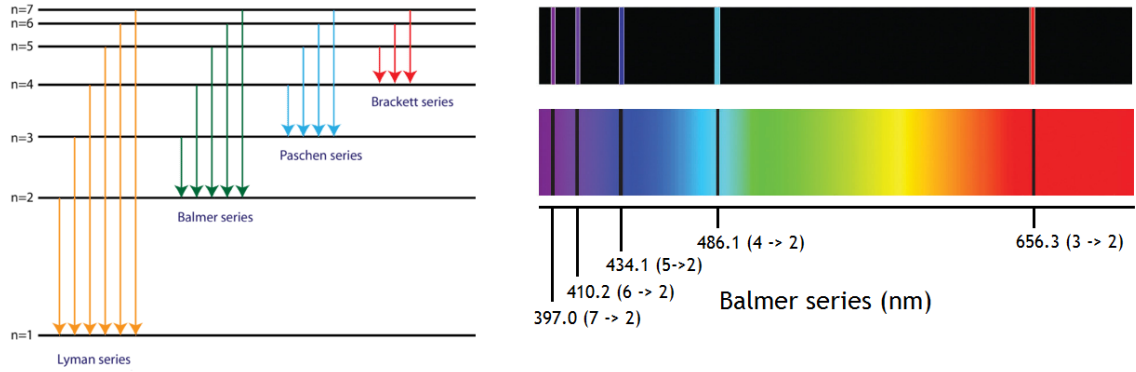
Figure 4.4: Spectrum of hydrogen in the visible region and its correspondence with the energy levels (Balmer series).

4.2 Interaction of atom with external electromagnetic field and transitions between levels

In the last section we have presented a short introduction to the study of the atomic and molecular structure using the time independent Schrödinger equation. However the atoms are never completely isolated from the outside world, but constantly affected by time varying fields. During the interaction of the atom with this time varying fields the electrons can absorb or emit energy and change their atomic numbers. This process is described by the Quantum Theory of Time-dependent Perturbations, where the temporal evolution of the system is described by the sum of the stationary hamiltonian H_0 and the time dependent perturbation H' [81]. By expanding the temporal evolution of the system and considering the perturbation small enough we obtain the analytical expression of the transition probability. In some particular cases, such as the harmonic interaction, we can simplify even further and obtain Eq. 4.7 and 4.8 for the transition probability per unit time in absorption $W_{if(abs)}$ and stimulated emission processes respectively $W_{if(em)}$ [81].

$$W_{if(abs)} = \frac{2\pi}{\hbar}\delta\left(E_f - E_i - \hbar\omega\right)\left|\langle f\left|H'\right|i\rangle\right|^2 \tag{4.7}$$

$$W_{if(em)} = \frac{2\pi}{\hbar}\delta\left(E_f - E_i + \hbar\omega\right)\left|\langle f\left|H'^{\dagger}\right|i\rangle\right|^2 \tag{4.8}$$

In the previous equations f and i denote the final and initial states, E_f and E_i are the energy of the final and initial states and $\hbar\omega$ the photon energy. In the particular case of beam fluorescence inside a pipe under high vacuum, due to the combination of low pressure of the residual gas in the beam pipe (typically below than 10^{-4} Pa) and low emission cross section (specially at high energies), the dominant process is the spontaneous emission, which can be interpreted as the transitions induced by the zero point of the radiation energy, or electromagnetic vacuum. In that case the emission probability per unit time is given by Eq. 4.9.

$$W_{if(esp)} = \frac{\pi e^2}{m^2 c^2} \sum_{\lambda,\mu} \frac{1}{\omega_\lambda} \left| \langle f \left| \mathbf{A}_{\lambda\mu}^* \cdot \mathbf{p} \right| i \rangle \right|^2 \delta \left(E_f - E_i + \hbar\omega \right) \qquad (4.9)$$

ω_λ is the angular frequency of the radiation and p the momentum. The sum is performed over all of the wavelengths and polarizations (λ and μ respectively). $A_{\lambda\mu}^*$ the corresponding component of the magnetic potential vector. With respect to the polarization and direction of the emitted light, the transition probability follows a squared cosine law function depending on the angle between the dipolar transition moment and the polarization [82]. If we consider that the electromagnetic fields of the vacuum are randomly polarized and isotrope, and the atoms randomly oriented, then the spontaneusly emitted ligth is also unpolarized and isotrope.

So far we have only considered dipolar transitions. In nature we find many examples where these dipolar transitions are forbidden but its corresponding spectral lines appear nonetheless. The explanation to this phenomena is that we have not considered multipolar transitions, which make possible those transitions between states, however, this higher multipole transitions have way less probability [80].

4.3   Beam interaction with the residual gas

We have just briefly introduced the process of light emission of an excited particle, but before the photons are emitted the atoms and molecules of the residual gas must be driven to excited states. As the beam transverses the beam pipe, its moving charged particles excite and ionize the gas particles, generating a very low pressure plasma.

The formalism to treat the interaction between a charged particle moving towards and an atom/molecule is given again by the quantum mechanics scattering theory [81]. Roughly speaking, the problem consists in calculating the probability of the final states of the gas particle. The calculations in general are long and complex, but in certain cases, such as the one with a relativistic projectile, simplifications can be used. For example in the relativistic case it has been discovered that the electric field of the charged particle can be treated as a bunch of photons of a certain spectrum travelling in the same direction as the beam [4]. In other situations, such as the low energy projectile, different phenomena take place, like charge exchange processes where the incoming particle "steals" an electron from the target whichs ends up in an excited state, then decaying and making the projectile particle the source of light.

Nevertheless, in practical cases when designing FPMs we are interested in a qualitative approximation of the signal that our device is going to measure. Hence in those cases usually a total cross section of the emission process is used. The values of the total fluorescence emission cross section are tabulated for several gases (although usually not in the whole energy range), but since individual lines are not, the spectrum composition should be taken into account in order to determine the photon frequency distribution. As just mentioned, in most of the cases the required values are not listed, but if we interpolate between two known points in case they are close enough. However, if the distance between them is too big, we need to be careful with the interpolation to obtain a realistic value. If we are in the range of its application, it is normally assumed that the total emission cross section follows the Bethe formula [29] (Eq. 4.10) when the cross section starts reducing at increasing energy (usually at hundreds of keV in the case of protons). In Fig. 4.5 the typical form of the Bethe formula is shown (in this particular case is for protons in graphite). The Bethe formula dependence of the velocity is obtained considering that the amount of momentum exchanged between the projectile and the target is the integral of the force during the time the interaction between them exists. Although the fluorescence process is much more complex and needs to take into account the internal structure of the atom, experimental measurements support to a certain degree the use of the approximation in the same range of validity that the Bethe formula [49]. The energy loss per unit length is given by:

$$\frac{dE}{dx} = \frac{4\pi e^4 N_A}{m_e c^2} z^2 \frac{Z}{A} \frac{1}{\beta^2} \left[2\ln\left(\frac{2m_e c^2 \beta^2 \gamma^2 T_{max}}{I^2}\right) - \beta^2 - \frac{\delta}{2} - \frac{C}{Z} \right] \qquad (4.10)$$
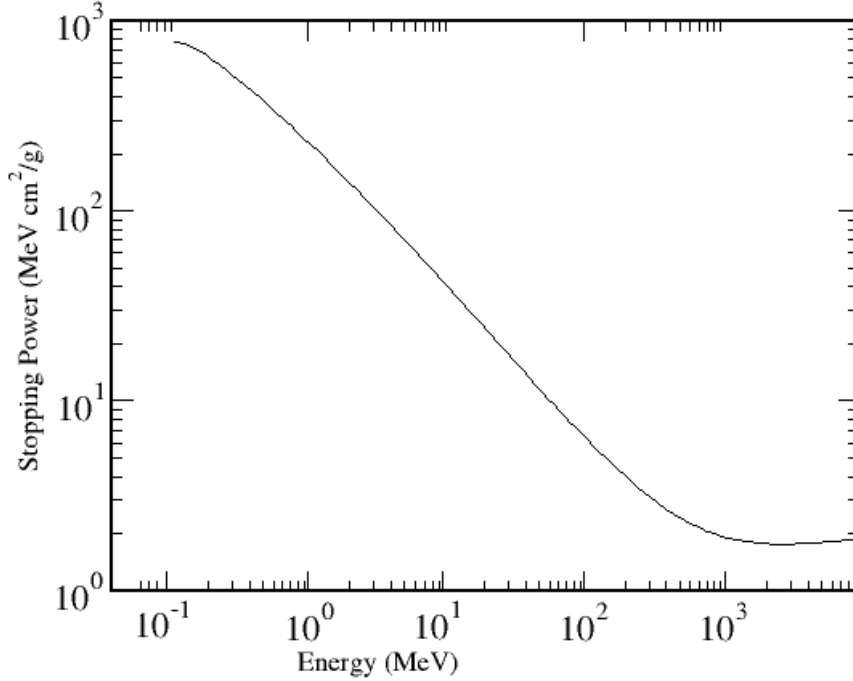
Figure 4.5: Stopping power of protons in graphite calculated using the Bethe formula.

Where the charge state of the projectile is z, its relativistic velocity β and factor γ, the atomic A and charge number Z of the target nucleus, the maximum energy transfer T_{max}, the mean excitation energy I and the density δ and shell boundary C corrections. When the cross section is known, either of a particular line or total, we can easily estimate the total number of photons emitted per unit time and length N_γ using Eq. 4.11:

$$N_\gamma = \frac{I_{beam}}{qe} n_{gas} \sigma \qquad (4.11)$$

Where I_{beam} is the beam current, q the charge state of the beam particle, e the electron charge, n_{gas} the number of gas particles per unit volume and σ the cross section. In most of the accelerators we will be in a high vacuum situation, where the pressure is in the order or below 10^{-4} Pa. The current is the parameter with varies most, however, as FPM are non-interceptive devices, they will be mainly used when dealing with high currents, a situation where interceptive diagnostics would be destroyed except at very low duty cycles. From the assumed Bethe dependence we can deduce that ions are one of the main targets for fluorescence monitoring, as electrons quickly become relativistic and situate on the lower part of the Bethe curve,

yielding a very poor number of photons unlike other diagnostics for electrons which are based on relativistic effects like synchrotron light or optical transition radiation are employed.

4.3.1 Accelerator applications

In the particular case of the accelerators involved in this thesis, the main component of the residual gas is expected to be Deuterium in the case of LIPAc and DONES, and Hydrogen in the case of AMIT. The accelerated particles are D^+ in the case of LIPAc and DONES, and H^- in the AMIT cyclotron, which is later stripped to H^+. In the case of LIPAc, the photon generation by protons in the SILHI source has been studied in depth in [83], which gave a value of the cross section of protons at 95 keV in Hydrogen of $1.5 \cdot 10^{-18}$ cm^2. By using the Bethe scaling accounting the different accelerated particle and residual gas we can obtain the extrapolated values of the fluorescence emission cross section for the different accelerators. Those results are written in Tab. 4.1. The current, energy and pressure for DONES are taken at the final position of the HEBT, in the TIR, whilst the values for LIPAc where from the injector.

Accelerator	E (MeV)	I_{beam} (mA)	P (Pa)	σ cm^2	N
LIPAc (@ Injector)		~ 125	$\sim 10^{-4}$	$1.5 \cdot 10^{-18}$	$2.8 \cdot 10^{12}$
LIPAc (@ D-Plate Ph.B)	4.5	~ 125	$\sim 10^{-6}$	$2.1 \cdot 10^{-20}$	$2.5 \cdot 10^{8}$
LIPAc (@ D-Plate Ph.C)	9	~ 125	$\sim 10^{-6}$	$7.4 \cdot 10^{-21}$	$1.4 \cdot 10^{8}$
DONES (@ HEBT)	40	125	$\sim 10^{-6}$	$1.3 \cdot 10^{-21}$	$2.5 \cdot 10^{7}$

Table 4.1: Extrapolated values of the fluorescence cross section using the Bethe formula.

Chapter 5

Profile distortion due to secondary electrons and excited particles movement

Alike the rest of detection systems, the fluorescence profile measurement is not infinitely accurate and precise, as there are many sources of noise and error that distort our measure. Inherent to the electronics we have the noise associated with the circuitry, as well as the dark noise of the detection. In the case of particle accelerator diagnostics, due to the long distance between the diagnostics their electronics, we can have Electro Magnetic Compatibility and grounding problems. In the optical systems we also find sources of errors and uncertainties, in this case they are characterized by the Point Spread Function of the system and its aberrations in the case of pure optical systems, but we should not forget the spectral transmittance of the lenses and viewports. The transmittance is optimized for the spectrum emitted in our particular case, but it is not constant over the spectrum and suffers from radiation degradation. With the cameras we face more problems than with the electronics because we also have to take into account the radiation damage on the sensor. MCP also suffers from radiation and its aging with their use is well known, but it is also important in its case to take into account the image blur due to the spread in the electron trajectories within the channels and the space charge effects that appear at high currents, making them unable of obtaining very sharp detail.

The effects described above deal with the data acquisition procedure. They are well known and can be minimized to some extent, either with careful circuit design, appropriate material selection... But there are some others, which we will describe below, that cannot be separated from the signal generation procedure and somehow we have to rely on theoretical corrections, wavelength filters and simulations when those errors start to have significant influence in the measurement. On the following we will focus on the errors introduced by the secondary electrons trapped in the beam potential and the finite light emission time, with two new different approaches to treat the errors arise from the former case.

5.1   Electron excitation

One of effects of a charged particle beam through a gas is the ionization and the creation of electron-ion pairs from the residual gas molecules. In the case of particle accelerators, due to the low pressure of the residual gas inside the beam pipe, the distance travelled before recombination is much greater than the beam pipe diameter. If we take into account the effects of the beam space charge field we find that the electron and ion pairs are separated due to the potential created by the beam charges, with the positive ions trapped in the beam in the case of electron and H^- beams, and with trapped electrons in the case of positive ion beams. These effects are normally neglected in beam optics calculations for low intensity beams, but are very important for high current beams, specially at low energies. One important consequence of the opposite polarity charge trapped in the beam is the Space Charge Compensation [84], which essentially is the reduction of the non linear self-defocusing electric field created by the beam, and plays an important role in the dynamics of particle acceleration and extraction of LEBT lines, leading to a partial mitigation of the emittance growth associated with non-linear fields. Additional information about space charge compensation is found in [85] and [86].

In the case of FPM, high current beams are desirable as the number of emitted photons per second is higher, but the resulting profile may be affected by the fluorescence of trapped particles, rendering useless the measured profile. We will limit our discussion to trapped electrons because the work of this thesis has been done with positive hadron machines, but in principle the equations are the same for opposite charge beam and particles. We will start studying the movement of the non

relativistic electron moving on a potential generated by a charge distribution with cylindrical symmetry. The radial electric field E_r generated by the distribution is given by the Gauss Law, which in the case of infinite uniform pencil beams of radius a has analytic solution in the form of Eqs. 5.1 and 5.2 [84].

$$E_r = \frac{I(1 - f_e)}{2\pi\varepsilon_0 c\beta_{beam}} \frac{r}{a^2} \quad for \quad r <= a \tag{5.1}$$

$$E_r = \frac{I(1 - f_e)}{2\pi\varepsilon_0 c\beta_{beam}} \frac{1}{r} \quad for \quad r > a \tag{5.2}$$

In the former equations I is the beam current, r the distance to the beam axis, ε_0 the vacuum dielectric permittivity, a the beam radius, βc the speed of the beam particles, $1 - f_e$ is a term that takes into account the reduction of the effective charge due to the space charge compensation. The azimuthal magnetic field B_{theta} associated with the beam is defined in Eqs. 5.3 and 5.4.

$$B_\theta = \frac{\mu_0 I r}{2\pi a^2} \quad for \quad r <= a \tag{5.3}$$

$$B_\theta = \frac{\mu_0 I}{2\pi r} \quad for \quad r > a \tag{5.4}$$

Here, μ_0 is the vacuum magnetic permeability. The ratio between the strength of the electrical field and the magnetic field is c/β_{beam}. The force acting over the generated electron and ion pairs in the transverse plane (by symmetry reasons there is no force acting out of the transverse plane) is given by the Lorentz force (in cylindrical coordinates) by Eq. 5.5.

$$\gamma m_e \ddot{r} = q_e E_r - q_e \dot{z} B_\theta \tag{5.5}$$

In Eq. 5.5, γ is the relativistic coefficient, m_e the electron mass, $\ddot{r}$ the second time derivative of the radial position, q_e the electron charge and $\dot{z}$ the beam velocity in the forward direction

The velocity distribution of the generated electrons depends on the beam energy, and can be found in [87]. In the non-relativistic case the magnetic field is

much smaller than the electric field, thus we can simplify Eq. 5.5 to the following differential equation:

$$m_e \ddot{r} = \frac{q_e I (1 - f_e) r}{2\pi \varepsilon_0 a^2 \beta_{beam} c} \quad for \quad r <= a \tag{5.6}$$

$$m_e \ddot{r} = \frac{q_e I (1 - f_e)}{2\pi \varepsilon_0 r \beta_{beam} c} \quad for \quad r > a \tag{5.7}$$

The last equations shows us a behaviour similar to an oscillator, which is even more clear if we consider the electrons to start with very little energy in the potential well created by the uniform beam, which left only the first equation (the electron can not move outside the beam), and the movement is the same of an harmonic oscillator. With high intensity beams the electron can get enough energy to interact with the atoms and molecules of the residual gas, leading to excitation, ionization and other processes in parallel with the beam effects. Each of these effects has an associated cross section that varies with energy, as in Fig. 5.1, so in general is very difficult to treat the problem, but fortunately only appears at high currents, low energies and away from external electric and magnetic fields that influence the electrons trajectories.

This error due to the electrons is dependent on the beam current and gas pressure, as an increase in the beam current gives an increase number of electrons trapped in the beam's potential, and with stronger space charge forces the stronger the electron oscillation can become. Discrepancies in the measured profile that can be attributed to secondary generated electrons that excite transitions involving spin flip have been found in [88]. However, one important characteristic regarding the spectrum of the emitted light is that electrons enable atomic and molecular transitions that involve spin flip, as we will see in the next chapter. By carefully selecting the transitions and with a system capable of resolving the emitted light (either with narrowband filters or imaging spectrometers), we can separate the contribution to the profile of the different wavelengths, and thus separate the contribution of the beam particles to that of the secondary generated particles. However in certain cases this effect can be used for our benefit, like in profile monitors for a hollow electron lens [89].
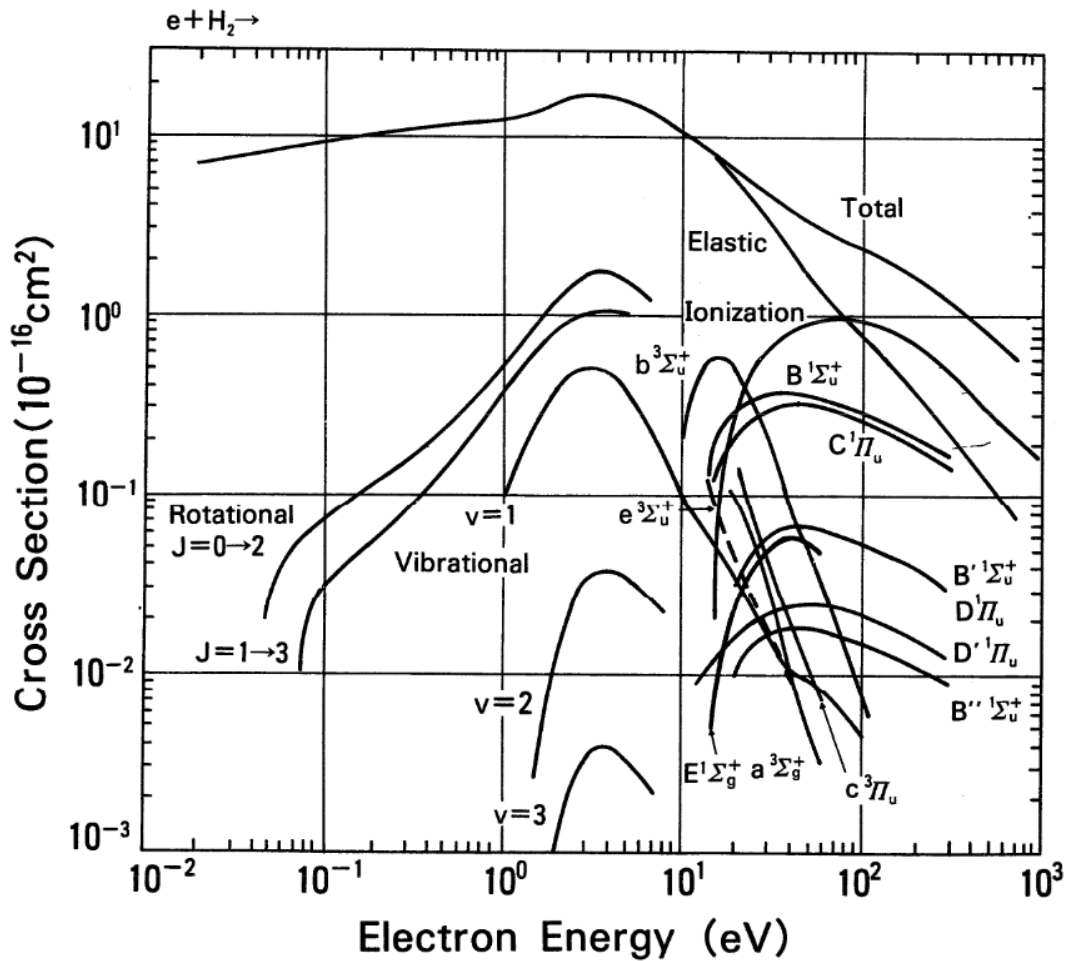
Figure 5.1: Interaction cross section between electrons and molecular hydrogen as a function of the electron energy [3].

5.2 Profile distortion due to excited particle movement

After the passage of a charged particle beam the excited atoms and molecules of the residual gas emit light with an spectrum distribution depending on its electronic structure and the beam properties. In principle all of the species contribute to the emission, but usually only one is the dominant as it is the most abundant component of the residual gas. From all of the excited transitions the ones with the highest product of intensity and spectral transmittance of the detector will give the strongest contributions. From the quantum theory of light emission and from empirical obser-

vation we know that each emission line has a finite lifetime with an exponential decay similar to the radioactive decay of nuclei. The consequence of this finite lifetime is a displacement from the initial particle position where the particle was excited to the position where the photon is finally emitted. This displacement depends on the initial momentum of the particle (taking into account the momentum change due to the collision) and the external electromagnetic forces when the excited particle is not neutral.

In general the process of light emission can be divided in three steps:

- **Collision:** The collision between the charged particle and the residual gas particles. This step is crucial for the theory and simulations because it determines the starting momentum distribution of the particles. The exact description of the interaction is in general very complicated to treat analytically due to the number of variables. Extensive studies in the case of ionization problems have treated the most simple case, the Three Body problem, and some experiments have characterised the kinematically complete problem using high resolution recoil-ion momentum spectroscopy (for example [90]). It has been found that depending on the kinetic energy and nature (electron or ion) of the incoming particle, some approximations can be used: at high energies we can treat the incoming particle as a radiation field (bunch of photons of different frequencies, as in Fig. 5.2) and very little momentum is exchanged [4], on the other hand at low energies we have a stronger "collision" in the classical way, strong electric interaction between the particles after the collision.

- **Excitation:** The next step of the process is the excited (and maybe ionized) particle propagation, where the particle of interest moves according to the external forces and its initial conditions. Here we have to separate between two cases, the neutral particles, which only drift according to their initial conditions (neglecting the very small effect of the gravity force), and the charged particles, which are subjected to the influence of electromagnetic fields such as the ones generated by the beam or the externally produced ones by magnet or electrodes. When the space charge forces are very small and external fields are weak the trajectory of the excited particles is not significantly affected by the external forces, they can be treated as neutral particles and calculate its drift according to the initial conditions. In the particular case of particular accelerators the
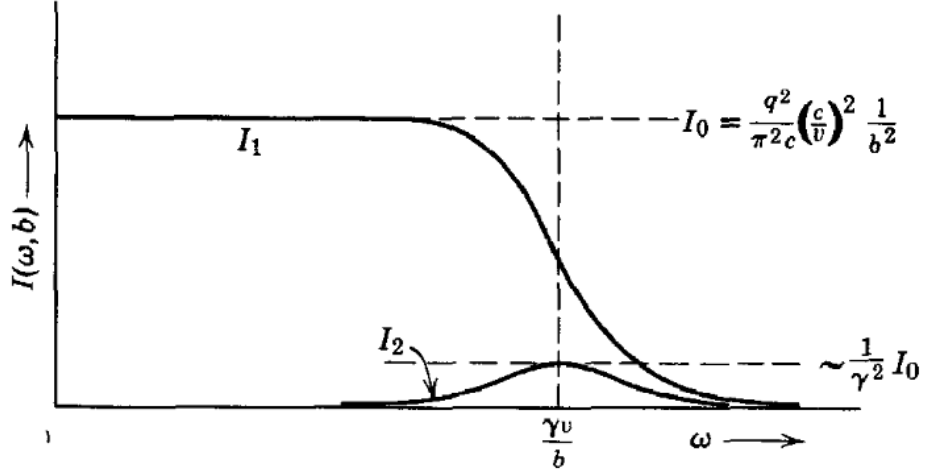
Figure 5.2: Frequency spectra (Intensity versus angular frequency) of a relativistic moving charge in the parallel I_1 and perpendicular I_2 direction. From [4]

vacuum is very good (less than 10^{-4} Pa) and we can neglect the collisions between excited particles as the mean collision distance between particles is far longer than the pipe transverse dimensions. However it may not be the case in external gas jets injected to locally enhance the pressure [64], thus this effect has to be taken into account when examining those systems.

- **Photoemission:** After some time, the particle emits the photon in a specific direction with a specific polarization. Averaging over the whole particle distribution the light emission is isotropic, and if the detector system used is not sensitive to the polarization we can disregard the polarization effects. The light is then collected by our optical system and detected by a sensor (camera, PMT,...), which converts it to electronic signals and sends them to the control system. In this step we have to take into account the optical aperture, detector geometry and spectral properties of our detector.

5.2.1   Correction schemes

The first correction scheme that we propose for the excited particle movement is based on a deconvolution correction to the measured profile. Our strategy will be to develop a correction similar to the optical Point Spread Function, where we will

examine the shape that a point of light has in the detection system. This theory is only applicable in the case of excited particles of the residual gas, because in the case of excited particles coming from charge exchange the theory is not applicable since their velocity distribution is not maxwellian and their transversal velocity is significantly smaller than the parallel one, which is almost equal to the particles of the beams. To develop the correction function of the movement of excited particles along the gas for the convolution we will start with several assumptions:

1. The gas has a Maxwellian distribution of velocities. It is justified because the residual gas is in thermal equilibrium and has very low density [91].

2. The momentum exchanged in the collision between the excited particle and the projectile is small compared with its initial momentum. According to [90] (and its references) the excited residual gas atom or molecule change in momentum decreases with increasing projectile energy (excluding nuclear interactions), so at sufficiently high energies or heavy targets the change in momentum of the excited particle is negligible compared with its initial momentum.

3. The residual gas has a molecular flow, therefore the mean free path without collisions of the particles is larger than the beam pipe diameter, which is also larger than the distance travelled by the particle until its decay [32]. In accelerator systems the gas is at very low pressures (typically less than 10^{-4} Pa) and in thermal equilibrium, hence this hypothesis is well justified. The distance travelled before decay is also less than the beam radius.

4. There is no posterior light emission after the first decay or the emitted light has no effect in the measurement. We only consider one excitation and one light emission. Any posterior light emission is not considered.

5. The photon emission follows an exponential decay law with respect to the time. The light emission is isotropic and the effects of polarization are neglected. This hypothesis is justified previously in Ch. 4.

6. Space charge effects and external field are neglected. This is only applicable in the case of low current beams (low self-field), no external electromagnetic field and/or the emission transitions belong to neutral atoms/molecules.

5.2.2 Analysis

We start the analysis examining the spatial distribution of the light emitted by the particles excited in a certain point along the beams path. If the light emission were instantaneous, with no time between excitation and emission, the spatial light emission distribution will be a Dirac delta located in the same position where the excitation occurs, and according with the fifth hypothesis the photons will be emitted isotropically with random polarization. However, in the real case the particles travel some distance after the excitation, depending on the time constant of the decay time. According to the hypothesis 1 and 2, after the collision the excited particle will have a thermal maxwellian distribution described by Eqs. 5.8 and 5.9.

$$f(v_x, v_y, v_z) = \left(\frac{m}{2\pi k_B T} \right)^{\frac{3}{2}} e^{-\frac{m}{2k_B T}(v_x^2 + v_y^2 + v_z^2)} \tag{5.8}$$

$$\int_{-\infty}^{\infty} f(v_x, v_y, v_z) dv_x dv_y dv_z = 1 \tag{5.9}$$

Since we neglect external forces, no particle can gain or lose energy and the velocity distribution remains constant. This means that the particle will follow rectilinear trajectories with constant velocity, so we can make the following change of variables $v_x = x/t, v_y = y/t, v_z = z/t$. Considering the time t as a parameter and x, y and z the new variables we get Eq. 5.10. Real collisions take a finite amount of time, thus we will not consider the instant $t = 0$. This gives us the spatial distribution at a given time that at time $t = 0$ in the position (0,0,0) started to drift with a maxwellian distribution.

$$f(x, y, z, t) = (\frac{m}{2\pi k_B T})^{\frac{3}{2}} \frac{1}{t^3} e^{-\frac{m}{2k_B T} \frac{x^2 + y^2 + z^2}{t^2}} \tag{5.10}$$

For practical applications of FPM we deal with one dimensional projections of the transverse profile. In the analysis we place the beam axis in the z axis position and we measure the projected profile in the x axis. If the beam profile is measured over a length much shorter than the betatron oscillation period its width can be considered constant over that period (or averaged with a small standard deviation). As we said before, the particles move, thus in our "slice of beam" we will have contributions from
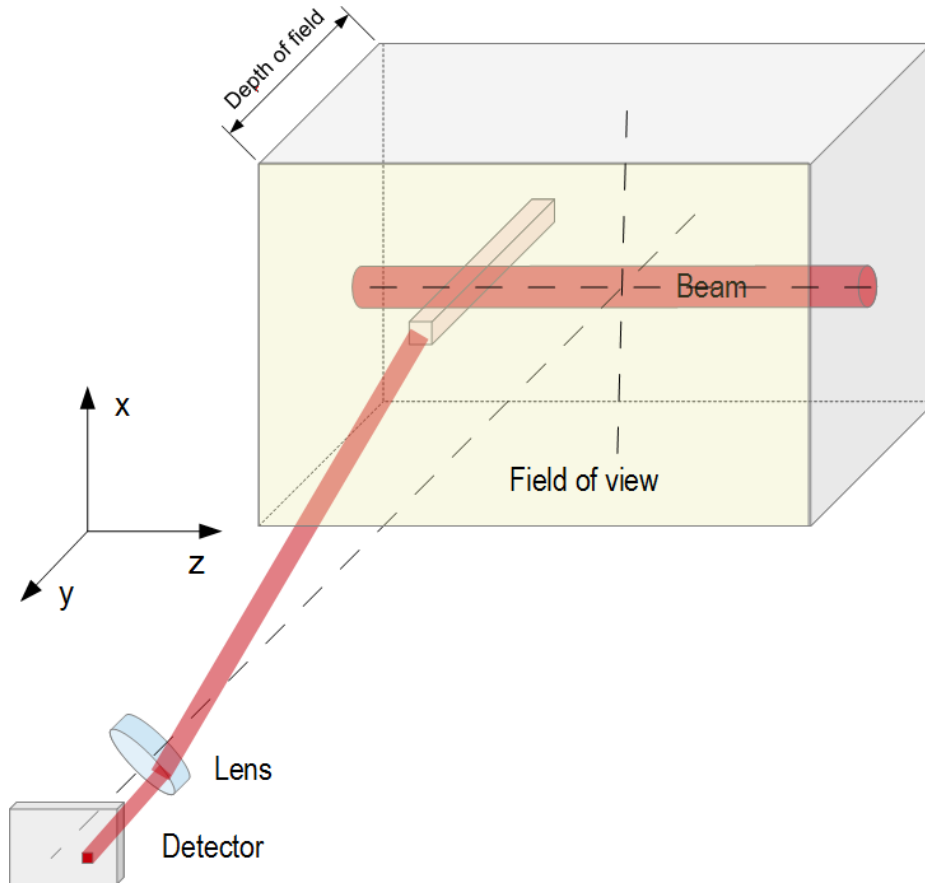
Figure 5.3: Schematic picture of the geometry

other points with different z coordinate, but as the average thermal movement during the transition time is quite short all of the excited particles generated in one point are detected in the slice. With this consideration we can ignore the contributions coming from the velocity in the z axis. In the transverse plane the contribution of the particles with different y positions can also be ignored, but the argument is different. With the optical systems typically used we have enough depth of field to accomodate all the beam and the excited particles. This means that we can only distinguish the x and z coordinates, since the light emitted at points with different y coordinate but with the same x and z coordinates will fall in the same detector position, therefore the velocity along the y axis of excited particles is irrelevant for the widening of the x profile. We further simplify by summing (or averaging) the data points along the z axis to create the final histogram of the projected profile. Fig. 5.3 shows a picture of the geometry of the problem. The way of taking this into account is integrating the velocity distribution function in the y and z directions, and then performing the change of variables to obtain the function only dependent on the x position and time

t in Eq. 5.11. A plot of the distribution of hydrogen atoms at different times is shown in Fig. 5.4.

$$f(x,t) = \left(\frac{m}{2\pi k_B T}\right)^{\frac{1}{2}} \frac{1}{t} e^{-\frac{m}{2k_B T} \frac{x^2}{t^2}} \tag{5.11}$$
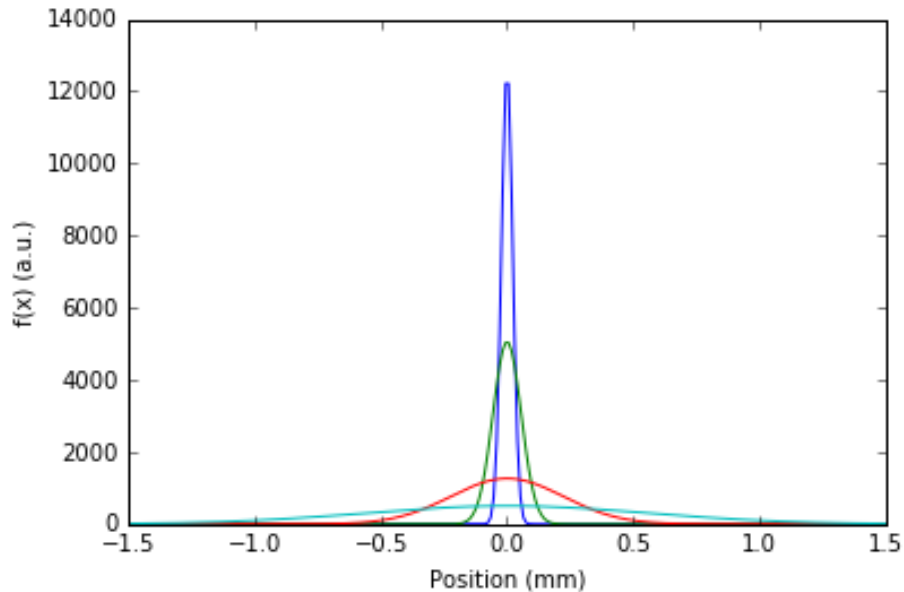
Figure 5.4: Distribution along x axis of hydrogen atoms ($m = m_p$, $T = 300K$) at different times from a point source released at t = 0. Blue = 20 ns, Green = 50 ns, Red = 200 ns and Turquoise = 500 ns.

   The former distribution, however, is not the final PSF that we are looking for, as it only gives us the spatial distribution at a given time. We also have to take into account the time taken by particles drifting from their starting positions before emitting light, which follows an exponential time decay law. It is also important to remark that when the observation is being done we are essentially looking at a stationary process and the signal is integrated in time to perfom and average of measurements (generally in times orders of magnitude longer than the transition lifetime), thus in our recordings we will be able to measure the full decay of all the particles that started drifting from the same position at the same time, therefore our PSF has to take these considerations into account. The way of doing is by weighting the profile at different times taking into account the amount of atoms/molecules that emit their photons at that time, as it is shown in figure 5.5. In the following analysis

only the exponential part of the decay function is used, leaving proportional terms out for reasons of simplicity, as they do not affect the beam width, which is what we are looking for.

$$PSF(x) \propto \int_0^\infty \left(\frac{m}{2\pi k_B T}\right)^{\frac{1}{2}} \frac{1}{t} e^{-\frac{m}{2k_B T}\frac{x^2}{t^2}} \lambda e^{-\lambda t}$$ (5.12)

With the change of variables $t = t'\sqrt{\frac{m}{2k_B T}}$ and $dt = dt'\sqrt{\frac{m}{2k_B T}}$ we get simplified expression for the PSF (Eq. 5.13):

$$PSF(x) \propto \int_0^\infty \left(\frac{1}{t'}\right) e^{-\frac{x^2}{t'^2}} \lambda e^{-\sqrt{\frac{m}{2k_B T}}\lambda t}$$ (5.13)
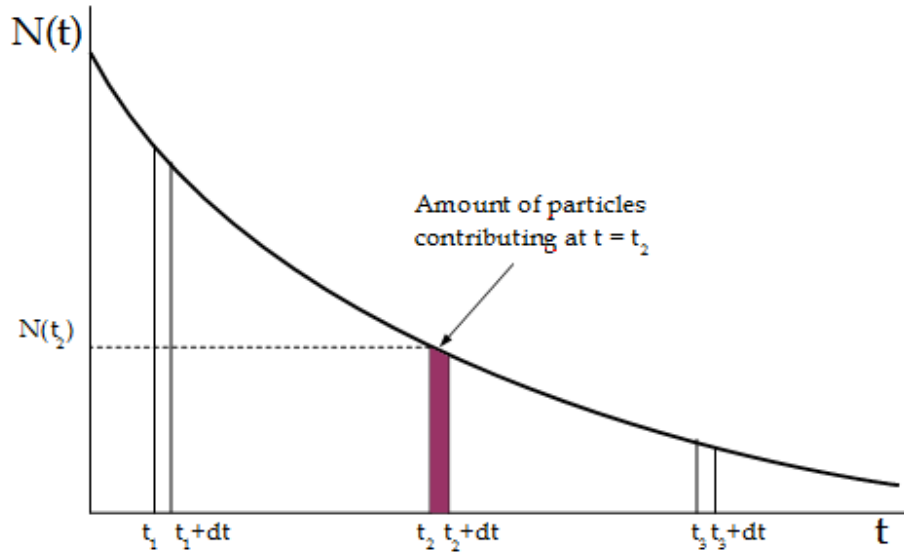
Figure 5.5: Distribution along x axis of hydrogen atoms ($m = m_p$, $T = 300K$) at different times from a point source released at t $= 0$. Blue $= 20$ ns, Green $= 50$ ns, Red $= 200$ ns and Turquoise $= 500$ ns.

This equation has not an immediate integral, and its rises several problems when evaluating due to its essential singularity in the origin. However, as the photon emission is not instantaneous but delayed with respect to collision, we can avoid the singularity and being coherent with the physics excluding the origin when performing the integration by setting the lower integration limit to a finite albeit short time. For example the classical collision time, so that the beam particle is far away and does

not disturb the electronic orbitals. In the case of different lines one can compute the total distortion by adding the contribution of the different transition times weighted by each line strength.

5.2.3 Simulation and model testing

To test the model represented by Eq.5.13 several beam profiles have been simulated. In all the cases we started with a gaussian beam profile and a maxwellian velocity distribution, and both the position and moments were randomly generated. A good example of the profile widening is shown in figure 5.6: on the left we have a gaussian profile of $\sigma = 0.3$ mm before (blue) and after (red) the particle propagation, whilst on the right another gaussian profile of $\sigma = 3.0$ mm before (blue) and after (red) has been simulated. In both cases a transition time $\tau = 200$ ns (exponential decay) and a thermal distribution of velocities with temperature $T = 300$ K, of the excited particles of $m = 2m_p$ has been considered. It is clearly seen the effect of the transition time on the widening of the smaller profile, as shown in table 5.2.3, with an increase of the σ of 45%. In the case of the wider profile the effect is almost imperceptible to the naked eye, but the substraction of both profiles (5.7) shows a decrease in the peak of the function and the widening of the function.
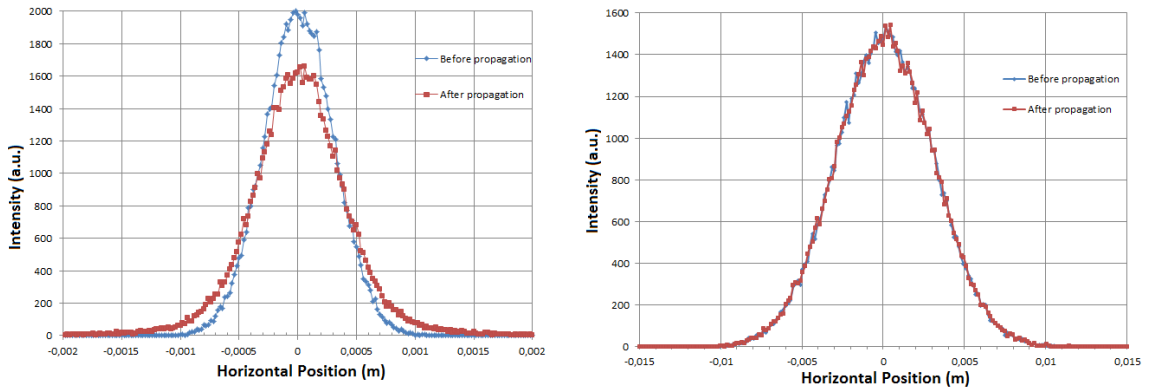
Figure 5.6: Comparison of two different gaussian profiles before and after the widening due to the transition lifetime ($\tau = 200$ ns, $T = 300$ K, $m = 2m_p$).

In order to compare the results predicted by Eq. 5.13 with the simulations in Fig. 5.8 we have represented four different profiles: in blue the particle distribution randomly generated from a gaussian distribution, in red the particle distribution after

$\tau = 200$ ns	$\sigma = 0.3$ mm	$\sigma = 3.0$ mm
σ_{before} (mm)	0.300	3.00
σ_{after} (mm)	0.436	3.02

Table 5.1: Beam width comparision before and after excited particle propagation.
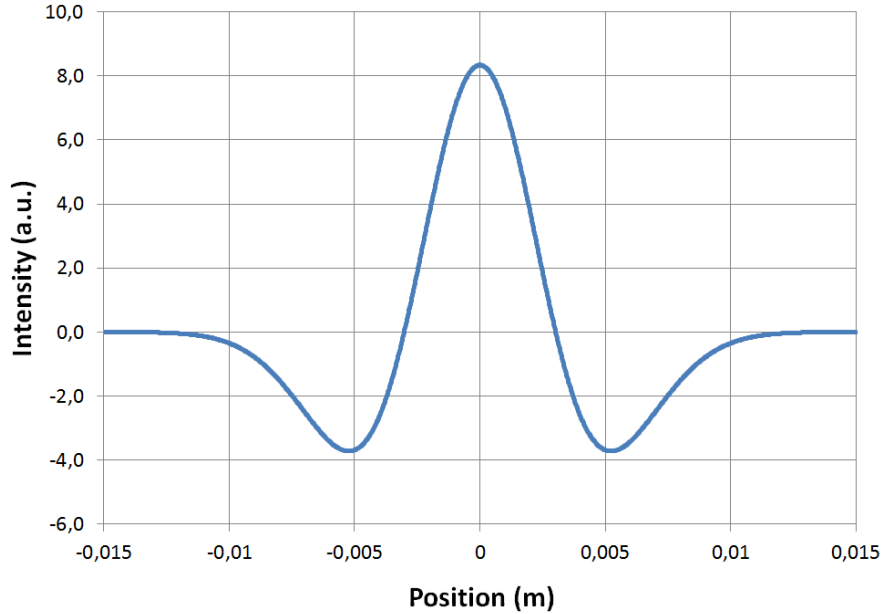
Figure 5.7: Difference between the profiles before and after propagation for an analytical gaussian of $\sigma = 3.0$ mm (Value before minus Value after).

propagation of the particles according to a maxwellian velocity distribution, in green the original gaussian profile and in purple the profile resulting from the convolution between the original gaussian profile and the PSF, Eq. 5.13. The parameters of the original gaussian function, residual gas and transition time were the same as in the left simulation shown in Fig. 5.6. The gaussian and convolved distributions have been scaled with the same factor so the maximum of the gaussian coincides with the peak of the distribution before propagation. Results show good agreement between the theory and the simulations.
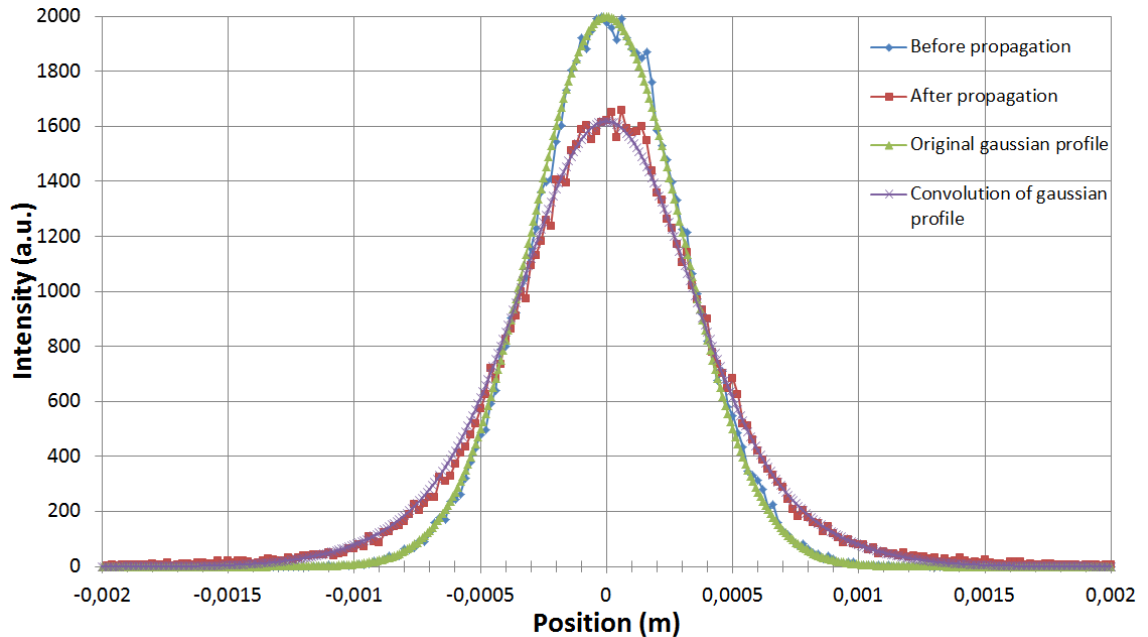
Figure 5.8: Comparison between the predicted and simulated profiles. Original and convolution are analytical values.

5.3 Evolution of the particle distribution second moment between excitation and emission

In this section we will discuss the distribution of excited particles in a collective way, obtaining the temporal evolution of the RMS distribution. The treatment is similar to the one used to study analytically the effect of the space charge in a charged particle beam. However we will use the position and the velocity/momentum instead of the position and the divergence angles as used in beam dynamics. The original theory of the space charge effects on beams in which our analysis is based on can be found in [92] [93]. The starting points are the Newton equation of the movement of a single particle, Eq. 5.14, with the mass included in the F_{ext} term for the sake of clarity, and the definition of the emittance, Eq. 5.15 [13]. We will ignore relativistic effects as the particles velocities are at least two orders of magnitude below the speed of light:

$$\ddot{x} - F_{ext} = 0 \tag{5.14}$$

$$\varepsilon^2 = \overline{x^2} \cdot \overline{\dot{x}^2} - (\overline{x\dot{x}})^2 \tag{5.15}$$

In the equations before x is the position coordinate of the particle, the number of upper dots denotes the number of derivatives with respect to the time, F_{ext} stands for the external forces (in general time, position and velocity dependant), and ε is the emittance. The evolution with respect the time of the distribution moments is easily derived:

$$\frac{d\overline{x^2}}{dt} = 2\overline{x\dot{x}} \tag{5.16}$$

$$\frac{d\overline{x\dot{x}}}{dt} = \overline{\dot{x}^2} + \overline{x\ddot{x}} = \overline{\dot{x}^2} + \overline{xF_{ext}} \tag{5.17}$$

$$\frac{d\overline{\dot{x}^2}}{dt} = 2\overline{\dot{x}\ddot{x}} = 2\overline{\dot{x}F_{ext}} \tag{5.18}$$

By substituting $a^2 = \overline{x^2}$, taking the second derivatives and using our definition of emittance we arrive to Eq. 5.19, which describes the evolution of the second moment of the distribution:

$$\ddot{a} - \frac{\varepsilon^2}{a^3} - \frac{\overline{xF_{ext}}}{a} = 0 \tag{5.19}$$

For the emittance we can easily derive the temporal evolution just by taking the first derivative:

$$\dot{\varepsilon^2} = 2(\overline{x^2} \cdot \overline{\dot{x}F_{ext}} - \overline{x\dot{x}} \cdot \overline{xF_{ext}}) \tag{5.20}$$

With the last pair of equations we can study the evolution of the transverse distribution's second moment of the excited particles of the beam. The initial values are the same as the beam in the position that were excited, so a good estimation of the original beam profile can be achieved.

Eq. 5.19 can be integrated analytically given certain conditions, in particular the time invariant of the emittance and the external forces. In a situation where non-linear forces are absent we can assure the conservation of the emittance. If no external forces are present the differential equation is simplified and can be integrated to obtain the time dependence of the position's second moment of the distribution (Eq. 5.24). The initial condition for the integration is the initial second moment a_0^2 in $t = 0$. Depending on the initial emittance and initial size the behaviour is different, as shown in Fig. 5.9, where the evolution of the standard deviation of two gaussian distributions has been computed, considering a excited residual gas with temperature of 300 K and two different gases.

$$\ddot{a} - \frac{\varepsilon^2}{a^3} = 0 \tag{5.21}$$

$$\dot{a} = \sqrt{k - \frac{\varepsilon^2}{a^2}} \tag{5.22}$$

$$t = \frac{a_0^2 a}{\varepsilon} \sqrt{\frac{1}{a_0^2} - \frac{1}{a^2}} \tag{5.23}$$

$$a^2 = a_0^2 + \frac{\varepsilon^2 t^2}{a_0^2} \tag{5.24}$$

If we consider constant the therm associated with external forces with no emittance growth we can only obtain the first integral (Eq. 5.25), requiring numerical integration to obtain the second moment evolution. This is the situation where only constant and/or linear forces are present.

$$(\dot{a})^2 + \frac{\varepsilon^2}{a^2} - \overline{xF_{ext}} \log(a) = cte \tag{5.25}$$

In general the emittance will grow with time in presence of nonlinear forces. It can be easily shown by expressing the force by means of a Taylor's series and substituting in the equation of the time derivative of the square of the emittance. In Eq. 5.29 is easily seen that the time derivative of the emittance is 0 for n = 0, 1.
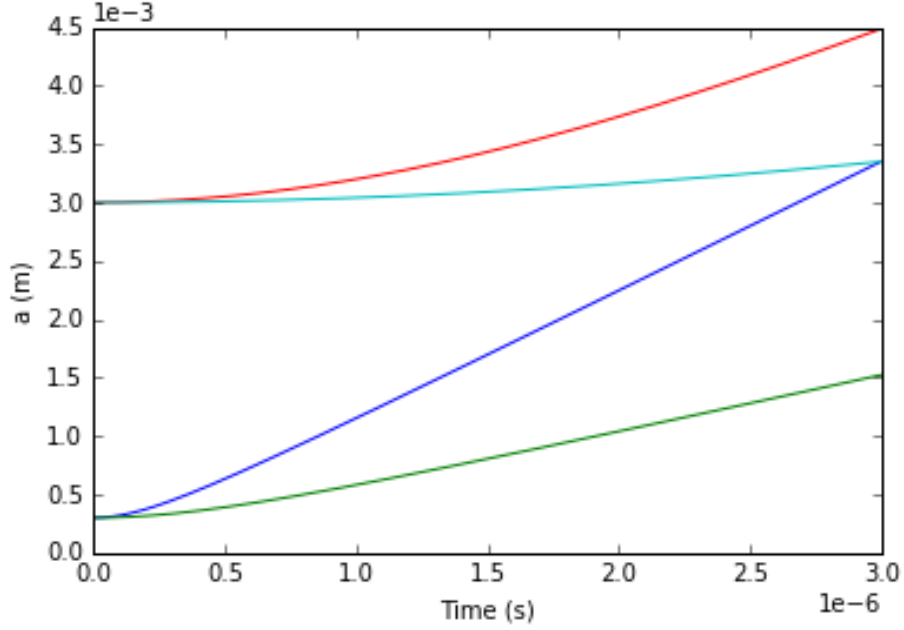
Figure 5.9: Evolution of the standard deviation ($\sqrt{a}$) of two beam profiles with $\sigma = 3$ and 0.3 mm for molecular Hydrogen (blue and red) and Neon (green and cyan).

$$F_{ext} = \sum_{n=0}^{\infty} a_n x^n \tag{5.26}$$

$$\dot{\varepsilon^2} = 2(\overline{x^2} \cdot \overline{\dot{x}F_{ext}} - \overline{x\dot{x}} \cdot \overline{xF_{ext}}) = 2(\overline{x^2}\dot{x}\overline{\sum_{n=0}^{\infty} a_n x^n} - \overline{x\dot{x}x}\overline{\sum_{n=0}^{\infty} a_n x^n}) \tag{5.27}$$

$$\dot{\varepsilon} = 2(\overline{x^2}\sum_{n=0}^{\infty} a_n\overline{\dot{x}x^n} - \overline{x\dot{x}}\sum_{n=0}^{\infty} a_n\overline{xx^n} \tag{5.28}$$

$$\dot{\varepsilon^2} = 2\sum_{n=0}^{\infty} a_n(\overline{x^2} \cdot \overline{\dot{x}x^n} - \overline{x\dot{x}} \cdot \overline{xx^n}) \tag{5.29}$$

As in the previous subsection we still need a final step to adapt the evolution of the second moment to the real problem when the excited atoms follow an exponential decay. Due to the finite transition time the measured second moment of the distribution is a weighted average of the second moment evolution by the function describing the decay (a decreasing exponential in this case) properly normalized.

63

$$a_{meas}^2 = \int_0^\infty a^2(t)\lambda e^{-\lambda t}dt = \int_0^\infty (a_0^2 + \frac{\varepsilon^2 t^2}{a_0^2})\lambda e^{-\lambda t}dt \qquad (5.30)$$

With the change of variables $t' = \lambda t$ we further simplify and resolve the integral to obtain Eq. 5.32.

$$a_{meas}^2 = \int_0^\infty (a_0^2 + \frac{\varepsilon^2}{a_0^2 \lambda^2}t'^2)e^{-t'}dt' \qquad (5.31)$$

$$a_{meas}^2 = a_0^2 + \frac{2\varepsilon^2}{a_0^2 \lambda^2} \qquad (5.32)$$

In order to apply the developed theory to real world beam examples, we have calculated the profile widening due to the thermal drift of three different beams: the AMIT cyclotron just before the target position, the LIPAc injector just after the accelerator column and the DONES HEBT in the middle of the TIR room. The beam profile characteristics are resumed in Tab. 5.2. In this simulation we have chosen only three spectral lines, the H_α at 656.3 nm with a lifetime of 22.7 ns, the H_β at 486.1 nm with a lifetime of 119 ns, and the N_2^+ line at 391 nm with a lifetime of 60 ns. We have chosen the hydrogen lines because hydrogen is the predominant gas in the three accelerators, and the nitrogen one because nitrogen is one of the most common residual gases and the line it is one of the most prominent lines in the beam fluorescence.

	σ_x (mm)	σ_y (mm)
LIPAc (@ injector)	28	28
DONES (@ TIR)	33	26
CNA	7	7

Table 5.2: Beam profile rms at the specified positions.

The results of the widened profile with respect to the initial profile (in %) are resumed in Tab. 5.3. As we can see, for those lines and those sizes the thermal drift effect is negligible.

Assuming a residual gas in thermal equilibrium and a negligible influence of the beam in the collisions, we can reorder the variables in Eq. 5.32 and develop the

64

	Horizontal error (%)	Vertical error (%)
H_α		
LIPAc (@ injector)	$8.14 \cdot 10^{-5}$	$8.13 \cdot 10^{-5}$
DONES (@ TIR)	$5.85 \cdot 10^{-5}$	$9.43 \cdot 10^{-5}$
CNA	$1.30 \cdot 10^{-3}$	$1.30 \cdot 10^{-3}$
H_β		
LIPAc (@ injector)	$2.24 \cdot 10^{-3}$	$2.23 \cdot 10^{-3}$
DONES (@ TIR)	$1.61 \cdot 10^{-3}$	$2.59 \cdot 10^{-3}$
CNA	$3.58 \cdot 10^{-2}$	$3.58 \cdot 10^{-2}$
N_2^+		
LIPAc (@ injector)	$4.08 \cdot 10^{-5}$	$4.08 \cdot 10^{-5}$
DONES (@ TIR)	$2.92 \cdot 10^{-5}$	$4.72 \cdot 10^{-5}$
CNA	$6.51 \cdot 10^{-4}$	$6.51 \cdot 10^{-4}$

Table 5.3: Profile error due to thermal drift of the particles.

emittance term assuming no correlation between the position and the velocity of the gas particles. After these steps we can calculate the transition lifetime which causes a beam distortion of $p\%$ ($error = 100 \cdot \frac{a_{meas} - a_0}{a_0}$) as a function of the beam's rms (a_0), molecule mass (n times m_p) and gas temperature T, obtaining Eq. 5.34. For the beams considered before, we have calculated the transition lifetime that produces a 1% error due to the thermal drift of the excited particles. Results are shown in Tab. 5.4. Results were checked with the simulations, where we propagated the particles with an exponential decay equal to the calculated with the theory for the 1% error. They were in good agreement, and were error less than 1% in all the cases.

$$t = \sqrt{\frac{a_0^4 \left[(1 + 0.01p)^2 - 1\right]}{2\varepsilon^2}} = \sqrt{\frac{a_0^4 \left[(1 + 0.01p)^2 - 1\right]}{2\left(a_0^2 \frac{k_B T}{n m_p} - \left(\overline{x\dot{x}}\right)^2\right)}} \quad (5.33)$$

$$t = a_0 \sqrt{\frac{n m_p}{2 k_B T} \left[(1 + 0.01p)^2 - 1\right]} \quad (5.34)$$

	Horizontal profile (s)	Vertical profile (s)
Hydrogen		
LIPAc (@ injector)	$2.52 \cdot 10^{-6}$	$2.52 \cdot 10^{-6}$
DONES (@ TIR)	$2.97 \cdot 10^{-6}$	$2.34 \cdot 10^{-6}$
CNA	$6.41 \cdot 10^{-7}$	$6.41 \cdot 10^{-7}$
Nitrogen		
LIPAc (@ injector)	$9.43 \cdot 10^{-6}$	$9.43 \cdot 10^{-6}$
DONES (@ TIR)	$1.11 \cdot 10^{-5}$	$8.76 \cdot 10^{-6}$
CNA	$2.36 \cdot 10^{-6}$	$2.36 \cdot 10^{-6}$

Table 5.4: Transition lifetime for a 1% error in Hydrogen and Nitrogen.

5.3.1 Profile distortion in the LIPAc and CNA measurements

Using the measurements done at LIPAc and CNA, which were described in Ch. 6 and Ch. 8 respectively, we were able to measure the transverse beam size with two different FPM, one based on an intensified camera and one based on a PMT array.

In the case of both measurements the theory was used to estimate the beam width increase due to the thermal gas particle movement, as it is shown in Tab. 5.3, but comparing to the typical error in our measurements, we are still far away of the limit where the distortion starts to be significant. In the case of LIPAc, the typical error obtained when measuring the profile is in the order of 0.6 %, whilst for the case of the CNA measurements the minimum error obtained is 3% for a gain voltage of 550 V and an integration time of 15 ms. In both cases the profile distortion is 4 orders of magnitude lower than the error in the measurement, so it is impossible to appreciate any kind of distortion. Additionally, in the case of lower energy beams and/or higher pressures, like the one in the LIPAc injector, although the theory could be applied, the contribution due to the light emission of the particle that does not belong to the residual gas play a role in mitigating the distortion suffered by the beam, as they do not drift in the same manner after excitation.

These results show that the effect of the distortion plays an important role in the case of very narrow beams (less than mm), since the typical emission lifetimes

of the atomic and molecular lines are very short in time. This distortion effect is minimized at higher residual gas mass.

Chapter 6

Experimental measurements of low energy Deuterons

An FPM detector based on an intensified CID camera was installed in the LIPAc injector to compare its performance with CCD cameras, as CID devices alone were not capable to obtain an image of the beam. These measurements were done with the most basic configuration of the SILHI source [57], with no LEBT, to assess the performance of the accelerating column and do a crosscheck between the measurements and the Tracewin [94] simulation code. In this short campaign of experiments the only component after the source were a diagnostic chamber with the emittance metter [95], the FPM based on the ICID detector, the Doppler Spectrometer [74] and the Beam Dump, which provides the current measurement. An image of the injector configuration can be seen in Fig. 6.1.

This chapter of the thesis is dedicated to the study of the results obtained with the ICID and the Doppler Spectrometer. The transverse profile measurements were done in pair with the more time consuming emmitance scans for different ion source parameters scanning. An sketch of the configuration of the source can be seen in Fig. 6.2. The biggest impact on the profile came from the variation of the intermediate electrode voltage and the beam current, as will be seen later on. All the measurements were done in pulsed mode with different duty cycles and periods. Additional parameters that were varied during the experiments were: the Reppeller Electrode voltage, the RF power and, gas flow of the source (Deuterium) and the
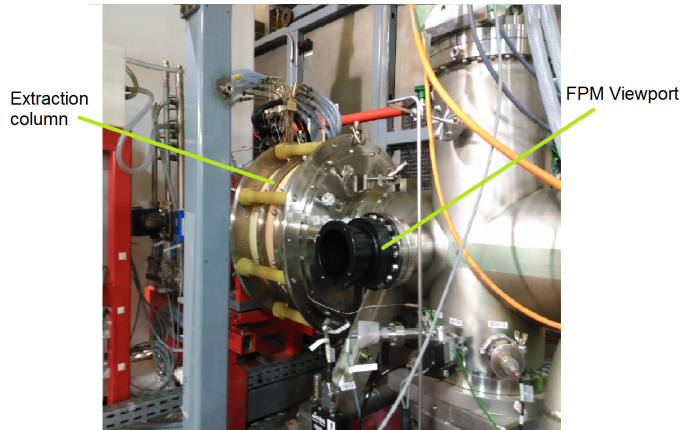
Figure 6.1: LIPAc injector during experimental campaign. FPM was installed in the black support. The only elements out of the vacuum are the FPM and the Doppler spectrometer.

space charge compensation gas (Krypton).

6.1 Experiment Setup

The main detectors used in the experiment were the ICID camera, used to measure the profile, and the spectrometer used to measure the spectral properties of the fluorescence light. Both apparatus were controlled individually since at that time they were not integrated in the LIPAc control system.

6.1.1 Intensified CID Camera

The measurements of the transverse profile were done using an Intensified Charge Injection Device Camera ICID, seen in Fig. 6.3. This not a monolithic device, but an assembly of different parts. The optical front end is a 25 mm fixed focal length from Edmund Optics [96] with variable aperture, which forms the image in the front plate of the intensifier. The intensifier itself is based on a Micro Channel Plate model BV 2581 BX-V 100 N from Proxitronic (now Proxivision) [97] whose main characteristics are enumerated in Tab. 6.1, and its quantum efficiency displayed in Fig. 6.4. The back end of the intensifier is a P46 phosphor screen where the intensified image of
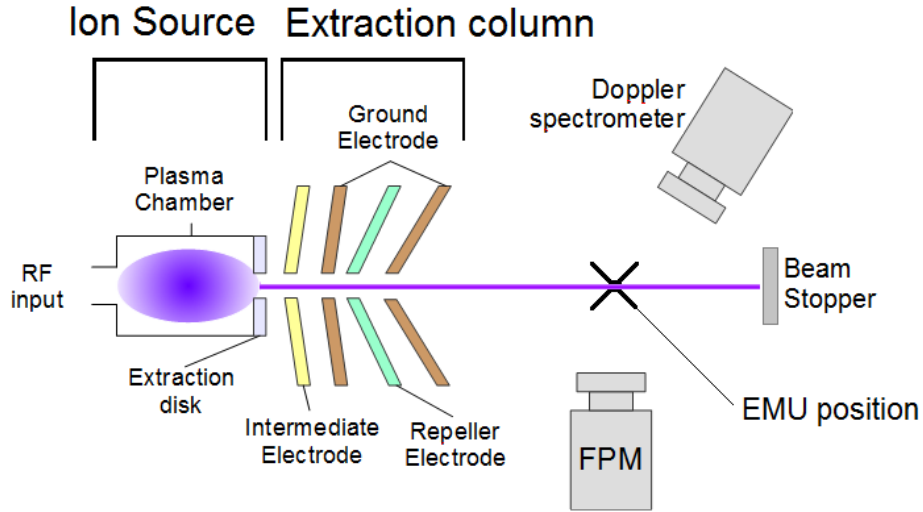
Figure 6.2: Schematic drawing (top view) of the LIPAc injector during the measurement campaign. The beam current is measured at the beam stopper.

the beam is formed. The next stage of the assembly is a Schneider Kreuznach [98] macro lens from the Unifoc series, which forms the final image an the detector, a CID camera 8726DX6 from Thermo Scientific [99] (now Thermo Fisher Scientific) with its characteristics enumerated in Tab. 6.2. The whole assembly calibration was done with an optical calibration pattern and a constant of 0.32 mm/pixel, with enough depth of field and field of view to cover the whole beam, was obtained.

Input diameter	25 mm
Window material	Quartz
Photocathode material	Bialkali (K_2SbCs)
Type	V-Stack
Phosphor screen	P46
MCP max. voltage	1800 V
MCP max. gain	10^6
Min. Gate time	100 ns
Trigger frequency (min - max)	200 Hz - 14 kHz

Table 6.1: Proxitronic MCP specifications.

The image acquisition is done by capturing the analog output of the camera

Pixels	726 x 575
Pixel size	17.3 x 17.3 μ m^2
S/N ratio	-45 dB signal / RMS
Radiation hardness (min.)	30 kGray
Output	Analog and digital (USB 2.0)

Table 6.2: Thermo Scientific CID specifications.
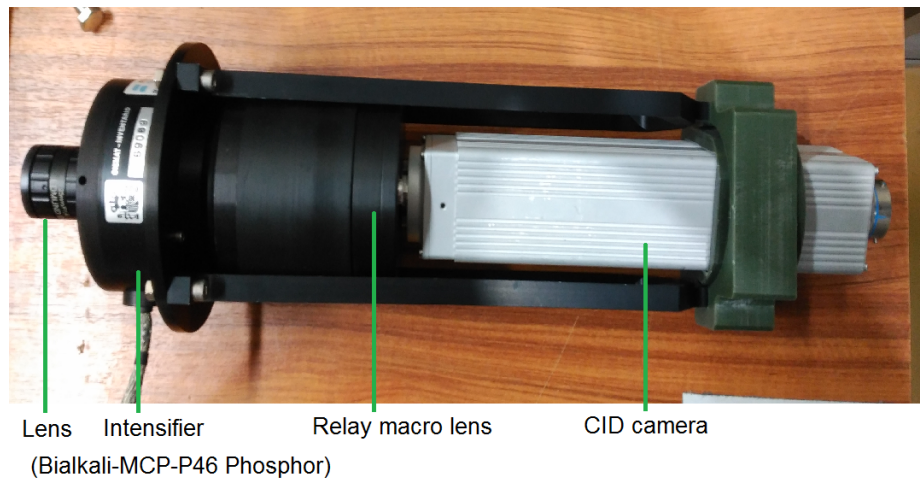
Figure 6.3: ICID assembly.

electronic box with a National Instruments [100] video acquisition card, which is controlled with LabView. The Labview program (created by CEA [59]) has many features, including background substraction, automatic profile fitting and average over multiple frames. The data post processing was done at CIEMAT with a Python script that includes multiple ROI selection, automatic profile fitting and automatization routines for data processing.

6.1.2   Synchronization board

The whole system was synchronized with the LIPAc timing system. The board was designed and built at CIEMAT and is based around STM32F334R8 microcontroller [101] with an auxiliary interface board to protect the inputs (trigger and gate) and generate the required 5V TTL (50 Ohm) signal for the MCP. The MCU generates both the gain analog DC signal and the train of pulses with variable period and duty
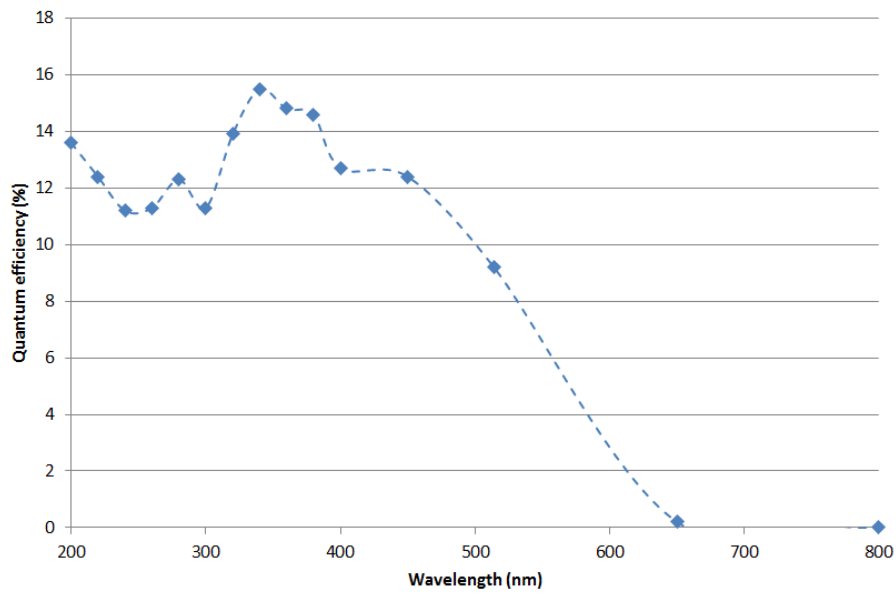
Figure 6.4: Proxitronic BV 2581 BX-V 100 N quantum efficiency.

cycle in order to synchronize the gating with the beam arrival.

During operation the device performed extremely well. The light yield of the residual gas was more than enough to be detected with our ICID without getting even close to the maximum settings. Due to the proximity to the plasma chamber, the background was measured with the plasma ignited but without beam extracted. However, as can be seen in Fig. 6.5, the main noise source was the reflection on the chamber walls, which were not darkened in order to minimize the reflection of stray light. Nevertheless, a dark coating would be of little interest in that particular vacuum chamber due to the presence of the emittance scanner, which is an Allyson type scanner with tungsten plates facing the beam. Although tungsten is known to be resistant to sputtering, the continuous bombardment with 100 keV ion scrap material and deposit it all around the chamber, making a mirror-like deposition that has a very high reflectivity, and even affecting the viewport where the FPM was located, requiring a cleaning of the glass to remove the deposited tungsten. On recent campaigns has been observed that the effect of the beam chopper also adds more light to the background [102].
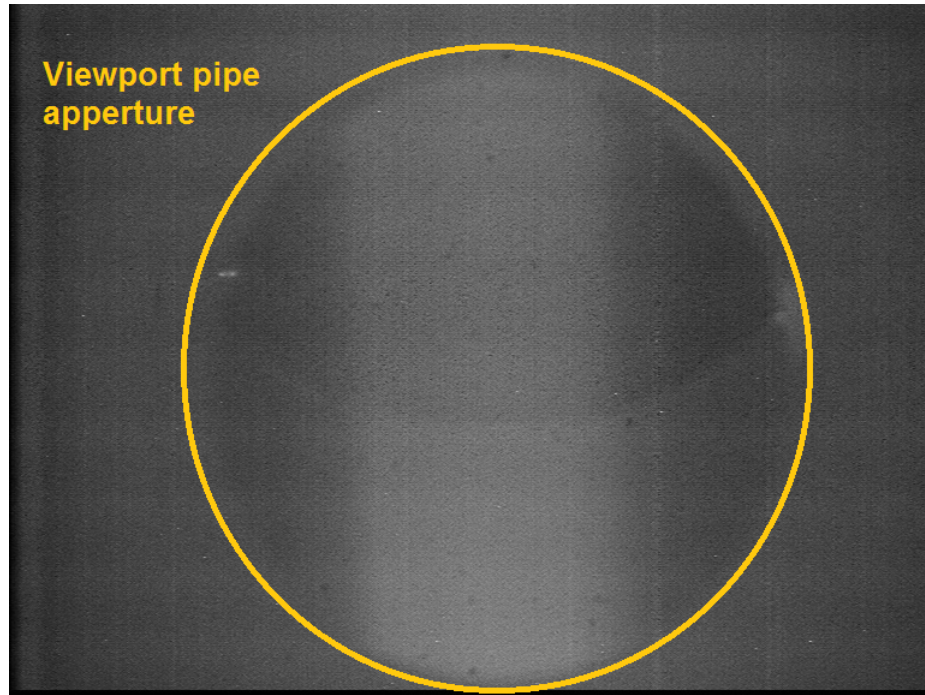
Figure 6.5: Raw profile taken by the ICID camera. The beam is the vertical big fringe seen in the center. Stray light reflections and the physical aperture of the beam pipe are clearly seen.

6.1.3 Doppler Spectrometer

The other non-interceptive, fluorescence based diagnostic that was installed was a spectrometer [74] in order to measure the fraction species of the beam, although it is also capable of measuring the beam profile. The device is located at the electronics room with all of the electronics of the accelerator, safe from the radiation. Thus a system to guide the light from the beam is needed. In this case an image fiber from Fujikura [103] was selected. The spectrometer is a iHR320 from Horiba Scientific [5], depicted in Fig. 6.6. Its associated detector is a cooled CCD camera from Horiba Scientific. The combination of diffraction grating and detector yield a resolution of 0.032 nm. The spectrometer and detector were controlled using a PC with Horiba's propietary software, and the spectral data processing was done using Python. In order to separate the lines with Doppler shift the spectrometer is located at an angle of 20º with respect to the beam direction in the horizontal plane.

Figure 6.6: iHR320 Spectrometer [5].

6.2 Measurements

As we said before, the main objective of the experimental campaign was to perform profile and emittance measurements in order to compare with the data obtained in the simulations. This step was considered crucial to the next stage of commissioning of the accelerator, since errors and mismatches at LIPAc's high current (125 mA) could seriously damage the machine. In this thesis we will only focus in the analysis of the transverse profiles obtained with the FPM. As was expected, they are in good agreement with the results obtained with the emittance scans. The methodology that we will follow in the data examination is to provide the raw profile obtained by averaging the pixels of the ROI in the direction of the beam, obtaining a one dimensional array with the projection of the profile. Then this array is used for graphical representation, curve fitting and statistical analysis. The ROI dimensions, 450 x 50 pixels (equivalent to a beam slice of 144 mm x 16mm), were kept constant to avoid the reflections to interfere with the profile. Due to the high current and low energy of the beam (always extracted with 100 keV) its space charge forces are very high (more information about SC can be found in [84], so the beam tends to be flattened instead of gaussian, as it is shown in Fig. 6.7, where several fittings have been applied. For this reason it is sensible not to give only the information regarding beam width obtained by the gaussian fit of the data. We have decided to include as well the distribution center $\bar{i}$ and the standard deviation of the distribution calculated in a purely statistical way σ_{st} using Eq. 6.1 and 6.2 respectively, where i is the pixel position and f_i is the profile value at position i.

$$\bar{i} = \frac{\sum i \cdot f_i}{\sum f_i} \tag{6.1}$$

$$\sigma_{st} = \sqrt{\frac{\sum f_i \cdot (i - \bar{i})^2}{\sum f_i}} \tag{6.2}$$
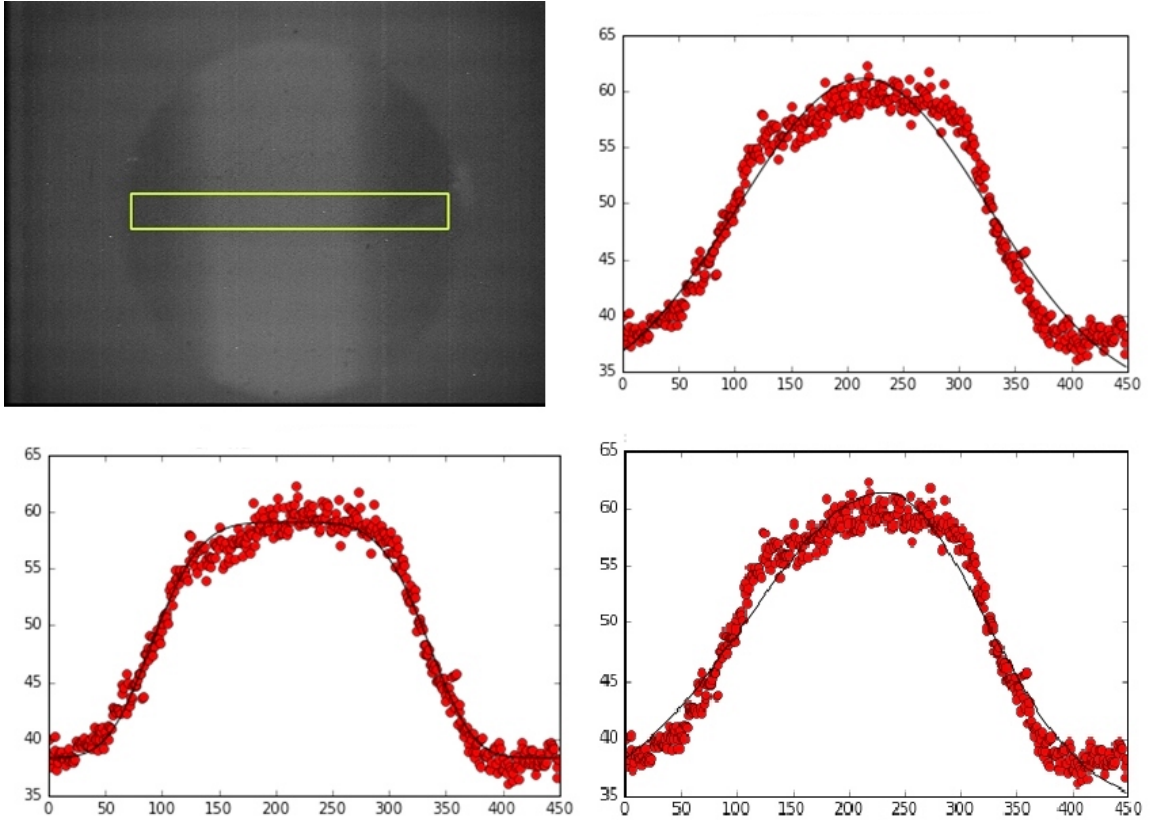
Figure 6.7: Top left: ROI used in the analysis. Top right: Gaussian fitting. Bottom left: Generalized Gaussian fitting. Bottom right: Asymmetric Gaussian fitting.

6.2.1 Residual Gas Composition

In the process of beam fluorescence emission the two main actors are the beam and the residual gas. In our case the beam was a Deuteron beam extracted from a gas bottle and ionized by means of an ECR process. Due to the proximity to the plasma chamber and extraction system the accelerated beam was not pure D^+, but it contained an appreciable amount of D_2^+ and D_3^+, which were easy to spot using both Doppler
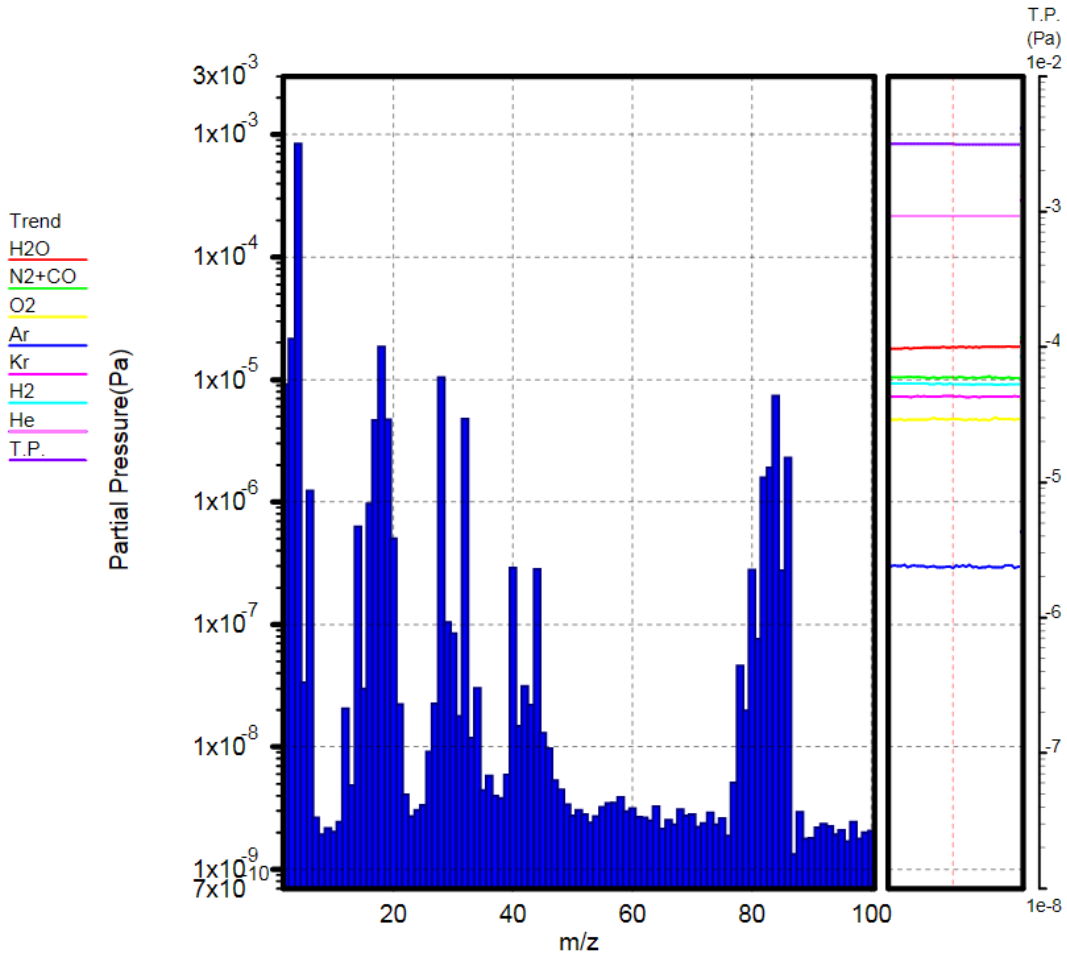
Figure 6.8: Residual gas composition measured with the Residual Gas Analyzer at the diagnostics chamber during beam measurement.

shift spectroscopy and emittance scans, as they have less velocity and focusing than D^+ ions. The specific fraction is measured independently by using the Doppler shift spectroscopy [74] and emittance scans [95]. Both results show quite a good agreement. The residual gas in the diagnostics chamber is mantained at very low pressure by a big turbomolecular pump located in the bottom of the vacuum chamber. The main sources of gas are the injected gas, outgassing, leaks and the beam. In Fig. 6.8 there is a measurement of the gas composition using the Residual Gas Analyzer with only deuterium injected, where we can clearly see the first peaks corresponding to H_2 ($\sim 4 \cdot 10^{-5}$ Pa), HD and D_2 (which apperars as He in the graph), a second peak associated with H_2O ($\sim 10^{-4}$ Pa) from the wall outgassing and Ar ($\sim 2 \cdot 10^{-6}$ Pa) from the residual gas and leaks, another two corresponding with N_2 ($\sim 5 \cdot 10^{-5}$ Pa)
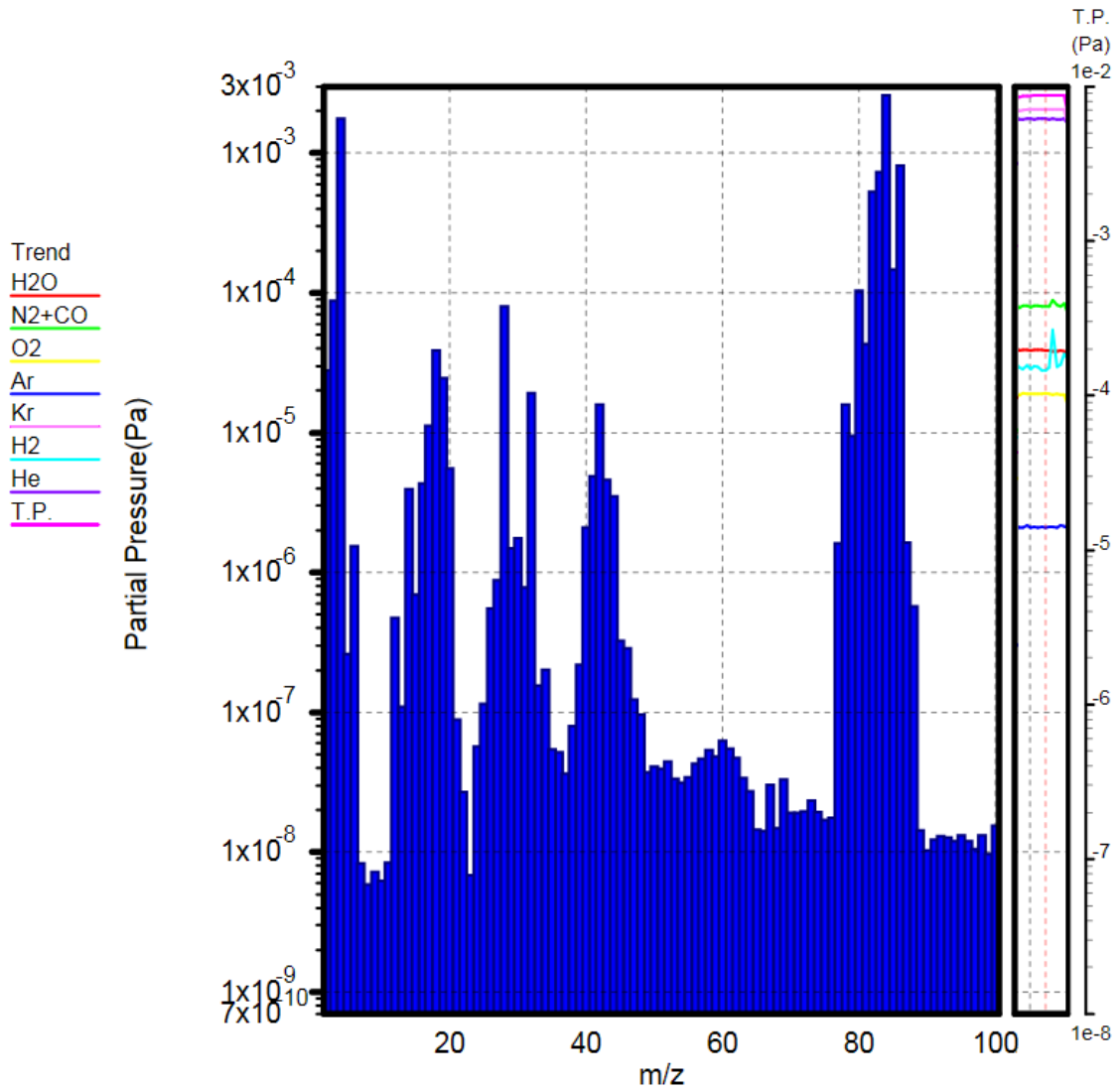
Figure 6.9: Residual gas composition during beam extraction with additional Kr injection.

and $O_2(\sim 2 \cdot 10^{-5}$ Pa$)$, and finally a broad peak corresponding to Kr from previous injection that has not been evacuated yet. With the injection of additional Kr for space charge compensation its corresponding peak grows several orders of magnitude (Fig. 6.9).

6.2.2   Profile vs V_{IE}

The main objective of CW D$^+$ injector commissioning is to obtain a beam of sufficiently high current ($>$125 mA) with the lowest emmitance and the best match with the RFQ. With the minimal configuration used during this campaign few parameters could be changed, being the voltage in the Intermediate Electrode the most important of them. By varying it we can change the divergence (focus) of the beam and obtain different beam apertures. Our scans were initially limited by a minimum voltage of 20 kV due to sparks between the intermediate electrode and the first ground electrode, but after a few upgrades in the connections we were able to go down to 14 kV. The main results are displayed in Fig. 6.10, 6.11 and 6.12.
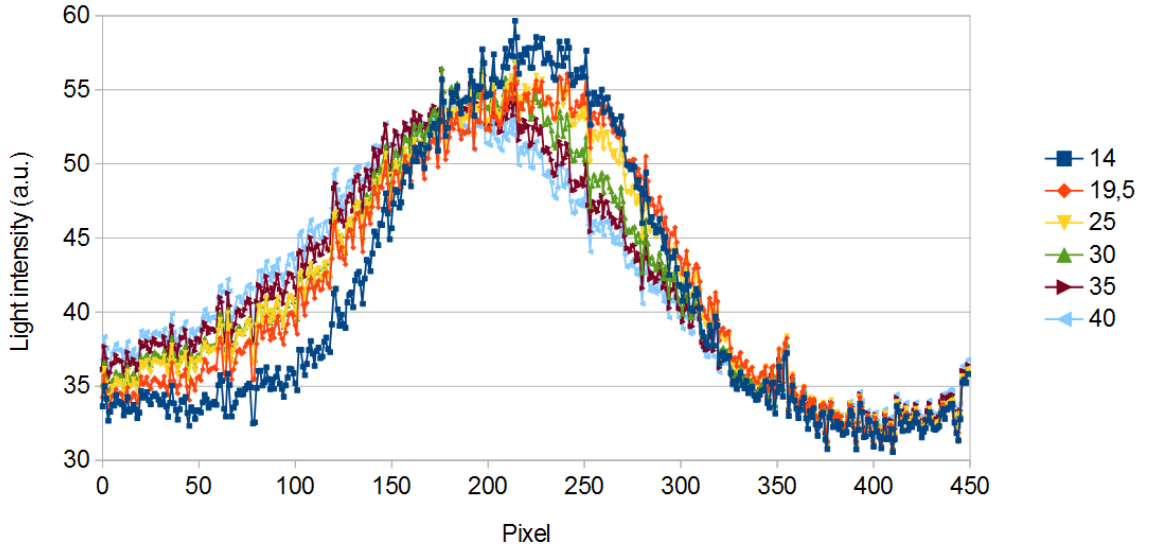
Figure 6.10: Beam profile measured with FPM versus Intermediate Electrode Voltage (kV). $I_b = 115$ mA.

While at different currents the overall shape changes (this will be analyzed later), we can identify a pattern at the three different currents. At higher Intermediate Electrode Voltages the beam width grows, but this growth is not symmetrical. Further examination shows that the center of gravity of the distribution shifts when the voltage is increased to the side where the tail is longer. The exact values of the distribution center position and statistical beam width are summarised in Tabs. 6.3.

This strange behaviour shown by the data (the beam should not be steered), could be explained by a misalignment error, since an offset in the position of a focusing
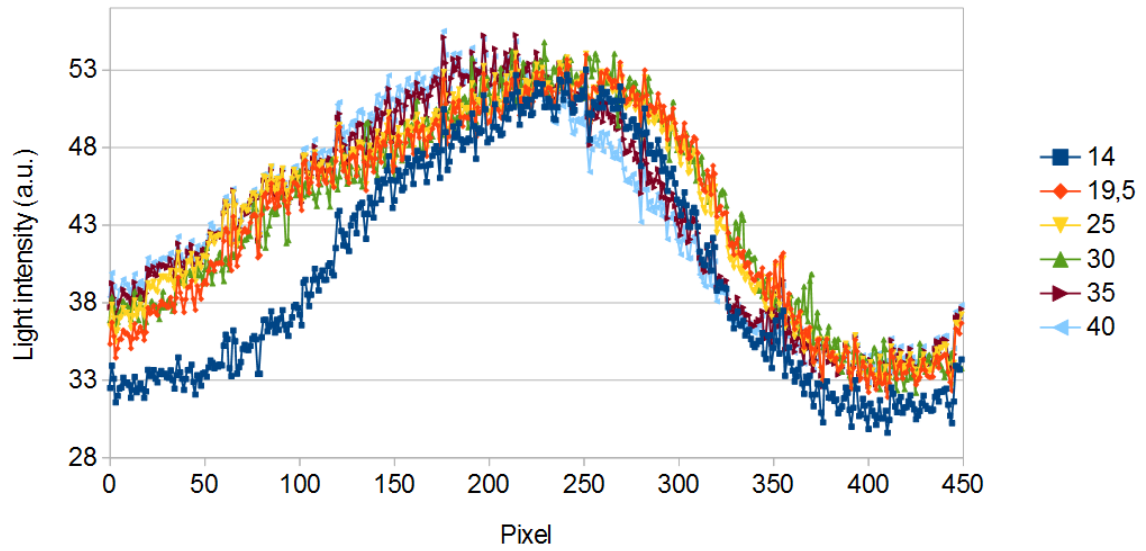
Figure 6.11: Beam profile measured with FPM versus Intermediate Electrode Voltage (kV). $I_b = 135$ mA.
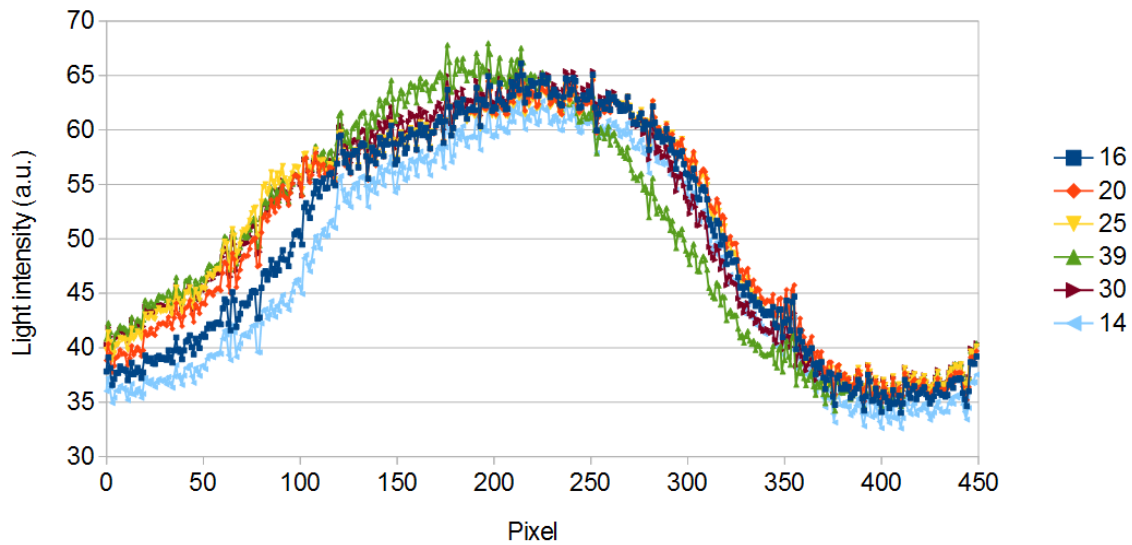
Figure 6.12: Beam profile measured with FPM versus Intermediate Electrode Voltage (kV). $I_b = 156$ mA.

element induces lower order components of the field [13]. In this case the misalignment in an electrostatic lens induces an additional dipolar field that steers the beam with a strength proportional to the voltage applied, hence the decreasing behavior shown in Fig. 6.13, whose linear fitting coefficients are shown in ⟨ ⟩ The dependence of

beam width with respect to the Intermediate Electrode voltaje is shown in Fig. 6.14 After the measurement campaign and thanks to this analysis during maintenance and aligment operations a misalignment in the position of the electrodes was discovered . Another source of error could be attributed the the repelling magnet of the Faraday cup, whose influence in the beam was higher than expected.

V_{IE} (kV)	14	19.5	25	30	35	40
$I_b = 115$ mA						
Center position (mm)	68.8	66.6	64.6	63.0	61.1	59.5
σ_{st} (mm)	25.5	27.4	28.0	28.0	28.5	29.2
$I_b = 135$ mA						
Center position (mm)	68.8	65.6	63.7	65.6	60.8	59.2
σ_{st} (mm)	27.6	30.0	30.34	30.1	29.8	29.8
$I_b = 156$ mA						
Center position (mm)	67.2	66.24	64.6	63.0	62.1	59.5
σ_{st} (mm)	26.9	27.6	28.8	28.8	28.6	28.5

Table 6.3: Beam profile distribution center and standard deviation for different beam currents.
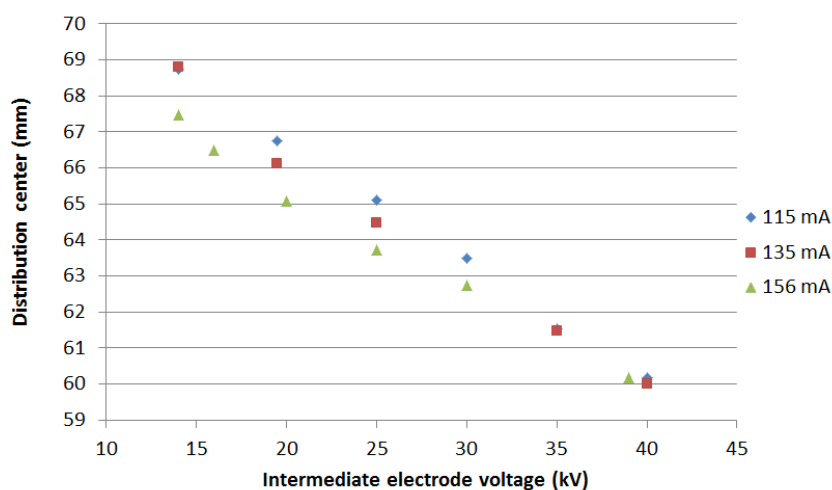
Figure 6.13: Beam distribution center position as a function of the Intermediate Electrode Voltage (kV) for different beam currents.
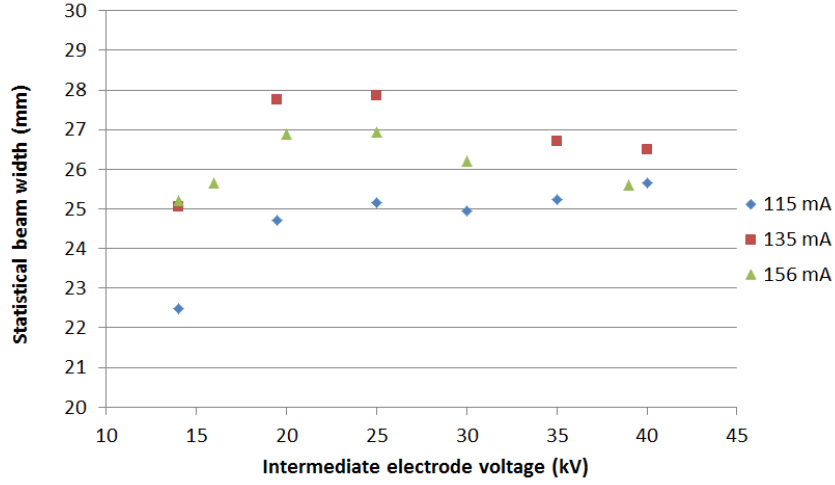
Figure 6.14: Beam distribution statistical beam width as a function of the Interme-
diate Electrode Voltage (kV) for different beam currents.

I_{beam} (mA)	Fitting equation	R^2
115	$-0.331x + 73.3$	0.999
135	$-0.327x + 72.9$	0.990
156	$-0.280x + 71.0$	0.990

Table 6.4: Linear fitting parameters and R^2 for the distribution center as a function
of the Intermediate Electrode Voltage of the data in Figs. 6.10, 6.11 and 6.12.

6.2.3   Profile vs I_{beam}

The next part of the measurements after the intermediate electrode voltage scan is
the profile dependence on the beam current. Due to the plasma source limitations we
were forced to change the current by tuning the RF input power and the gas load, thus
the results obtained in this subsection are not fully comparable, however qualitative
trends can be observed. Although all of the profiles follow the same trends, we will
only display here the corresponding to $V_{IE} = 14$ kV and 30 kV in Fig. 6.15 and 6.16
respectively. Profiles have been normalized with respect to their maximum values
for easier comparison. The source parameter values are summarized in Tab. 6.5. In
order to avoid the saturation of the image intensifier while keeping the noise low the
distance between RF pulses at 156 mA was increased from 100 ms to 400 ms.

V_{IE}	I_{beam} (mA)	RF Power (W)	Gas Flow (sccm)
14	115	300	2.3
14	135	450	2.3
14	156	450	3.3
30	115	255	2.3
30	135	400	2.3
30	156	400	3.3

Table 6.5: Source parameters for the different profiles.

Even though the data is scarce, we can identify two different trends:

- When increasing the gas flow the light level is increased, due to both an increase of pressure and beam current, although we suffer from higher losses and beam scattering.

- The distortion in the shape of the beam. We have seen previously that the strange asymmetric shape could be attributed to the presence of different ion species, however, at the same voltage it was not supposed to broad due to the misalignment of the electrode. This phenomena is explained by the space charge field, which not only counters the focusing effect of the electrodes, but also introduces nonlinearities that distort the profile. We can see that even if the current was increased by 20 mA steps, the distortion seems to be more severe in the first step, where the RF power was increased (Figs. 6.15 and 6.16).

6.2.4   Profile vs V_{REP}

The repeller electrode does not play an important role neither regarding the focusing nor the acceleration of the beam, as it is shielded by two ground electrodes. However, it creates a potential barrier that reflects electrons and prevent them to be accelerated towards the source, de-stabilizing the plasma and damaging the ceramic window of the RF waveguide. During the campaign a brief period of beam time was allocated to study its effects on the beam profile by scanning the voltage over a 2 kV range,
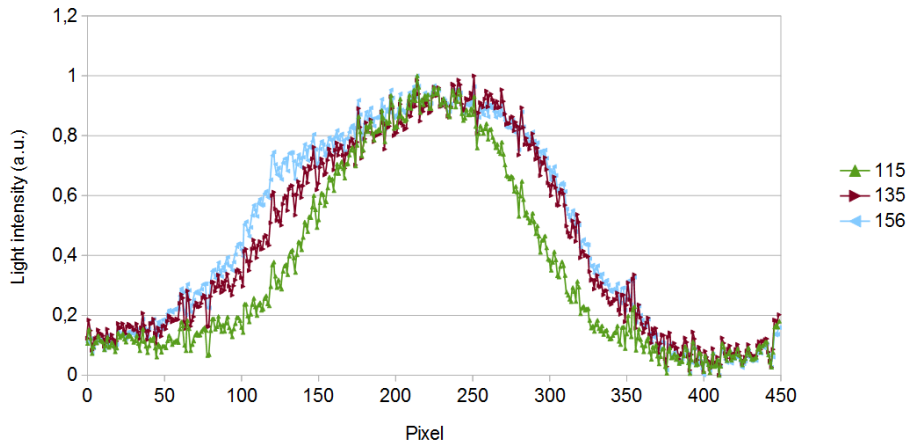
Figure 6.15: Beam profile at different extraction currents (in mA) for a fixed Intermediate Electrode voltage of 14 kV.
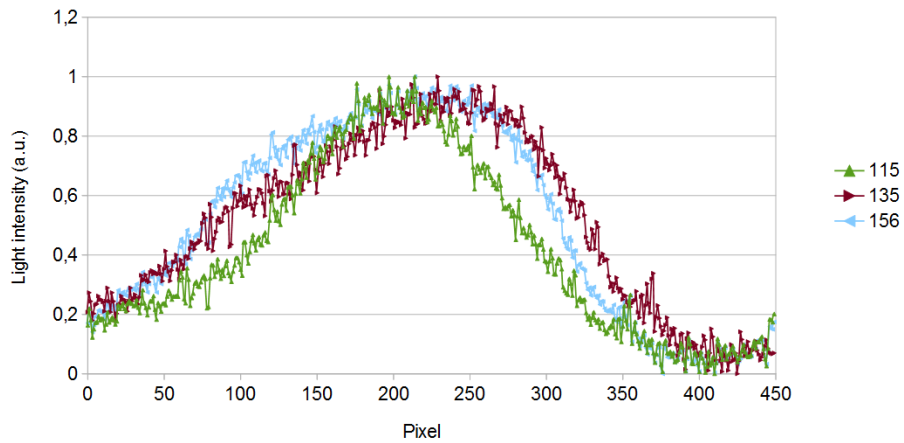
Figure 6.16: Beam profile at different extraction currents (in mA) for a fixed Intermediate Electrode voltage of 30 kV.

yielding interesting (and expected) results. The measurements were done using a 156 mA Deuterium beam.

In Figs. 6.17 and 6.18 we can observe the beam profile with 14 kV and 19.5 kV in the Intermediate Electrode respectively. The effect on the profile is almost negligible in the case of 14 kV, and with 19.5 kV we can see a reduction in the profile intensity at 3.9 and 5.0 kV. If we continue to lowering the reppeller voltage we are able to notice a threshold effect that heavily distorts the profile in Fig. 6.19 (all profiles normalized with respect to their maximum). Below threshold the apparition
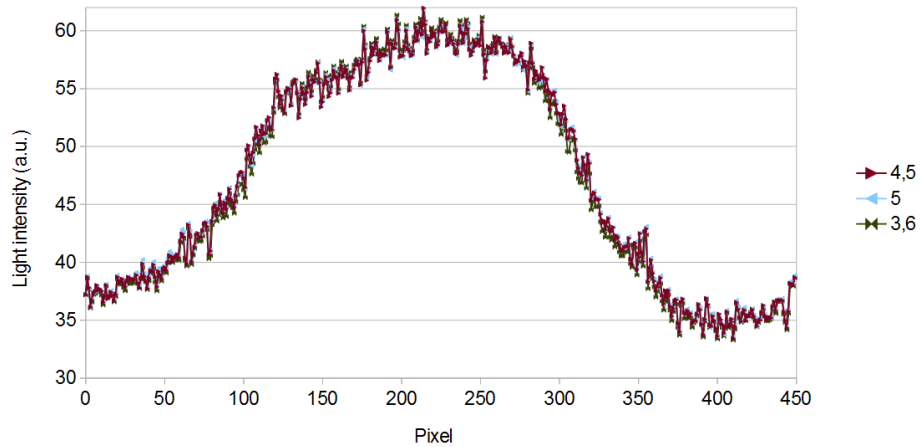
Figure 6.17: Beam profile at different Reppeller Electrode voltages for a fixed Intermediate Electrode voltage of 14 kV $I_b = 156$ mA.
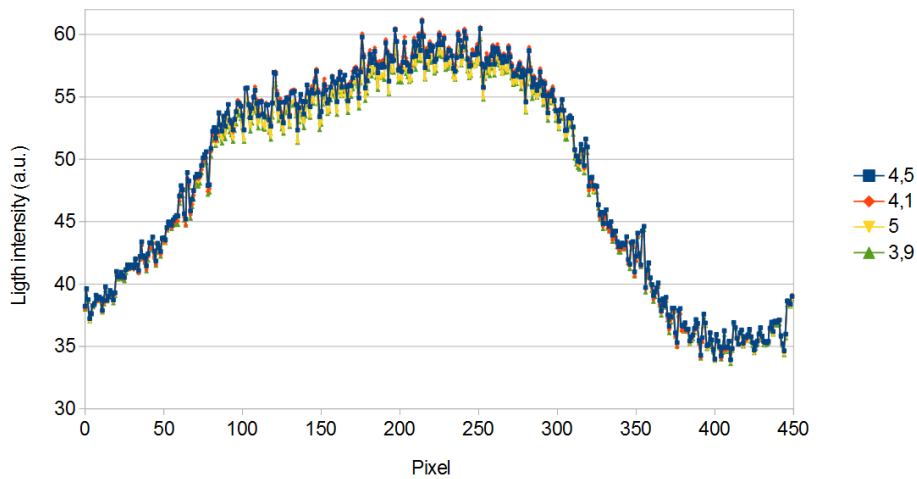
Figure 6.18: Beam profile at different Reppeller Electrode voltages for a fixed Intermediate Electrode voltage of 19.5 kV. $I_b = 156$ mA.

of sparks was also greatly increased.

6.2.5 Profile vs Krypton injection

The last measurements done by the FPM were focused on examining the impact of the Krypton injection in the beam line. Although the external gas injection coupled with non-interceptive diagnostics has been widely used to enhance the signal, in this
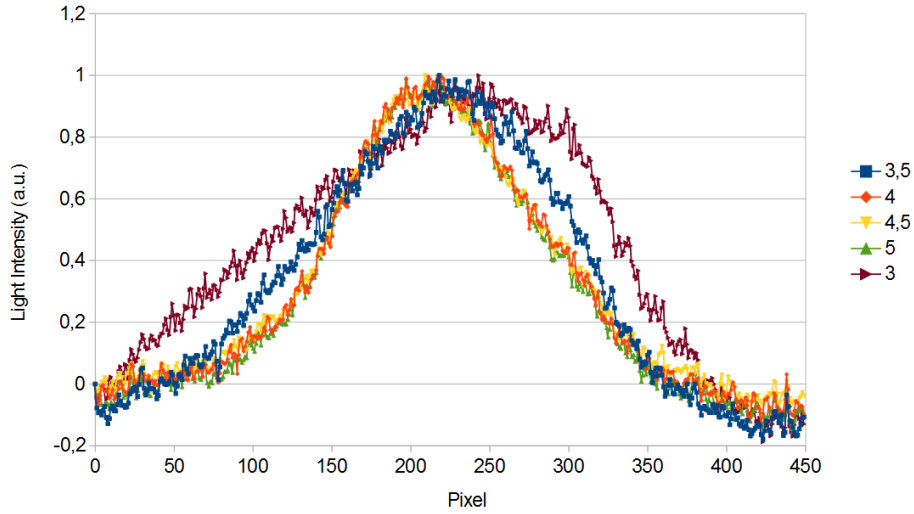
Figure 6.19: Threshold effect in the distortion of the beam profile at different V_{rep} (kV). $I_b = 80$ mA and $V_{IE} = 30$ kV.

case the purpose of injection is to increase the space charge compensation of the beam, minimizing the emittance growth. This is achieved by injecting gas in the chamber with a sufficient flow to reduce the space charge compensation time but low enough to avoid beam losses by charge exchange and emittance growth due to beam scattering.
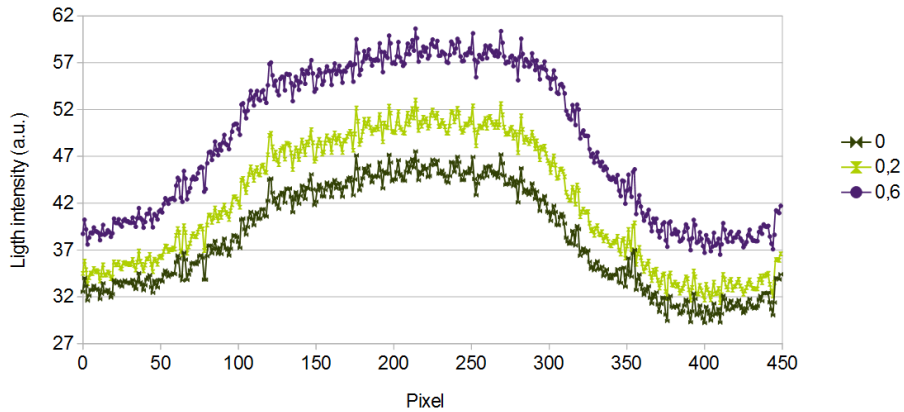
Figure 6.20: Beam profile for different gas flows (sccm) and a fixed Intermediate Electrode voltage of 14 kV. $I_b = 156$ mA.

In these measurements we kept the beam current constant at 156 mA by increasing the RF power at higher gas flows. Results of the profile for different Krypton flows at different Intermediate Electrode voltages are shown in Figs. 6.20, 6.21 and

85
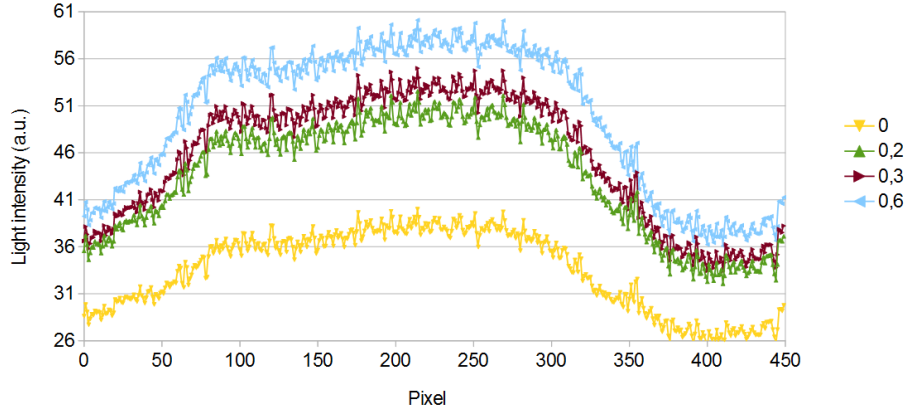
Figure 6.21: Beam profile for different gas flows (sccm) and a fixed Intermediate Electrode voltage of 19.5 kV. $I_b = 156$ mA.
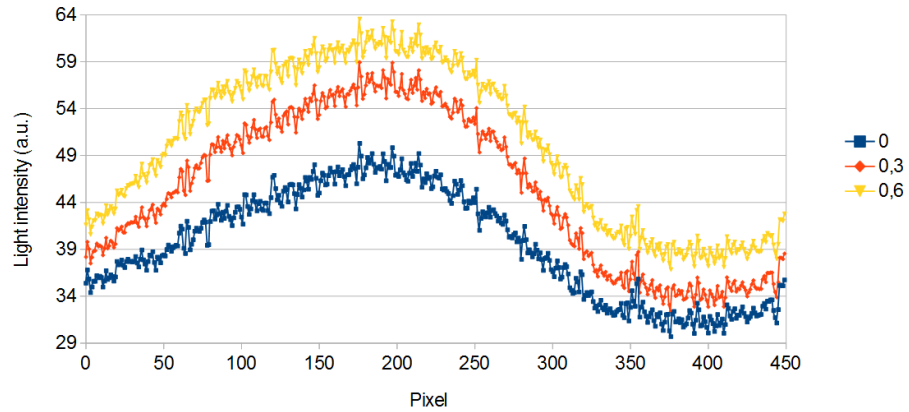
Figure 6.22: Beam profile for different gas flows (sccm) and a fixed Intermediate Electrode voltage of 40 kV. $I_b = 156$ mA.

6.22. Additionally to these measurements, an improvement in the extracted current was observed between 0.15 and 0.3 sccm, becoming the pulse current much more stable and with less ripple, but unfortunately this effect is lost at higher flows. Back to the figures, we do not observe any kind of distortion in the profiles due to the increase in gas flow, only an increase both in the background and the signal, as expected from increasing the residual gas pressure. These observations are in accordance with the theory, as at higher gas pressures we have more density of atoms/molecules ready to be excited. No effect of the gas injection has been found on the profile center and width during the scans.

6.2.6   Profile vs RF Period

The impact of the duty cycle of the pulsed RF was another aspect that was measured during the campaign. The signal is proportional to the integration time and the RF period. In Fig. 6.23 we can see the raw profiles for RF pulse period of 60 ms (5% DC) an 100 ms (3% DC) obtained with 156 mA and a RF ON time of 3 ms. We were limited in power by the status of the beam dump at the time of the measurements. The statistical analysis yielded a center of the distribution located at the same pixel position for both of the profiles, but the standard deviation for the 100 ms is 8.4% higher (31.4 vs 29.0 mm) than the one obtained in the case of 60ms.
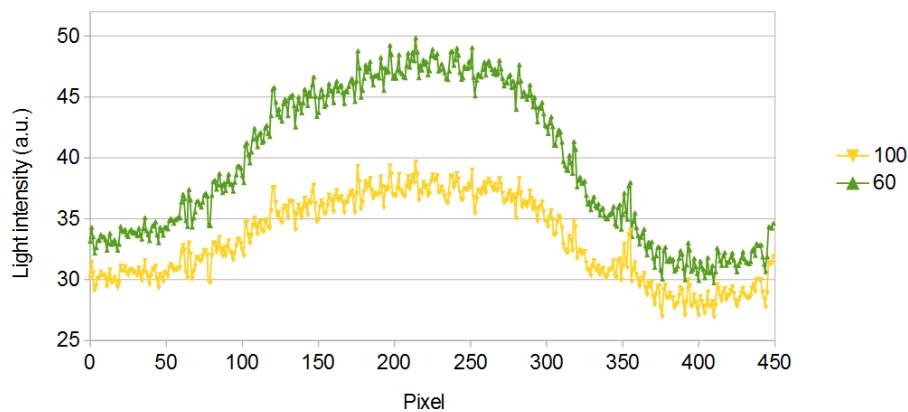
Figure 6.23: Variation of the profile for different RF period (ms). Beam extraction time was kept at 3 ms.

The increase of the beam width is typical in systems when the SNR is small, either because of the low signal strength or high noise, and require special treatment of the data in the post-processing to retrieve the signal correctly. In our case the signal is not very low, it is even possible to detect it with a much less sensitive CCD camera, but due to the high sensitivity of the device and the electronic noise the contribution of the background is quite high.

6.2.7   FPM vs. Allison Emittance Scanner

In order to verify the correct operation of the FPM we decided to compare the profiles taken with the ICID detector with the ones obtained in the emittance scans using an

Allison scanner [95]. Both systems where installed in the diagnostics chamber located just after the accelerating column, looking at the vertical profile in the same position (they where installed perpendicular to each other). In Fig. 6.24 we have plotted the profiles measured with the emittance scanner and with the ICID for different beam extraction conditions.

The ICID profiles were taken just after the emittance scans, and the results obtained where very similar at lower currents (115 and 135 mA), which correspond to beams with lower space charge and a more gaussian profile. However, at high current (156 mA) and lower voltages in the Intermediate Electrode, the profiles have similar width but the shape is quite different, but in all the cases the profile obtained with the ICID is broader. The asymetric tail is present in both of the systems, as well as a small plateau with some inclination, although the profiles obtained with the emittance scanner (at low V_{IE} and high I_{beam}) exhibit a sharper edge and a spike in the opposite side of the long tail.

We have speculated about the different causes of the spike, and the narrowing of the emittance scanner slit due to a transcient thermal effect is a good candidate, because the spike only appears when the beam edge is very sharp. After the spike we assume that the device reaches the stationary state and the slit width is more or less the same, limiting the current with respect to the case where no heat load was applied. However, emittance measurements take quite a long time, so the stationary state should have been reached in short time and transcient effects should be negligible. The sharper features observed in the emittance scans could also be explained by the absence of the smoothing typical of intensified image devices, where the electrons diverge in the space between the MCP and the fluorescence screen, plus the effect of the averages typically done in the image acquisition and processing phase.

Another cause of error could be the difference in the photon emission cross section (and charge exchange) of the different molecules that are present in the beam and the residual gas excitation by other particles. At higher energies this effect is not present because the beam has been cleaned of undesired particles, but in low energy beam transport lines, specially when we are very close to the plasma or there are dipoles, the presence of heavier ions in the plasma is noticeable, like D_2^+ and D_3^+ in LIPAc. Both cases happen in this particular ion source configuration. It has been foreseen, if another opportunity arises, to further investigate this effect using an imaging spectrograph of an optical filter wheel. From the phase space scans
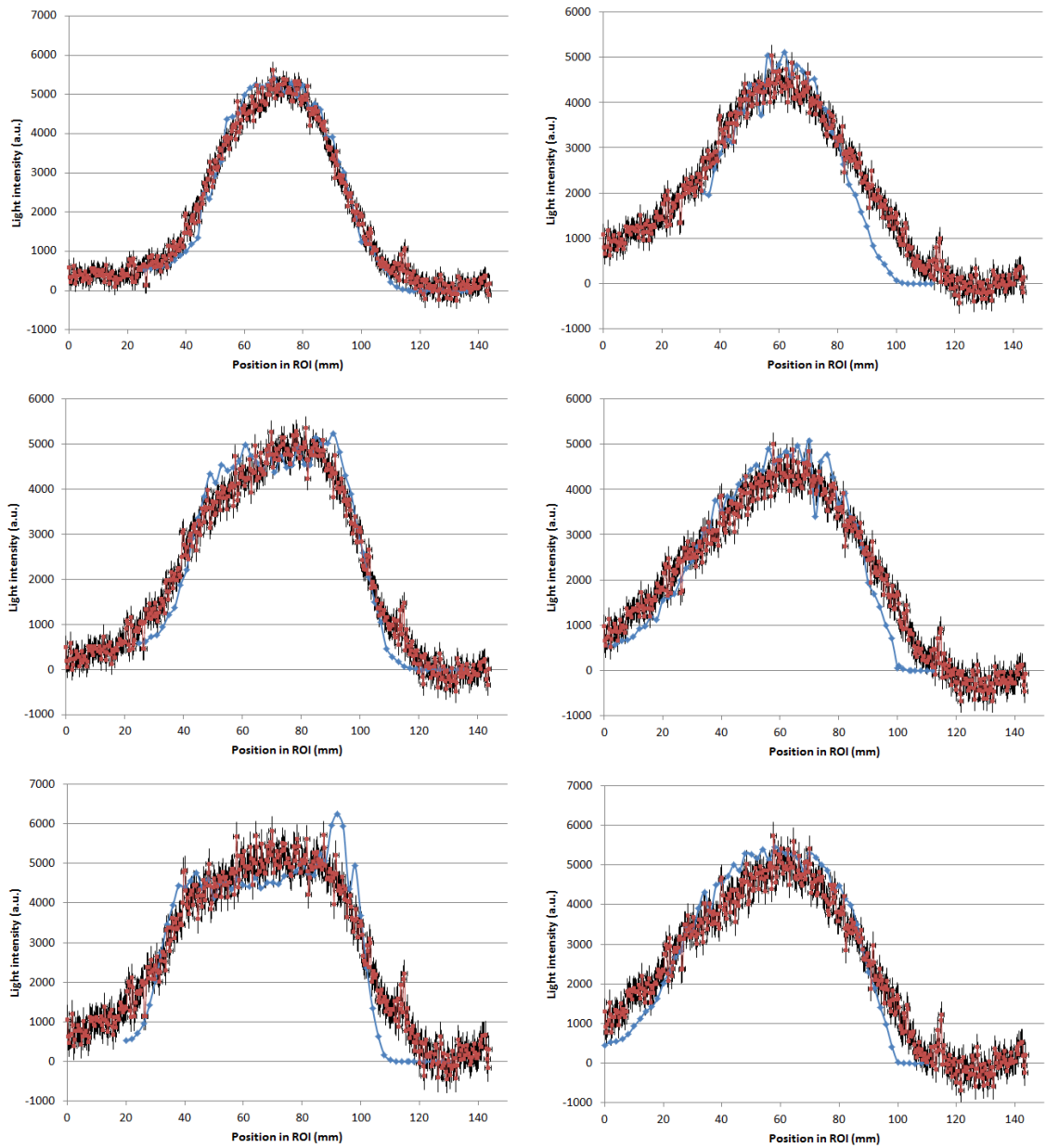
Figure 6.24: Comparison of the profiles obtained with the ICID camera (red) and the emittance monitor (blue). Left profiles are taken at 14 kV of V_{IE}, whilst the right profiles are at 40 kV. Beam current for the top pair is 115 mA, 135 mA for the middle pair and 156 mA for the bottom pair.

performed with the emittance scanner it was not possible to distinguish between the separated ions, as it is seen in Fig. 6.25, because all of the ions beams were defocused with similar angles, as opposite with typical measurements [95] done in between the

solenoids, where the contributions of the different ion beams are clearly seen. Data of the cross sections at 100 keV is not available, however, scaled values from [104] could be used. It is also important to note that the same effect also happen with the electrons created by ionization and later accelerated and trapped by the beam potential, as the calculations done in [83], this effect can reach up to 6 per cent of the alpha line in the case of 95 keV protons. Without knowing the exact potential well of the beam it is difficult to calculate the exact electron distribution in both position and velocities.
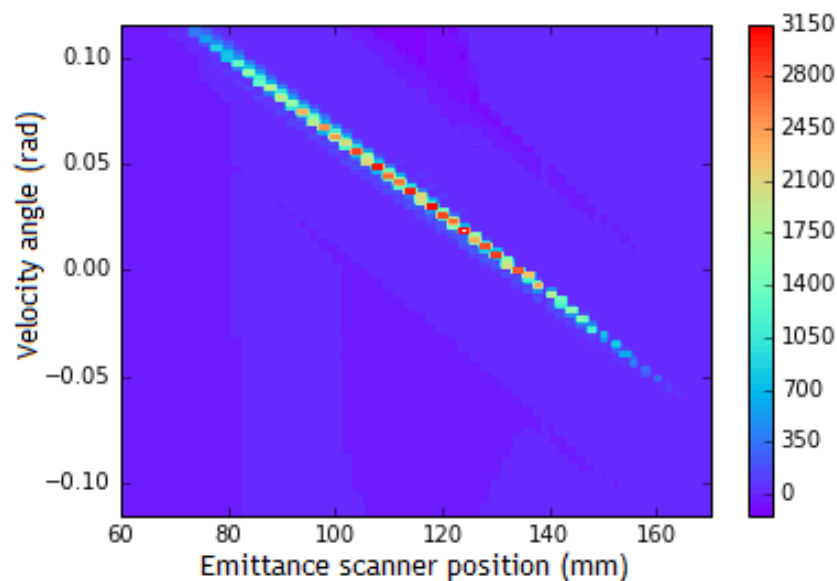
Figure 6.25: Raw emittance profile scan.

6.2.8 Spectroscopic measurements

The other aspect of the fluorescence emission process that was examined during the experimental campaign was the spectrum composition of the emitted light and its variation with the injector parameters. The spectral composition of the emitted light is fundamental when choosing the detector, as the measured signal is going to be stronger when it is matched with the part of highest quantum efficiency of the detector spectral response. In our particular case the bialkali photocathode, as shown previously in Fig. 6.4, is higher in the UV band and the blue light. With

MCP and PMT the quantum efficiency is mainly determined by the photocathode response. The emitted light corresponding to the fluorescence process in the injector comes mainly from the excitation of Deuterium atoms and molecules. In theory all of the gases contribute to the emission process, but for practical purposes only the most relevant give a signal strong enough to be detected over the background noise. This effect limits our observation to the first two lines of the Balmer series of the Deuterium, D_α (at 656.94 nm) and D_β (at 486.68 nm), when no additional gas is injected. We are also able to see its associated Doppler Shifted components. When Krypton gas is injected its spectrum lines appear clearly.
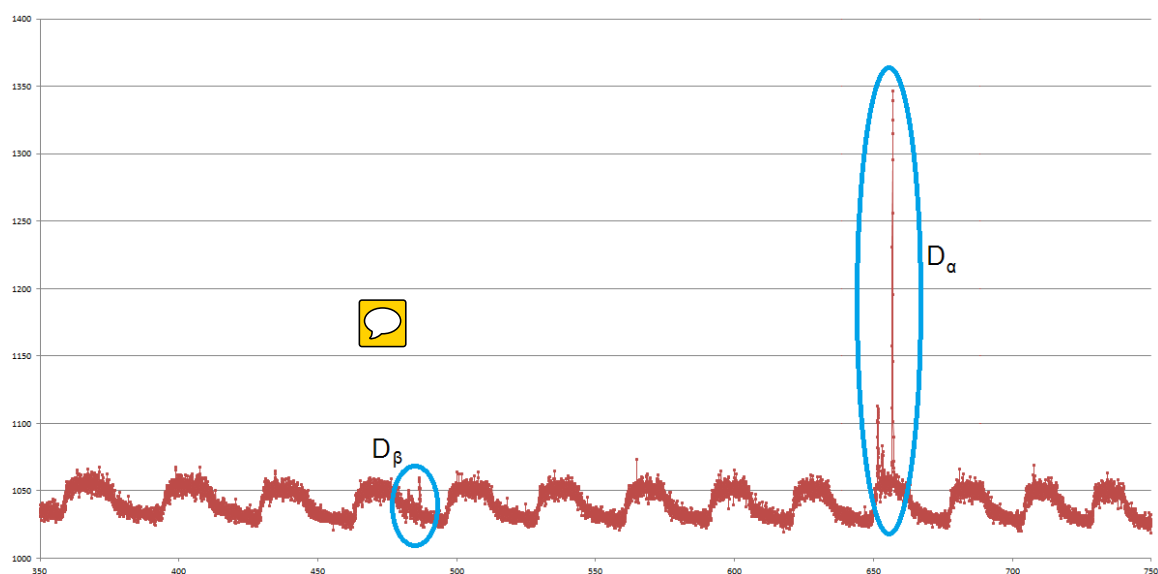
Figure 6.26: Spectrum measurement of the light emitted by the extracted beam without Krypton injected.

Our combination of spectrometer and detector provided us a resolution of 0.03204 nm, with 1024 channels, therefore the longest spectre that we could measure was 32.8 nm. This was long enough to cover each line of the Balmer series with their associated Doppler shifted lines, but in order to take measurements of the whole spectrum the diffraction grating needed to move several times, taking a few minutes to do a measurement. This had an effect on the stability of the measurement, causing an oscillation of the noise floor, as it is shown in Fig. 6.26. However, this oscillation is very long, in the order of the maximum spectrum lenght, so with a proper removal of the floor level we can compare the measurements without problem (as was done). Even without removing, the D_α and D_β and their associated Doppler shifted components are seen over the background without problem.

91

For calibration purposes we have compared the theoretical wavelength of the D_α and D_β and compared with the measured values, finding an offset of 1 nm in the spectrometer with respect to the values predicted by the theory. The results are shown in Tab. 6.6.

Line	λ_{theo} (nm)	λ_{meas} (nm)	$\Delta\lambda$ (nm)
D_α	655.94	656.94	1.0
D_β	485.88	486.68	0.8

Table 6.6: Theoretical and measured values of the center for the first two lines of the Balmer series.

6.2.8.1 Balmer Series

The measurements with the spectrometer were done with constant gas flow and then the different source parameters were varied. We focused in six lines in total: the basic D_α and D_β, which come from the residual gas excitation, the D_α and D_β coming from the neutralization of D^+ at 100 keV and its posterior photon emission, and the $D_{2\alpha}$ and $D_{2\beta}$, coming from the neutralization of the D_2^+ extracted at 100 keV. Although the Doppler lines of D_3^+ were observed in the case of the α line, the signal was so weak with respect to the noise floor that the results gave no clear information.

During the first measurements we kept the current at 156 mA and then we proceed to change the Intermediate Electrode voltage, and then the Repeller Electrode voltage. In the case of the IE voltage a weak dependence of the line intensity with respect to the intermediate electrode voltage was observed in the case of all the lines, which is shown in Fig. 6.27. In the case of the Repeller Electrode voltage, in Fig. 6.28 no significant change in the case of D_α was observed, and for D_β the measurement was very noisy, so no conclusive results were extracted. The full data of the recorded spectrums can be found in Appendix 1 (Fig. A.1 and A.2).

In the second measurements we proceed to do an scan in the beam current by varying the RF power. During the scan the gas flow of D_2 was kept at 2.75 sccm, the Intermediate Electrode voltage held at 30 kV and the Repeller Electrode voltage at 4.5 kV. Eq. 4.11 predicts a linear dependence of the line intensity with the beam current. In Fig. 6.29 the dependence of the D_α shows a linear increase
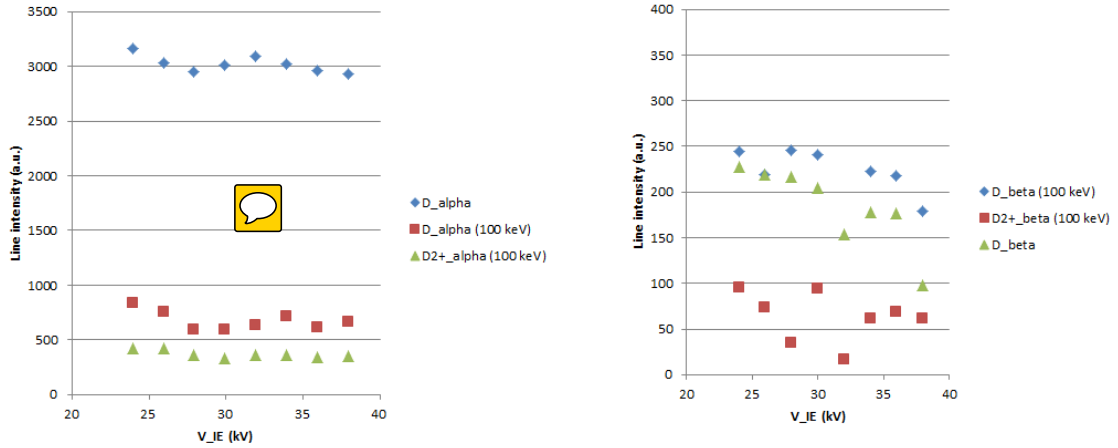
Figure 6.27: Line intensity variation of the D_α (left) and D_β (right) with the Intermediate Electrode voltage.

in the case of the deuterium coming from the residual gas excitation and the charge exchange. However, the intensity of the line coming from the neutralized D_2^+ seems to decrease at high current, but we believe it could be associated with an error in the measurement. In any case further investigation is needed.

A similar trend can be observed for the D_β in Fig. 6.30, but in this case the contribution from neutralized D_2^+ is stable. The absence of growth of that particular line indicates that at higher power not only the beam current is higher, but also the proportion of D^+ in the extracted beam is higher, a desirable characteristic to minimize the radiation and heat load due to the dumping of undesired extracted ions. The full spectrum graphs are also found in Appendix 1 (Fig. A.3 and A.4).

6.2.8.2   Balmer Series with Krypton injection

During normal operation of LIPAc's injector it is foreseen the use of additional Krypton to reduce the emittance of the extracted beam by increasing the space charge compensation. In order to evaluate the impact on the proportion species and the plasma operation spectral measurements for different Krypton flows were taken. Results for D_α and D_β are shown in Fig. 6.31 and 6.32 respectively. To compensate the neutralization due to the increase the gas pressure the RF power is increased as well to keep the beam current constant. In the case of D_α lines the increase is linear, however it is remarkable to see that while in the case with no Kr injection (Fig. 6.29)

93
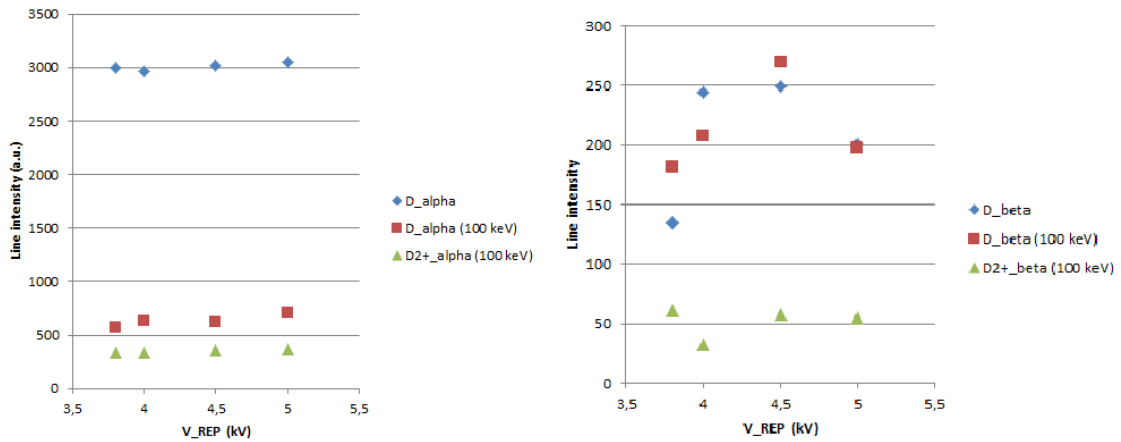
Figure 6.28: Line intensity variation of the D_α (left) and D_β (right) with the Repeller Electrode voltage.
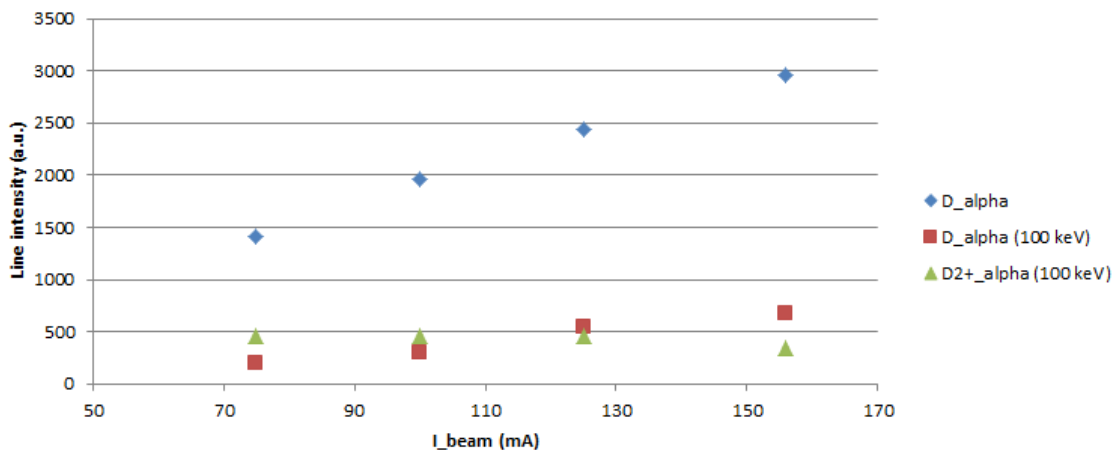
Figure 6.29: Line intensity variation with the beam current (mA) for the D_α and its Doppler shifted components.

the slope of the linear fit would be higher for the light coming from the residual gas, in this case the situation is the opposite and the line intensity for the light coming from charge exchange has higher slope. The effect is very likely to be caused by the increase in the neutralization due to the higher pressure. In the case of the D_β lines the general trend is to increase the line intensity at higher flows, however the data shows a quite erratic behaviour due to the noisy measurement, as can be seen in the
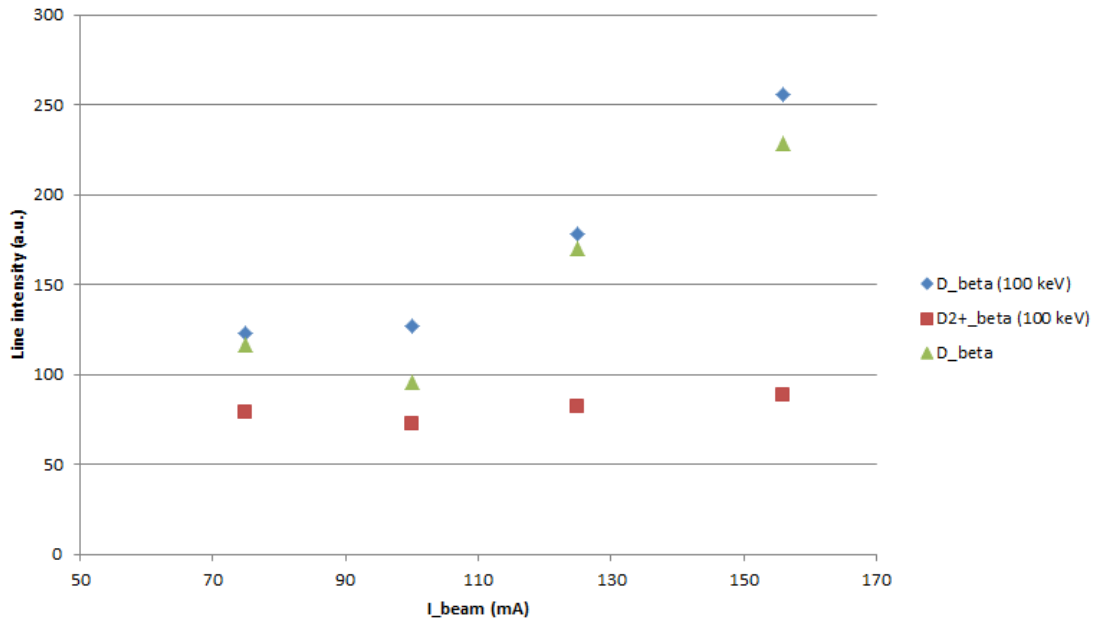
Figure 6.30: Line intensity variation with the beam current (mA) for the D_β and its Doppler shifted components.

spectrums of Appendix 1 (Fig. A.5 and A.6). Further investigation for these lines would be required to assess the linear behaviour.

6.2.8.3 Krypton spectral lines

The injection of Krypton gas, reaching a partial pressure in the order of the deuterium gas (Fig. 6.9), implies that new spectral lines will be contributing with their light to the fluorescence process. These lines are closely related to the electronic configuration of the related gas atoms and/or molecules. In the case of Krypton multiple lines appear in the visible spectrum, giving the glow lamps of Krypton their characteristic light blue colour, but due to the limitations of our detectors only a few of them are seen. A complete list of spectral lines for atoms in different states of ionization can be found in the NIST database [105]. In Fig. 6.33 it is shown the fluorescence spectrum of the beam with the injection of Krypton. Even though they are many in number, the Krypton lines are relatively weak compared with the Deuterium lines at similar partial pressures: $6 \cdot 10^{-3}$ Pa of Deuterium vs $7 \cdot 10^{-3}$ Pa of Krypton. With the current setup most of the lines are barely above the noise floor. The use of an EMCCD or
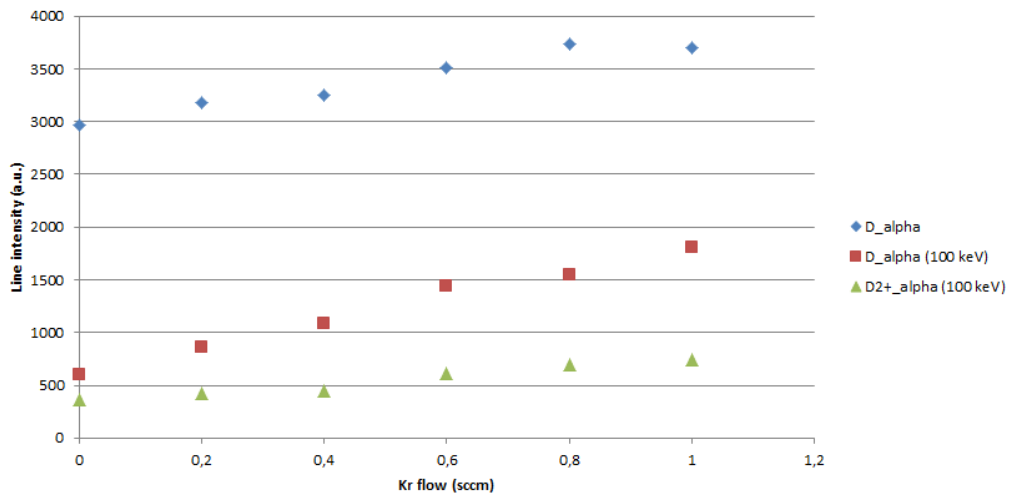
Figure 6.31: Line intensity variation with the Krypton flow (sccm) for the D_α and its Doppler shifted components.
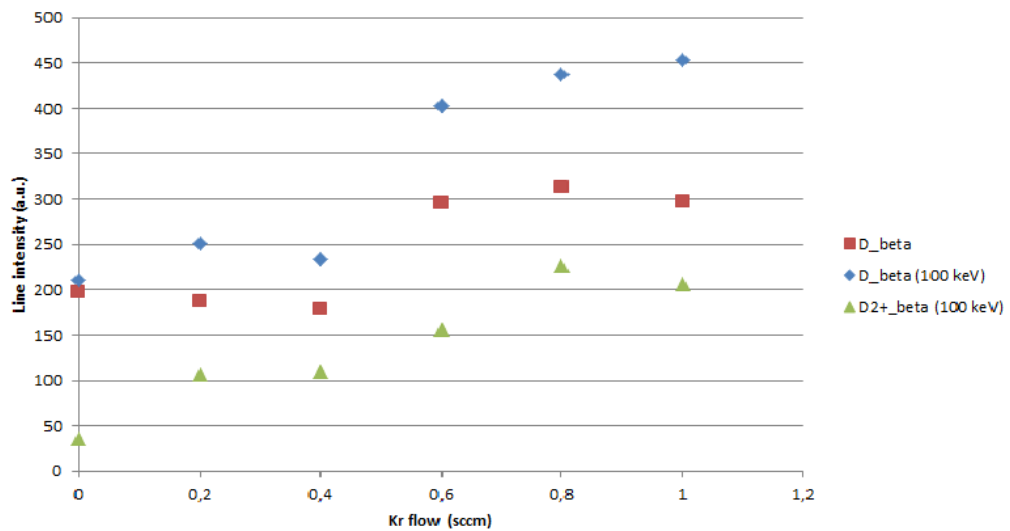
Figure 6.32: Line intensity variation with the Krypton flow (sccm) for the D_β and its Doppler shifted components.

ICCD instead of a cooled CCD camera (or their equivalent in CMOS technology) could probably yield better results when measuring the weak line intensity. For our analysis we have decided to focus in four different Krypton lines to study their linearity
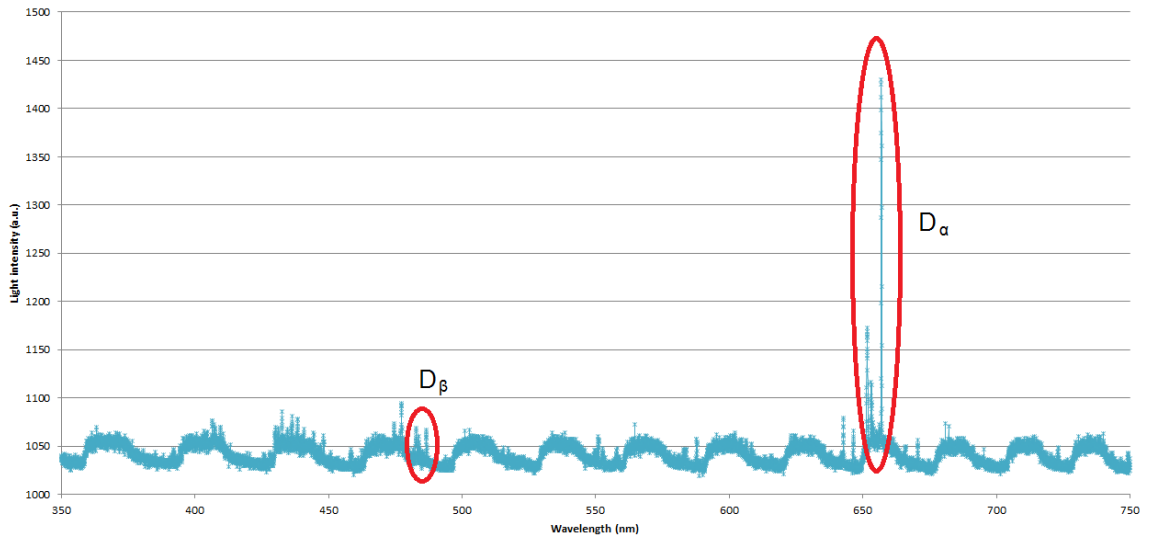
Figure 6.33: Full profile with 156 mA beam and 0.8 sccm of Krypton injected.

with the beam Krypton flow, which are enumerated in Tab. 6.7. The recorded profile are found in Fig. A.7.

Line	λ_{tab} (nm)	λ_{meas} (nm)	$\Delta\lambda$ (nm)
λ_{477}	476.57	477.30	0.73
λ_{642}	642.02	642.81	0.79
λ_{646}	645.63	646.47	0.84
λ_{743}	742.554	743.25	0.[?]

Table 6.7: Selected lines of Kr to evaluate their linearity. Comparison between theoretical and measured wavelength.

The three lines with shorter wavelengths were chosen because there were three of the most intense ones. The last one has significantly smaller value, but is important for other reasons. In Fig. 6.34 we observe the linear growth of the lines with respect the gas flow, a result that was expected. In the case of the 743 nm line the linear dependence at low flow values is not clearly seen due to the low signal.

In all of the cases we see that an offset between the measured wavelength and the theoretical wavelength exists, but in all the cases is very similar. Our main reason is that this line is very close to the 743.578 line, which involves spin flip (Tab. 6.8), therefore it can only be excited by electrons. Of the Kr line at 740.706 line no
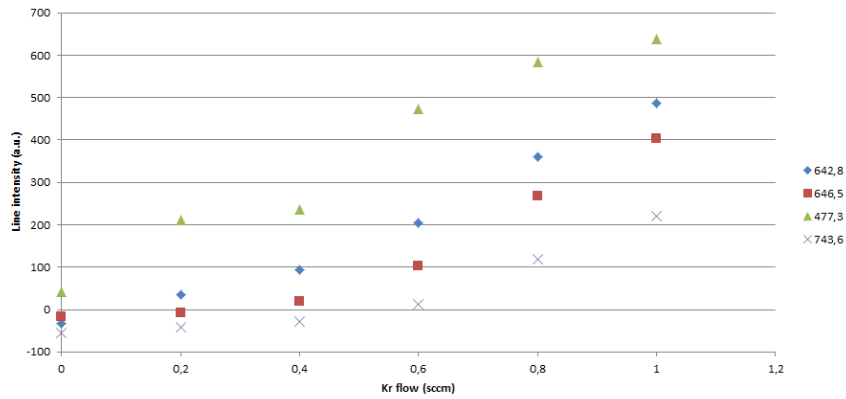
Figure 6.34: Line intensity variation with the Krypton flow (sccm) for the selected Krypton lines (nm).

trace is found, even though is stated to be far stronger than the line we selected. This small region of the spectrum should be studied in detail in further campaigns when the accelerator is available for experimentation and a more sensitive spectrometer is available, since if we are capable of measuring the profile generated by the 743.578 nm line we could have a direct measure of the electron density distribution in the core of the beam, allowing us to compare it to the calculated using the beam dynamics code and give insight about the space charge compensation process.

λ (nm)	Final state	Initial state
743⟨?⟩	$4s^2 4p^4$ (^{3}P) $5p$ ^{4}D^0 $\frac{5}{2}$	$4s^2 4p^4$ (^{1}D) $4d$ ^{2}D $\frac{5}{2}$

Table 6.8: Electronic configuration of the final and initial states of the 743 nm line.

Chapter 7

Radiation hard beam profile diagnostics for DONES

As explained before, DONES is a 40 MeV, 125 mA, CW accelerator [19]. Its main objective is the production of neutrons via deuteron-lithium reactions. Due to the strong beam requirements at the lithium target the beam should be continuously monitored. In order to ensure the correct neutron field required for the irradiation of the samples, the beam profile should be kept during the required limits. Since the TIR is the last room before the lithium target, the last beam diagnostics are planned to be installed there. However, due to the demanding conditions caused by the high radiation levels, wide beam profile and low pressure, the diagnostics at that position should be carefully designed. In this chapter we present the preliminary design stage for the profile diagnostics at the TIR, which will serve as the basis for the rest of the profile diagnostics of the HEBT, where the beam parameters are similar but enviroment conditions are much less demanding.

7.1   HEBT layout

The DONES accelerator High Energy Beam Transport line is still under design, although in its final stages. Its main goal is to transport the beam from the last cryomodule [106] up to the lithium target [107] and shape the beam profile to meet

the requirements needed for obtaining the desired radiation field. A more detailed description of the diagnostics layout along the HEBT is found in [108]. The HEBT is divided in several sections, which is also shown in Fig. 7.1.

- Section 1: The first transport line goes from the end of the fifth cryomodule up to the last dipole. It has several profile, current and position diagnostics to ensure that the beam is transported safely, since with a 5 MW beam even tiny are potentially dangerous to the accelerator.

- Section 2: In the second section are located the higher order magnets which are required to shape the beam to meet the rectangular transverse profile requirements [109]. Since the profile is critical, transverse profile monitors need to be installed near the multipole magnets. The scraper is located between the dodecapoles in order to purify the beam from particles with undesired position and momentum. Due to the high radiation fluxes, those scrapers must be shielded and the diagnostics installed should withstand the radiation dose received between the maintenance periods.

- Section 3: In the last section we find the diagnostics and the transport magnets (quadrupoles plus steerers), which guide the beam up to the lithium target. In the last part of this section, where the RIR and TIR are located, we find the most demanding conditions due to the radiation fluxes, specially at the TIR room.

- Beam Dump Line: From the second dipole (Section 2) a short beam line extends up to a beam dump, which is intended to be used for the commissioning and tuning of the machine.

As mentioned before, the most demanding conditions are found in the TIR room. Due to the high neutron fluxes remote handling of the components is mandatory [110]. The current strategy is to divide the beam line in different modules and replace them with and overhead crane. Additionally, due to the hazardous nature of the liquid lithium that flows in the target, the TIR room as well as the target room are filled with argon. Together, these two facts need the development of special connections for the cables, pipes and fibers, which should meet the three main requirements: air tightness, radiation hardness and remote disconnection. In this room three different modules are planned to be installed: the first diagnostic module, the
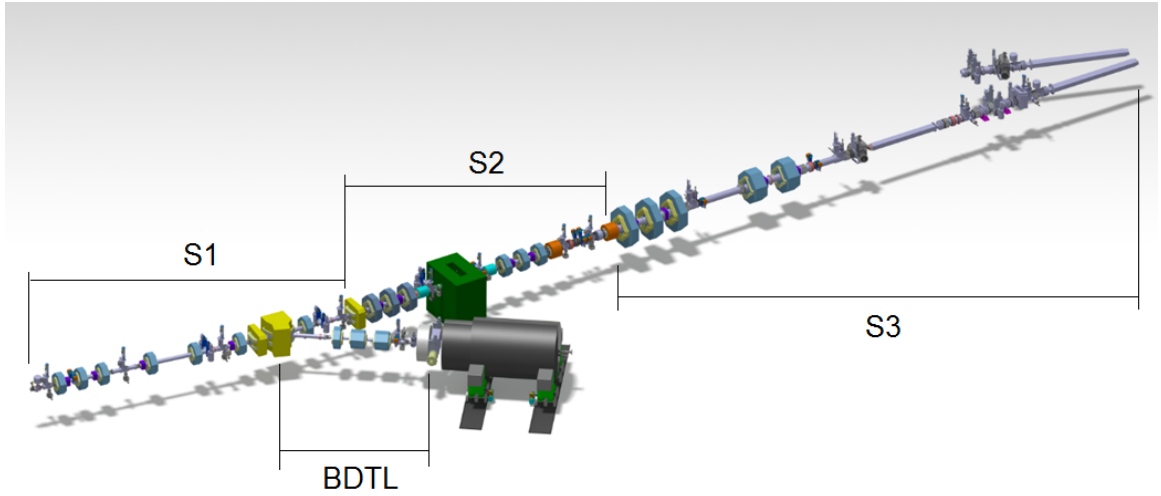
Figure 7.1: Layout of the HEBT with the different sections and the beam dump line. Source: [6].

vacuum pumping module, and the lead shutter module, which also includes diagnostics. The composition (diagnostic wise) of the line at the TIR is described in Tab. 7.1. In Fig. 7.2 a layout of the TIR line is shown.

Beam Position Monitor	3
DCCT	1
ACCT	1
Beam Loss Monitor	2-3
Interceptive Profile Monitor	2
Non-Interceptive Profile Monitor	2

Table 7.1: TIR diagnostic module composition.

7.1.1   Radiation dose and neutron flux

In the DONES facility the neutrons are produced via Li(d,xn) reactions in the Test Cell room, were the beam is stopped in a liquid lithium curtain. The spectrum of the produced neutrons is similar to the one produced in fusion reactors. The backscattered neutrons and gamma rays, although collimated by the wall between
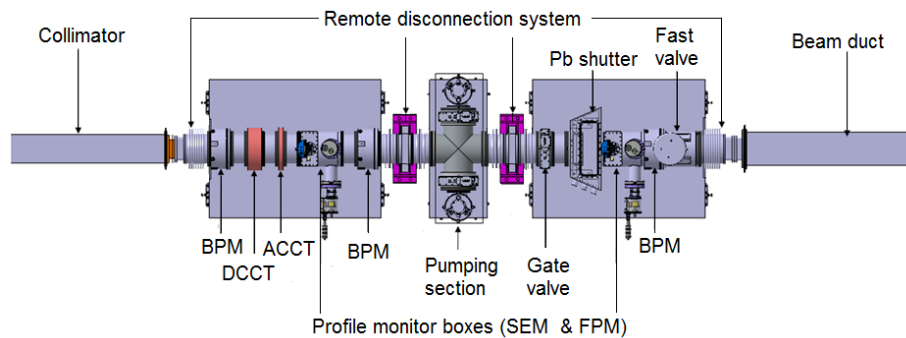
Figure 7.2: Layout of the beam line at the TIR. Source:[6].

the Test Cell and the TIR, could travel freely through the beam pipe, where they collide with the beam pipe and give rise to more radiation. Since the radiation dose calculation is an iterative process which should take into account the modifications done in the building, the beam line and the wall feedthroughs, final calculations are not available yet. However, several simulations have already been performed [7] [111]. The neutron fluxes are in the order of 10^8 neutrons/cm^{2}s, with biological absorbed doses in the order of few Sv/h, and absorbed doses in silicon of few Gy/h, as it is shown in Fig. 7.3. Typically, active electronics components are able to withstand up to few hundredths of Gray. Hence its installation close to the beam pipe is forbidden due to their short expected lifetime. In order to ease the task of selecting the appropiate radiation hard components a database of radiation hard components (and manufacturing companies) has been developed in the frame of the ENS project [112].
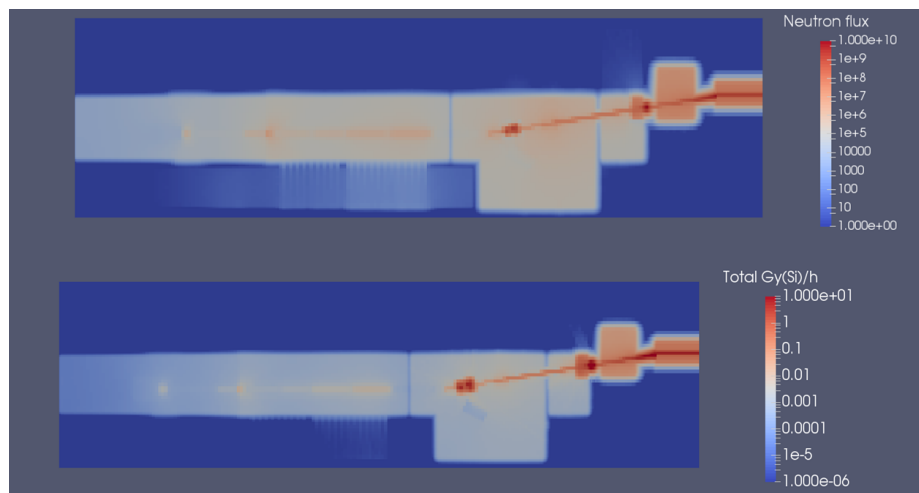
Figure 7.3: Radiation dose distribution in the DONES building during beam [7].

7.2　Beam Dynamics requirements

The main goal of the DONES facility is to study the neutron irradiation damage on material samples for its use in the future fusion reactors. In order to ensure the correct irradiation of the samples, the beam profile and position at the target should be within tights limits and two different profiles must be available [109].The overall beam requirements are listed in Tab. 7.2, and the required profile is shown in Fig. 7.4. The flat profile with the pair of peaks has been found to be the optimum compromised between high irradiation volume of neutrons and what is possible to generate with the higher order magnets [113].

Beam Energy (MeV)	40
Beam Current (mA)	125
Energy Spread FWHM (MeV)	0.5
Beam Profile size (cm^2)	20x5 | 10x5 (optional)
Angle incidence (º)	9
Beam Position (mm)	$\pm$ 0.25
Beam uniformity	$\pm$ 5% (across flat top)
Beam tails	$< 0.5 \ \mu A/cm^2$ beyond $\pm$ 11 cm (horizontal)
Horizontal edge peaks	15% - 30% over average density
Maximum Extension (cm)	25 x 10

Table 7.2: Required beam parameters at the lithium target.

7.3　Profile Monitors

One of the critical parameters of the DONES accelerator is the shape of the deuteron beam at the target position. As it has been shown before, it has a rectangular shape with two peaks at the side. Since the beam coming out of the SRF linac has a gaussian shape, higher order magnets (octupoles and dodecapoles) together with moveable scrapers are needed to obtain the required profile. The rectangular profile starts forming at the multipole magnet position, in the section 2 of the HEBT, and it
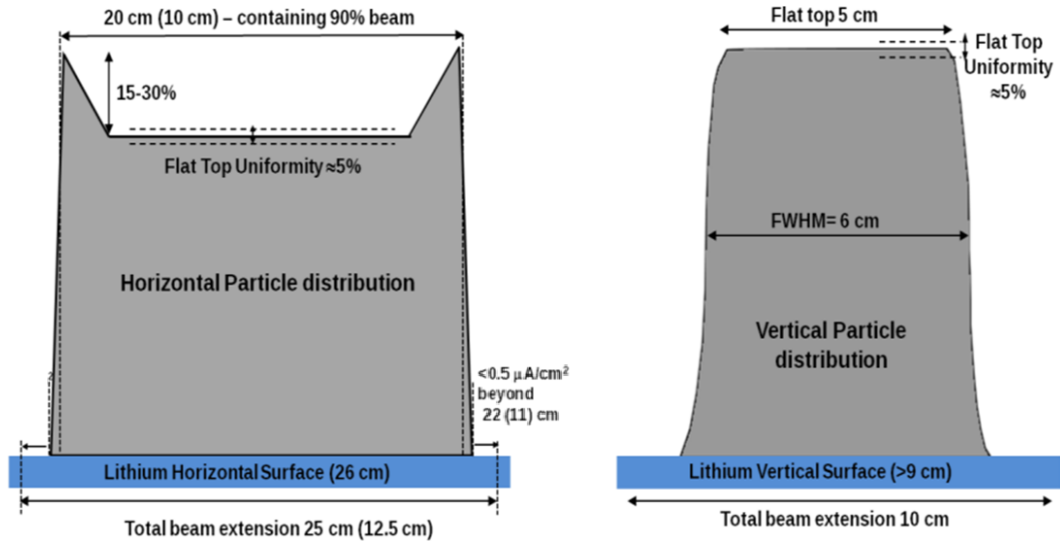
Figure 7.4: Beam profile requirements at target position [8]

is not fully developed until a few meters before the target. Up to date no clear profile diagnostic for the beam at the target position has been found, but several candidates are being studied. On the other hand, profile monitors are planned to be installed along the accelerator, specially at critical points such as the exit of the SRF linac, the region between multipole magnets and the TIR. Simulations of the beam profile at the start and end of the TIR are presented in Fig. 7.5.
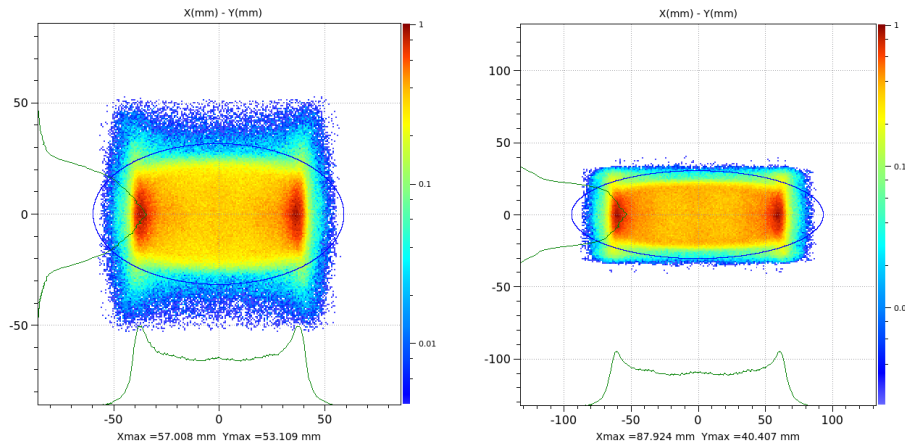
Figure 7.5: Beam profile simulations at the start (left) and end (right) of the TIR room [8].

Two different kinds of profile diagnostics are planned to be installed, inter-

ceptive diagnostics for low current and/or duty cycle operation, and non-interceptive diagnostics for nominal current and CW operation. Since at normal operation the beam power is very high, non-interceptive diagnostics are a necessity. In the case of interceptive diagnostics two options were considered, fluorescent screens and wires, but in the end the later were selected due to the high beam power. In the case of non-interceptive diagnostics, due to the high current Fluorescence Profile Monitor have been considered a priori, as they are less sensitive to space charge distortion, but Ionization Profile Monitor has not been discarded because in some areas the installation of redundant diagnostics is been considered, and the latest developments on correction schemes for space charge distortions seem promising [114]. The TIR, for example, is a good candidate for the installation of an IPM, since it is the last position were a profile monitor is installed and the beam size has grown appreciably from previous positions. However, one point of major concern with IPM is the impact that the evaporated lithium of the target will have when deposited in the insulation between measurement channels and, more important, the insulation between high voltage electrodes. The other point of major concern is the influence of the flow of neutrons coming directly from the target without any prior moderation.

7.3.1   SEM grid

At lower currents and/or duty cycles, such as the working conditions used for beam commissioning and machine tuning, the non-interceptive diagnostics are not able to get enough signal to give a good profile, thus interceptive diagnostics are needed. Additionally, at high power densities the interceptive diagnostics are destroyed due to the intense heat deposition, therefore interceptive and non-interceptive diagnostics complement each other in the operation of the machine.

Interceptive profile monitors for hadron beams have used traditionally two kinds of devices: fluorescent screens and wires [26]. Screens are composed of ceramics compounds, and are not able to withstand high thermal loads. Wires tipically use high melting point materials, such as tungsten, silicon carbide or pure carbon. Whilst screens rely on recording the emitted light by the screen, which is proportional to the beam profile, the wires use secondary electron emission produced by the passage of the beam charged particles through the surface of the material. For DONES we propose the use of a grid using tungsten wires, since preliminary simulations have

found that fluorescence screens are not able to withstand the thermal load. Due to the requirements of the superconducting RF cavities the use of carbon is forbidden in the accelerator [115], thus tungsten and some particular alloys such as rhenium-tungsten are the only available materials with high melting point. Since we want to reduce the number of elements inside the beam pipe due to the high radiation levels we are proposing to use a grid of wires instead of a moving wire.

The complete theory of secondary electron emission can be found in [28], but for our purposes some assumptions can be done in order to calculate the emitted current per wire. As a first approximation we have used 48 wires per profile, thus with 96 wires in total (vertical and horizontal profiles) we only need three 32-channel modules (a typical module) for the current measurements. The spacing of the wires is 2 mm in the center position and 3 mm at the sides, although this distribution is not totally fixed and will be validated with final beam dynamics. The preliminary calculations have been done using a 125 mA, CW beam, with a bi-dimensional gaussian distribution with and rms value of 20 mm in both the horizontal and vertical direction to simulate a lateral peak of the beam (the most dangerous part since the thermal conduction is quite low). The signal is proportional to the beam current in order to extrapolate at different currents. The results are found in Fig. 7.6, were the measured profile as been plotted for different wire diameters: 20, 50, 100 and 200 μm. In all of the cases the values are easily measurable using standard electronics.

One of the most important points when working with SEM grids is defining the safety values of operation of the machine. As a first approach, a calculation has been done with a 125 mA, 40 MeV CW deuteron beam going through a 100 μm diameter wire. Considering tungsten as the wire material, an energy deposition of 2.48 eV/A is obtained with SRIM [116]. Only radiative losses have been considered at the peak position, therefore using the Stefan-Boltzmann law a peak temperature (in the center of the gaussian beam) in the order of 5000 ºC is obtained, which is way above the tungsten melting point of 3695 K, thus the need to calculate the limits to operate in pulsed mode.

We have made several assumptions for our calculations in order to operate the diagnostics safely:

- The energy deposition along the diameter of the wire is considered constant since the path length is much larger than the diameter. Calculations of the
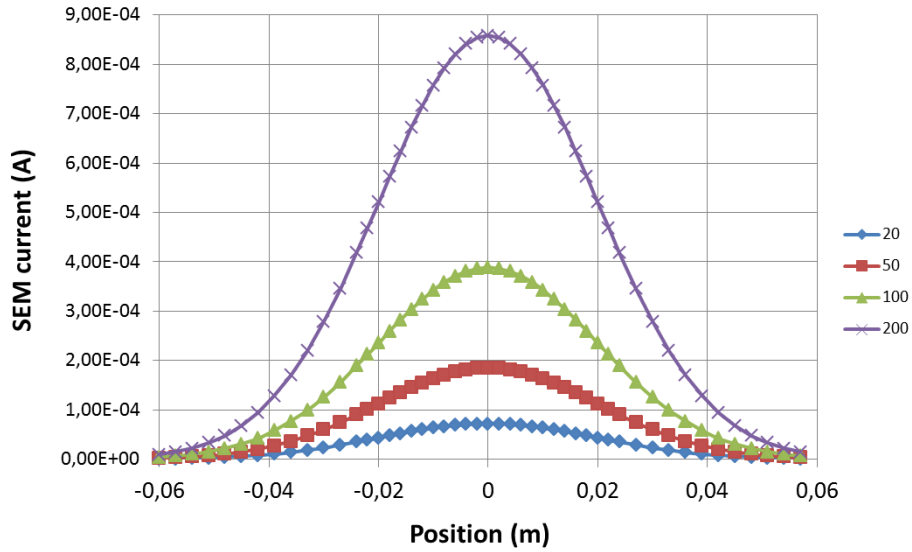
Figure 7.6: Simulation of the acquired profile by the SEM grid for different wire diameters (in μm).

energy lost per unit length were done using SRIM.

- The beam considered is 40 MeV, 125 mA deuterons at a repetition rate of 1 Hz. Its power deposition similar to the 20 MeV protons that are also going to be used during comissioning, but with a maximum beam current of 62.5 [💬]. For the peak current we have considered a beam with a Gaussian shape with a rms value of 20 mm in both horizontal and vertical directions. Although this is not the nominal beam, at the time of the simulations a final profile of the beam was not available from beam dynamics since the accelerator layout was not fixed, therefore we focused on examining one of the side peaks of the horizontal profile. For the final decision on the wires a complete simulation will be done at all of the SEM grid positions.

- The model considered is a 0-dimensional model, where the power deposition corresponds to the peak of the beam profile. This overestimates the temperature, giving us a safety margin, but is good approximation since the wire diameter is small considered to its length and the heating ratio is very high. The maximum temperature is achieved after a few pulses, therefore in operation the pulse length should be increased slowly to avoid thermal shocks.

- The limit for safety operation has been set using the tungsten melting point (3695 K) plus a safety margin of a few hundred degrees. We have not consid-

107

ered the changes of the crystalline structure or breakdowns that the material undergoes at high temperatures and alter its mechanical properties [117]. If this is the case lower duty cycles should be used, and switching from pure tungsten wires to tungsten-rhenium wires could be considered, which have better resistance against recrystallization at the expense of lower melting point.

The thermal and electrical results of the calculations are resumed below in Tab. 7.3, were the maximum allowable duty cycle (due to meltdown) for each wire diameter is shown. We can see that the thinner wires allow higher duty cycles, but, as seen in 7.6, the SEM current is smaller.

ϕ_{wire} (μm)	Max. DC (@1Hz) | | T_{ON} (ms)	Peak Temp. (K) @ Max DC
20	0.6 % | 6	3490
50	0.6 % | 6	3648
100	0.5 % | 5	3550
200	0.4 % | 4	3594

Table 7.3: Thermal and electrical calculation results for different tungsten wire diameters

The thermionic current density is given by Eq. 7.1, where T is the temperature and ϕ_W the work function, will distort our profile measurements. The thermionic current density (in A/m^{2}K^2) as a function of the temperature for tungsten ($\phi_W = 4.5$ eV) is plotted in Fig. 7.7.

$$j_{th} = 1.2 \cdot 10^6 T^2 e^{-\frac{\phi_W}{k_B T}} \tag{7.1}$$

In our analysis using a time dependent 0-dimensional model, which will be later expanded to a 1-dimensional time dependent model, we found that the heating of the wire is linear up to the region were radiation cooling becomes important, which is in the order of 3500 K for the case of the 20 μm wire. The linear region gets larger for higher diameters, as it is seen in Fig. 7.8. We will consider the maximum allowable thermionic current a 10% of the total SEM current. By using this criteria, and starting from ambient temperature, we have calculated the maximum beam pulse for the different wires, which are written in Tab. 7.4. It can be seen that
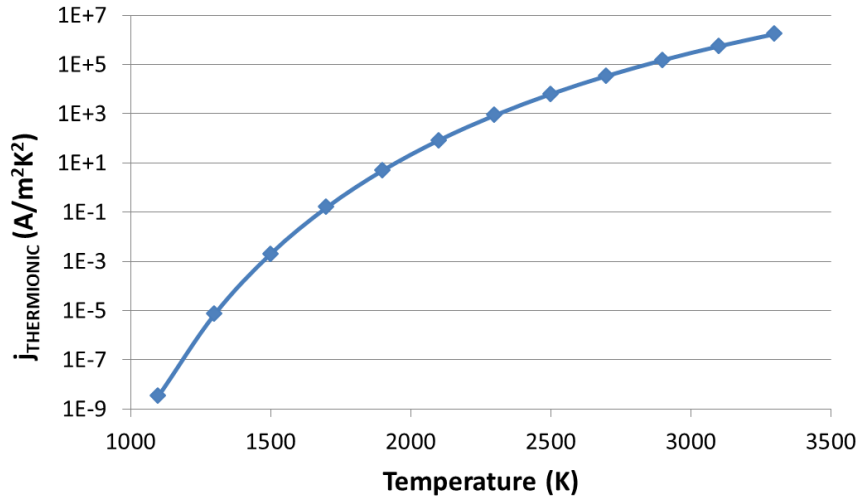
Figure 7.7: Thermionic current (according to Eq. 7.1) for Tungsten.

the limiting factor is the thermionic current and not the melting point. Although we are considering the worst case, with no heat transfer and the central wire, below the maximum beam on time our wires are safe and the profile distortion is less than 10%. From the simulations can be seen that the maximum pulse length is similar in all of the cases, and so is the current, but in order to have a compromise between electric signal and transported heat along the wire, the ones with a diameter of 50 and 100 μm are a good option, therefore the final decision will depend on the simulations for the other SEM grids of the HEBT in order to choose the same wire to simplify maintenance, if those simulations give similar results.
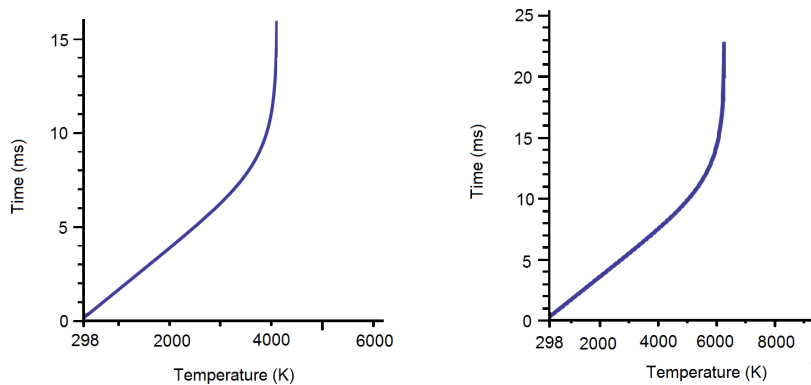
Figure 7.8: Maximum temperature evolution of the $\phi = 20$ μm wire (left) and the $\phi = 200$ μm wire right.

109

ϕ_W (μm)	SEM current (A)	Max. Time (ms)	T_{max} (K)
20	$7.19 \cdot 10^{-5}$	3.707	1935
50	$1.85 \cdot 10^{-4}$	3.637	1952
100	$3.89 \cdot 10^{-4}$	3.474	1954
200	$8.59 \cdot 10^{-4}$	3.158	1959

Table 7.4: Maximum allowable beam on time for $I_{th} = 10\%$ I_{SEM} and maximum temperature reached for tungsten wires and 40 MeV, 125 mA Deuterons.

7.3.2 Fluorescence Profile Monitors

7.3.2.1 LIPAc design review

During the installation and commissioning phase of LIPAc some valuable information regarding its performance, and also some key issues have been identified, which have led to propose a redesign to adequate the profile monitor to the special needs required for the TIR area. Some of these concerns are only a problem for high radiation areas, like the TIR or the profile monitors located close to the scrapers, but other are common to all of the FPM. The main issues of the present FPM are summarized in the following list:

- Mechanical coupling to the line: The present design is coupled to the viewport. This configuration applies stress directly to the flange, which leads to an uneven torque on the copper sealing gasket and can produce unexpected vacuum leaks when manipulated.

- Rad-hard wires and connectors: The high radiation environment together with the remote handling will impose heavy constraints on the materials and connectors. Special maintenance procedures must be also developed [110], [112] and [118].

- Rad-hard lens: Image forming elements suffer from radiation damage from neutrons and gamma rays, leading to darkening and reduction of the transmittance, thus a material which withstands a large radiation dose, such as fused silica, should be used [40].

- Modifying lens parameters: Current design only allows to change the lens parameters such as the aperture or the focal length hands on, thus making it unsuitable for high radiation areas, where remote handling is expected. A change in the mechanical design should be made in order to adapt the diagnostic to the remote handling.

- Inner carriage movement: Movement of the sensor in the image plane is done with a micrometric actuator. Experience with the LIPAc prototype has suggested that such fine adjustment is not necessary, as the data is later processed and fitted to a function, where those misalignments can be taken into account and both the Field Of View and Depth Of Field are wide enough to accomodate the beam. This actuator also adds additional weight quite far from the center of gravity, greatly contributing to the applied stress to the viewport. A redesign should be done in order to improve the movement system.

- Active voltage regulator: Current image sensor, a PMT array (model H7260 from Hamamatsu), uses and active divider for the last stages of the high voltage bias network [72]. Due to the radiation levels the transistors of the voltage divider are not expected to last long, requiring an special PMT assembly with an external bias based on a rad-hard bias network, or a system based on radiation hard optical fibers to guide the light to a safer location.

7.3.2.2   Design upgrades

Given the feedback received so far from the LIPAc FPM, we propose a design upgrade for the monitor located at the TIR room in DONES, which could also be used for the monitors located close to the scrapers, since the radiation flux is quite high in those areas. The design is inspired by the systems used for acquiring images in hazardous or difficult access areas, which use light guiding fibers to take the image out of the area where the sensor is located. The upgraded system would be divided in three parts: 1) the head, 2) the guiding fibers and 3) the sensor (Fig. 7.9).

The head of the FPM is attached to the beam pipe, taking care in isolating the system from stray light coming from outside. At that position the beam pipe has an inner diameter of 250 mm, whilst the beam has an rms size of 20 mm in both horizontal and vertical axes. A diagnostics box design has been proposed [119], were
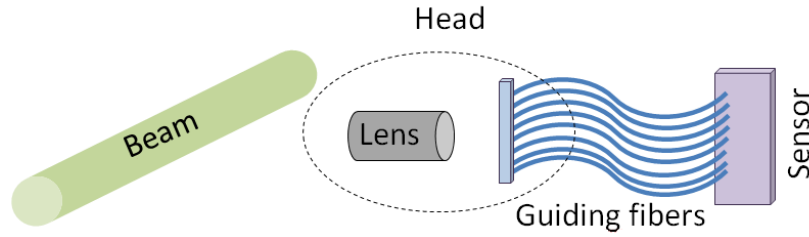
Figure 7.9: Schematic of the FPM at the TIR room.

two viewports are installed in order to measure the vertical and horizontal profile, and one port were the SEM grid is installed. In order to avoid huge transmittance losses from radiation damage early on, fused silica viewports have been chosen due to their radiation hardness [40] [120]. The image is formed using a rad-hard lens on one side of an array of light guiding optical fibers.

For the optical calculations, at the interface point (image plane) we have considered a FOV in the sensor of 7σ (140 mm) and a working distance of 500 mm, far enough from the beam center to reduce the gamma and neutron flux, which produces an image in the fiber plane of 21.84 mm for a 78 mm focal length. As we are interested in collect as much light as possible, large core multimode radiation hard fibers are selected. The first proposal is to divide the image area in 31 rectangular channels, but is yet to be confirmed that this number of channels provides enough resolution to extract the details of the beam, since at that position the final double peak transverse profile has not been developed yet. With 31 channels the image is divided in 31 rectangles of 0.704 mm width. To increase the light level each channel is composed of 9 fibers which will combine later at the sensor. Due to the round shape of the fiber we have chosen to pack the fibers forming a hexagon grid, with every channel separated from its neighbors with a thin foil. A 3D mock up is shown in Fig. 7.10

Alternatively, the size of the sensor area could be decreased with the same amount of fibers by using a shorter focal length and thinner image fibers. With a 25 mm focal length we obtain an image size of 7 mm long, each channel 0.22 mm wide if we keep the same amount of them (31). In order to use the same amount of fibers its size should decrease accordingly. In Fig. 7.11 we find a comparison between the FPM
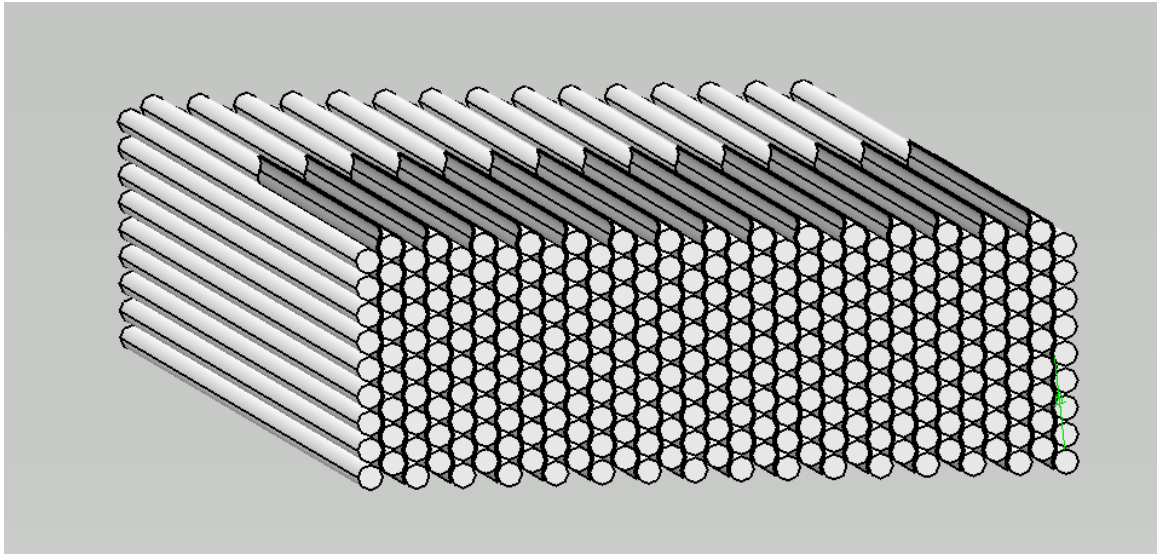
Figure 7.10: 31 x 9 fiber array and foil spacers.

(body cover removed) of LIPAc and the proposed new design. In the case of the 78 mm focal lens a similar form factor is achieved, but we have a much more compact assembly if the 25 mm focal lens is used. The capability for moving the device is currently under discussion, since it will be very difficult to tune the diagnostic due to the difficult access.

In order to avoid damage in the sensor, optical fiber is planned to be used, to keep it away from the radiation areas. Two options were considered: 1) an array of large core multimode fibers, with the fiber size depending on the focal length, and 2) an image fiber, however, due to the large beam size, the image fiber option is less favourable, as the price increases significantly and not much is gained in terms of resolution. Due to the radiation levels rad-hard mumltimode fibers made of fused silica have been chosen. Those fibers have a high amount of OH groups in the material, since it has been proven thath the OH quantity and and impurities concentration plays a key role in the radiation hardness of the material [121] [122].

For both lenses we have selected fibers with a numerical aperture of 0.2. In the case of the 78 mm focal lens a fiber with an inner diameter of 0.60 mm, clad diameter of 0.66 mm and outer jacket diameter of 0.75 mm has been selected. In the case of the 25 mm focal lens, the selected fibers have an inner diameter of 0.20 mm, clad diameter of 0.22 mm and an outer jacket diameter of 0.24 mm. In the second case we have the advantage that by reducing the diameter of the fiber by three times

113
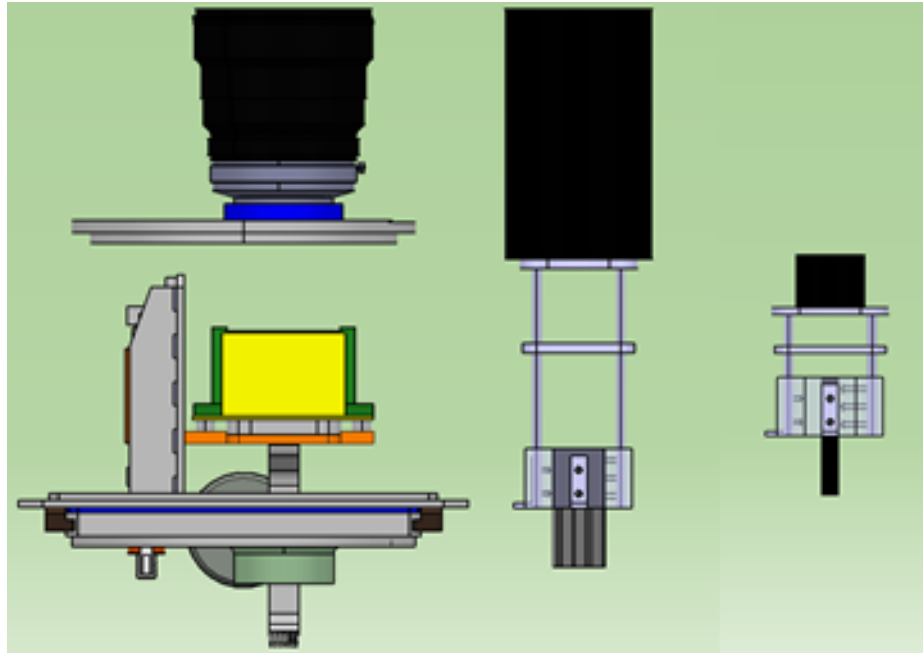
Figure 7.11: Comparison of the LIPAc FPM with cover removed (left) with the new proposals: the 78mm focal lens (center) and the 25 mm focal lens (rigth).

its cost is almost reduced by five (price comparison was done using multimode silica fiber from [96]), although the signal is weaker due to the smaller lens diameter. Each channel of the array is formed by 9 fibers, which are grouped in a protective metallic mesh sleeve. To make the installation easier and increase the protection of the fiber it is foreseen to group the channels in bigger sleeves. An additional fiber is planned to be attached to the bundle. This fiber will have the beginning at the TIR and end in the electronics room and will have double use: measure the background due to the fiber scintillation caused by radiation and monitor the fiber degradation.

Located further away from the radiation sources outside the TIR, the fiber bundles are separated in the different channels and coupled to an individual sensor, 31 per FPM and another for the background monitoring fiber. As most of the light is located in the visible part of the spectrum [105] due to Deuterium being the main component of the residual gas [123], we propose to use a SiPM since their efficiency in that range of wavelengths is higher compared to the classical PMTs. The sensor that we have selected is the SiPM array model S13361-3050NE-08 from Hamamatsu [2], which can be seen in Fig. 7.12, with 64 channels each one 3x3 mm. Using this sensor we are able to accommodate both vertical and horizontal FPM. For the electronics

an interface board from Vertilon specially designed for the sensor is selected [9]. The current measurements can be done by a standard multichannel charge amplifier, which should be capable to measure at least 0.1 pA currents with an interface compatible with the accelerator timing system. These requirements and selection of components are justified below in the signal estimation section.
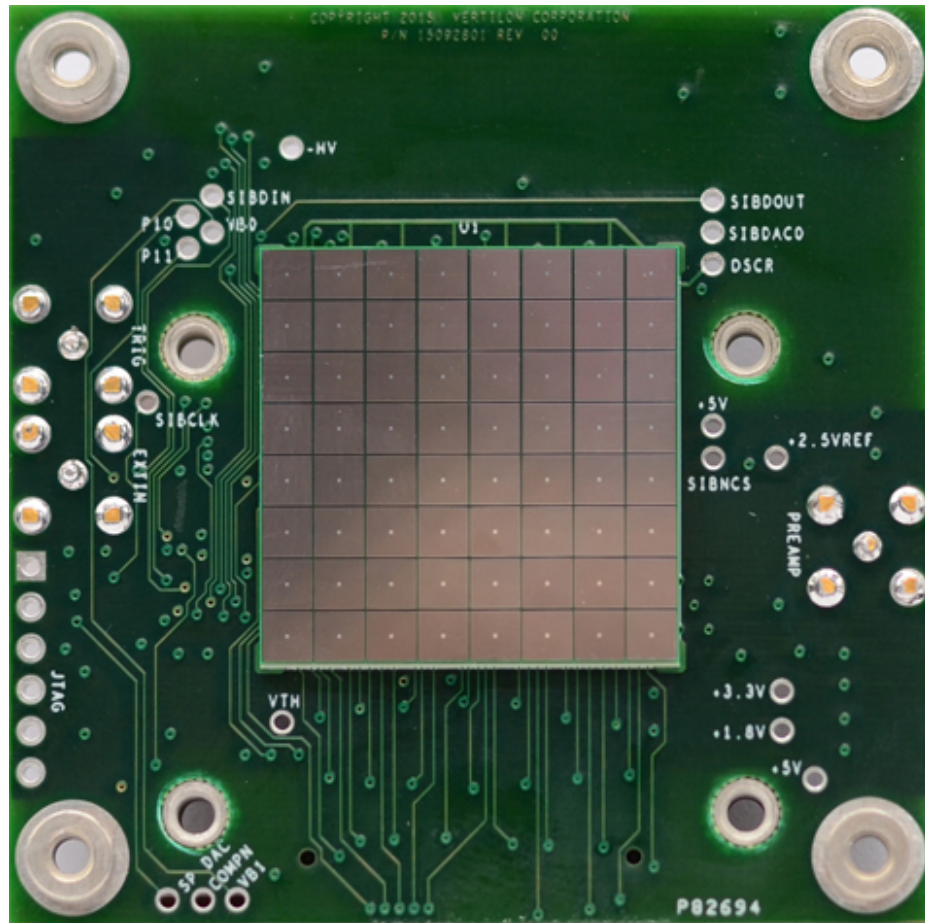
Figure 7.12: Hamamatsu SiPM array model S13361-3050NE-08 mounted on Vertilon interface board. Source [9].

7.3.2.3 Signal estimation

Prior to the manufacturing of a diagnostics, several calculations and simulations should be done. In a first approximation we will try to estimate the signal that will have to be measured by the light diagnostics. We will consider the full power beam of DONES, as for the cases of lower current and low duty cycle the obtained

signal will be proportionally reduced. The beam parameters considered are written in Tab. 7.5.

Particle	D^+
Kinetic Energy (MeV)	40
Current (mA)	125
Rest mass (MeV/c^2)	1876
β	0.203
γ	1.021
Charge (C)	$1.602 \cdot 10^{-19}$

Table 7.5: DONES's beam parameters considered for the calculations.

The number of photons emitted per second Y_{photon} is a function of the gas pressure P and temperature T, the beam current I, the particle charge q, the fluorescence cross section (σ) and the active length L, as is expressed in Eq. 7.2.

$$Y_{photon} = \sigma L \frac{PI}{qk_BT} \tag{7.2}$$

In this equation the beam parameters are given and already fixed and the active length will depend on the optical system (more precisely on the FOV at the sensor position). The particle gas density (P/k_BT) for our calculations have been obtained from [123], using a value of $5 \cdot 10^{-6}$ Pa (@300K). The most difficult data to obtain is the fluorescence cross sections, since no exact data for our main residual gas component (D_2) exist in our energy range. To estimate the total fluorescence cross sections we have followed two different approaches: in the first case we have extrapolated the fluorescence cross section for protons at 95 keV to deuterons at 40 MeV obtained from [83], and in the second case we have started from the ionization cross section for protons at 5 MeV [124] and make a rough estimation considering that the fluorescence is two orders of magnitude smaller. In both case the extrapolation is done using the Bethe formula. For the first case a cross section of $1.25 \cdot 10^{-24}$ m^2 is obtained, whilst for the second case we have a value of $1.70 \cdot 10^{-24}$ m^2. In our calculations we will use the worst case: $\sigma_{fluorescence} = 1.25 \cdot 10^{-24}$ m^2.

Since neither the light emitted by the deuterium nor the attenuation of the optical fibers is flat across the spectrum, we have to take into account the contribution of the main emission lines. We will use the criteria from [83], where the relative intensities of the different lines for Hydrogen are $H_\alpha = 1.65$, $H_\beta = 1.03$, $H_\gamma = 0.55$ and $H_\delta = 0.32$, and the total amount of photons is 2.15 times the H_α photons. The total number of generated photons is written in Tab. 7.6.

Wavelength (nm)	Photons generated ($m^{-1}s^{-1}$)
656	$1.04 \cdot 10^9$
486	$6.08 \cdot 10^8$
433	$3.08 \cdot 10^8$
410	$1.74 \cdot 10^8$
Total Balmer lines	$2.53 \cdot 10^9$

Table 7.6: Number of generated photons per second and unit length.

Not all of the emitted photons are able to reach the sensor. The first attenuation of the number of photons is due to the reflections in the interface between the air and the dielectric, which in our case is fused silica. We cannot include the losses in the lens since we do not know the exact number of elements. However, we can use the Fresnel equations 7.3 to calculate the transmittance in a dielectric surface due to the change in the refraction index between air (n = 1) and fused silica (n = 1.46). Since the angles of the light rays are small, we can consider it constant, simplifying the calculation and obtaining a transmittance of 0.965. This reflection only happens in the side of the fiber located in the vault, since the use of optical grease avoid this problem when coupling with the SiPM

$$T = 1 - \left| \frac{n_1 - n_2}{n_1 + n_2} \right|^2 \tag{7.3}$$

The second source of attenuation is the transmittance through the fiber itself. We have compared two materials from different manufacturers (fibers of equal dimensions): solarization resistant fibers from Thorlabs [125] and high OH UV/VIS fibers from Edmund Optics [96]. The attenuation values are resumed in Tab. 7.7. We have considered a tentative value of 25 meters for the fiber length since the building design and the cable layout is not fixed yet.

	Attenuation (dB/km)		Attenuation @ 25 m (γ_{out}/γ_{in})	
λ (nm)	E. Optics	Thorlabs	E. Optics	Thorlabs
656	9.4	6.5	0.947	0.964
486	20.5	15	0.889	0.917
433	29.6	24.6	0.843	0.868
410	31.5	32	0.817	0.832

Table 7.7: Comparison of the optical attenuation of the two fiber models.

In the sensor side we have compared six different kinds of sensors, five classical photocathodes: Multialkali, SuperBialkali and GaAsP from Hamamatsu [2], Hi-QE green from Photonis [126] and S20 UV from Proxitronic [97]; and one SiPM from Hamamatsu (S13361-3050NE-08). Its respective quantum efficiencies are shown in Fig. 7.13. Looking at the graph the most promising candidates are the GaAsP photocathode and the SiPM, both from Hamamatsu. The GaAsP has greater QE, it also has higher cost, and it is only available for image intensifiers, so needs a dedicated high voltage source and suffers from degradation over time, whilst the SiPM is cheaper due to the use of standard solid state technology and comes in a square array form. The gain from both systems is similar, in the order of 10^6.

Taking into account the filling factor due to the spectral efficiency of the photocathodes, the spectral attenuation of the fiber and the optical system characteristics (solid angle and fiber filling factor) we have calculated the number of generated photons per unit time in the active length that manage to get into the sensor in the case of the beam at 125 mA CW. In both cases we have done the calculations using the maximum aperture of the lens. After that we proceeded to calculate the amount of photons and electrons after and amplification of $4 \cdot 10^6$, which is a typical value for PMT and SiPM that does not push the devices into their limits (1 photon equals 1 electron after taking QE into account). In Tab. 7.8 and 7.9 we have put all the results for both optical setups together with the noise (per channel) that comes from the detector specified in maximum dark counts for the case of the SiPM [127] and the input photon noise background (derived from the Equivalent Background Input) for the MCP [128]. It is important to know that the noise generated by the radiation induced fluorescence in the fibers and optical glasses is not included.

As it can be seen on Tab. 7.9, the signal is very low, but within the limits
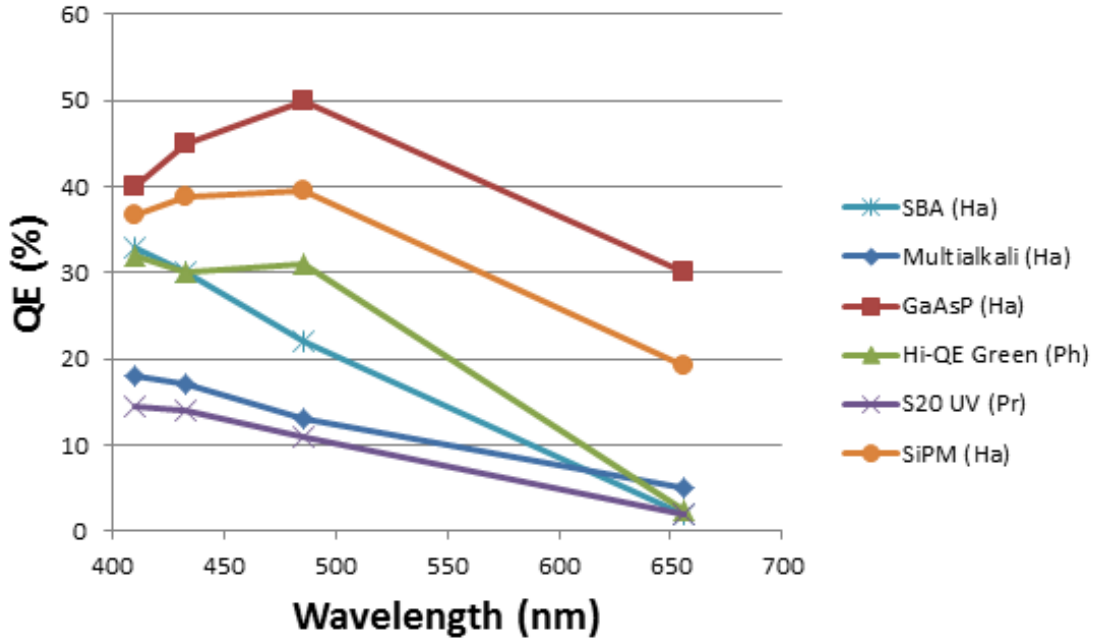
Figure 7.13: QE of the different detectors.

	25 mm focal Lens	78 mm focal Lens
Total signal (γ/s)	104	492
Background noise (γ/s)	199	1944

Table 7.8: Signal and noise for the MCP for the two different optical setups.

	25mm focal Lens	78 mm focal Lens
Total signal (γ/s)	194	856
Total current (A)	$1.24 \cdot 10^{-10}$	$5.48 \cdot 10^{-10}$
Dark Counts	$1.50 \cdot 10^{6}$	$1.50 \cdot 10^{6}$
Dark current (A)	$2.40 \cdot 10^{-13}$	$2.40 \cdot 10^{-13}$

Table 7.9: Signal and noise for the SiPM for different optical setups.

of our measurement capabilities, typically 0.1 pA. From the signal point of view the optical setup with the bigger apperture (78 mm lens) is preferable. This low level of signal is mainly caused by three factors: the low pressure in the chamber, low cross section and the very low solid angle subtended by the lens. This is because we have

located the lens quite far away from the beam (at 500 mm) in order to reduce the radiation dose absorbed by the optical components of our setup. However, since the final design of the beam line is not fixed, there is still room for improvement by getting the system close to the beam at the expense of radiation background radiation.

Depending on the kind of amplification used the detector needed is different: for the MCP the best choice is a camera where the image is further treated to average multiple frames and extract the information of each channel via software, but for the SiPM the best choice is a low noise multichannel charge integrator. In the case of the MCP we are limited to using CID cameras due to its radiation hardness, but their performance is significantly lower than CCD or CMOS cameras. Preliminary calculations using the latest available beam profiles from beam dynamics show that the setup with the optical fibers and the 78 mm focal length lens is enough to measure the transverse beam profile during nominal operation, as can be seen in Fig. 7.14.

.
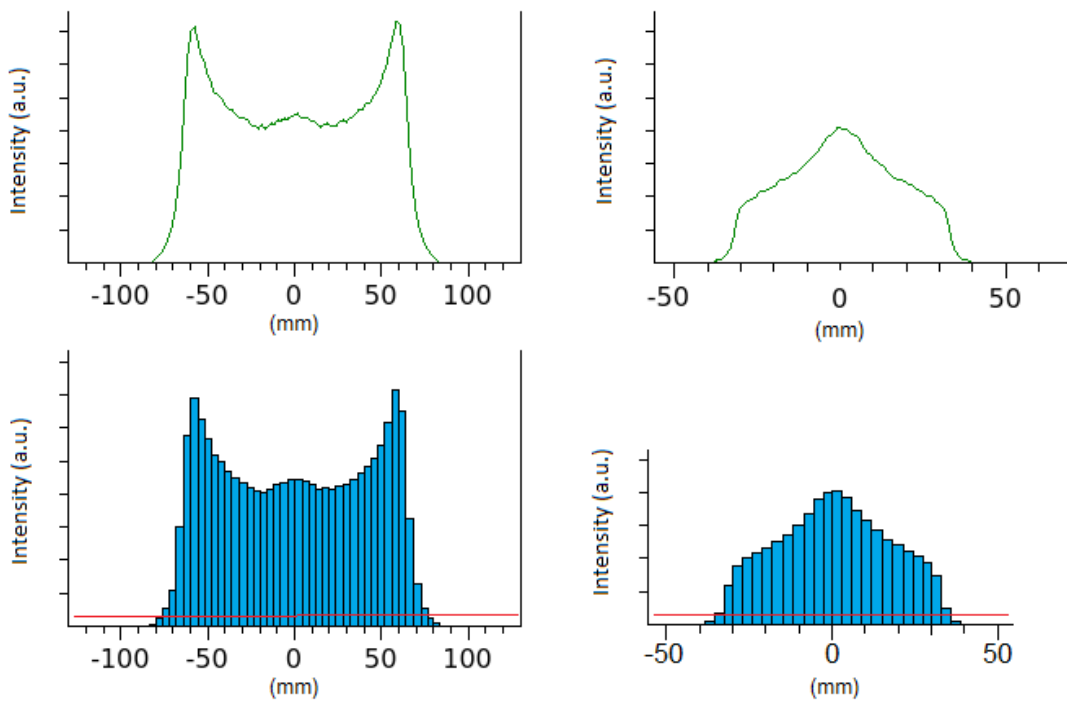
Figure 7.14: Simulation of the measured profile for the 78 mm focal lens at 125 mA CW. Horizontal (top left) and vertical (top right) profiles from beam dynamics compared with the simulation of the measured ones (bottom left and bottom right). Minimum measurable current of 0.1 pA is represented by the red line.

Chapter 8

Experimental measurements of DONES energy-like protons in gas and lithium enviroment

In order to obtain a uniform neutron flux profile, the DONES beam profile and position should be carefully monitored. In the case of transverse profile monitors two alternatives are candidates to be installed, the IPM and the FPM. Both of them have strengths and weaknesses which have been addressed in [129]. To evaluate the impact which the presence of lithium vapour will have in the FPM and the spectral properties of the emitted light by the fluorescence process an experiment has been designed, built and performed.

In the first case the foreseen problems associated with lithium are deposition in viewports and insulators, and possible distortions in the recorded profile due to non-homogeneities of its distribution. Nevertheless the extra amount of lithium vapour can enhance the signal since the fluorescence light will be added to that of the residual gas. Additionally, the spectral composition of the emitted light is essential for the selection of the detector, so the relative light yield of different gasses and the emission line strength is planned to be measured. The residual gas composition, as well as the lithium density along the beam pipe, has been addressed in [123].

Due to the low cross sections of the fluorescence process with the species

of the residual gas at 40 MeV, the number of generated photons is quite small, even with a deuteron 125 mA CW beam, as we calculated in Tab. 4.1. With respect to the residual gas, the residual gas pressure in the simulations of the DONES HEBT yield values in the order of 10^{-6} Pa for Deuterium [123] at 8 m before the beam interaction point, where the most critical FPM is planned to be installed. In the simulations all of the deuterium comes from the beam losses, and hydrogen is considered the most predominant gas in the outgassing of stainless steel according to [130]. Generation of Argon and byproducts of the D-Li nuclear reactions have also been considered in the lithium target. About the lithium presence [123] gives only the value of the deposited lithium in the walls, and results from [131] back the use of the Hertz-Knudsen equation and the cosine law for the evaporation of lithium. They also rise concern about the presence of impurities such as sodium or potassium due to their high vapour pressure. However, at the position of the diagnostic the lithium concentration is estimated to be orders of magnitude lower than other gases.

This has strong implications in the optical detector, because a small signal like that requires an amplification of orders of magnitude to obtain a good profile. Therefore the most suitable detectors for fluorescence measurements are photomultipliers arrays and intensified cameras. In both cases the element that determines the spectral efficiency and has a strong impact in the noise is the frontal photocathode, which has different properties depending on its composition.

As seen in Fig. 8.1, there are big differences between them, and knowing the spectral composition of the emitted light is the key to optimize as much as possible the spectral efficiency of the detector. The fluorescence light will be emitted by atoms and molecules excited by the beam, which mainly come from the residual gas, but also from the charge exchange of the beam ions, as seen Fig. A.3, where the peak of shortest wavelength (Doppler shifted D_α) represent the deuterium ions that were accelerated from the ion source but then have undergone the process of charge exchange and become excited atoms, whilst the peak of longer wavelength is the deuterium of the residual gas excited by the passage of the beam (D_α). From simulations a gas composition with Deuterium being the predominant gas is expected [123], therefore spectral properties of the emitted light may be similar from LIPAc injector, where deuterium is the most abundant gas. This fact is quite interesting, as the light will be concentrated in few lines in the visible spectrum (the Balmer series). However since most of the light will belong to the 656 nm line, we will not profit from high spectral efficiency and low noise when choosing a photocathode. This is
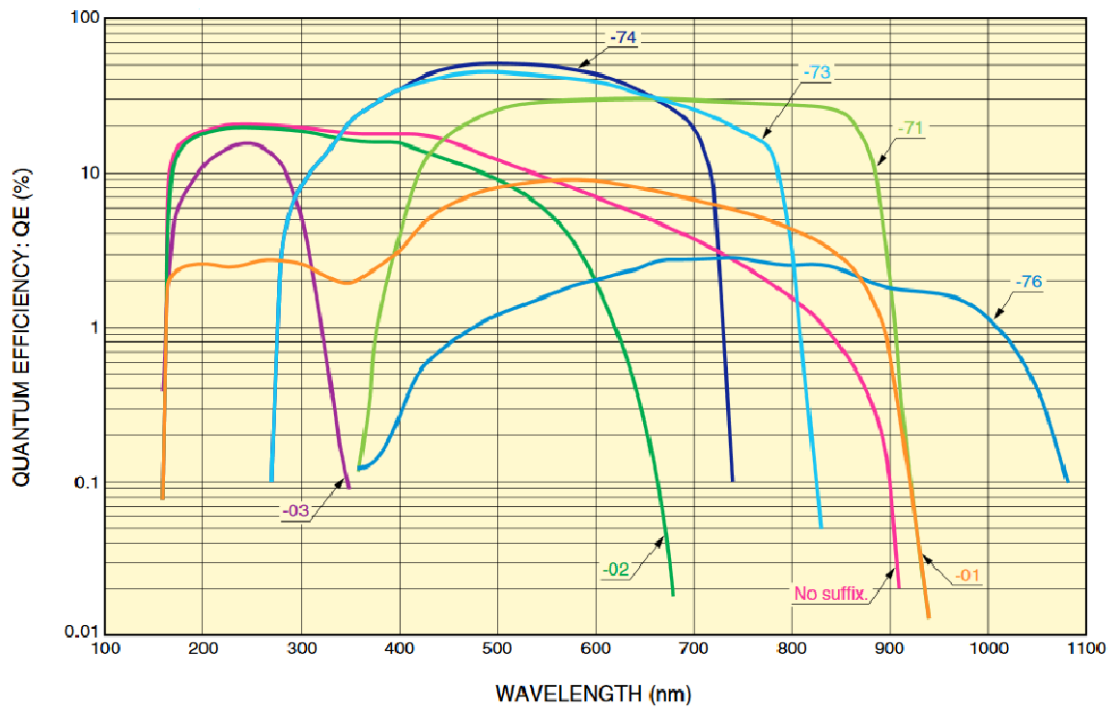
Suffix	Photo Cathode	Input Window	Suffix	Photo Cathode	Input Window
-71	GaAs	Borosilicate Glass	Non	Multialkali	Synthetic Silica
-73	Extended Red GaAsP	Borosilicate Glass	-01	Extended Red Multialkali	Synthetic Silica
-74	GaAsP	Borosilicate Glass	-02	Bialkali	Synthetic Silica
-76	InGaAs	Borosilicate Glass	-03	Cs-Te	Synthetic Silica

Figure 8.1: Quantum efficiency of different photocathodes [2]

the opposite case of the molecular Nitrogen (another of the most common residual gas), which concentrates its lines in the ultraviolet and blue range [132], just when the bialkali photocathode is the most efficient. Nevertheless this range is also the most affected by the radiation induced darkening of optical glasses [40]. In the case of the noble gases there are way more transitions than in the simple deuterium atom, thus they need photocathodes with higher bandwidth, as seen in Fig. 6.33, where the few Deuterium lines are clearly seen over the background but the Krypton ones are small but far more numerous.

8.1 Experiment description

The experiment goal was twofold: 1) evaluate the impact of a lithium vapour flow in the performance of FPM monitors and 2) study the relative light yield of the different lines in the fluorescence emission of several working gases when excited by protons. It was carried out in the cyclotron of the CNA at Seville [133]. Only two different particles are available from the cyclotron (IBA Cyclone 18/9), protons with a maximum energy of 18 MeV and deuterons with a maximum energy of 9 MeV. Due to the lack of deuterons at 40 MeV, we choose to use protons at 18 MeV, as its β is closer to the one of DONES deuterons (in fact it would be equivalent to 36 MeV deuterons). Since an external beam line was used, the final energy of the protons at the monitor location is about 15.5 MeV due to the loss of energy in the aluminium vacuum windows. This energy loss was an additional cause not to choose 9 MeV deuterons for the experiments, as the beam divergence would have grown significantly and its energy would have been greatly reduced. We assumed that the extrapolation using the Bethe scaling for the cross section holds in this case, therefore the theoretical fluorescence cross section would be given by Eq. 8.1.

$$\frac{\sigma_{40MeVD^+}}{\sigma_{15.5MeVH^+}} = \frac{\frac{\ln \beta_{40MeVD^+}}{\beta^2_{40MeVD^+}}}{\frac{\ln \beta_{15.5MeVH^+}}{\beta^2_{15.5MeVH^+}}} \approx 0.59 \tag{8.1}$$

Maximum average proton output current is limited to about 20 μA, thus the integration time should be scalated according to Eq. 4.11 in order to have the same photon yield as DONES.

8.1.1 Beam Line design

Due to the hazardous nature of pure lithium [134], it was decided to use an external beam line. The beam line itself was designed around standard off-the-shelf stainless steel components. It is built around a 6-way cross where the lithium oven and the borosilicate viewports are installed, followed by a wire grid chamber and then a long pipe up to the isolated graphite beam dump with an attached connection to measure the beam current. Made of aluminium to reduce induced activation and radiation generation if the beam hits it, the vacuum window was located at the front, and will

be described in detail later together with the collimators and the window foil. A complete picture of the line assembled in CIEMAT is shown in Fig. 8.2.
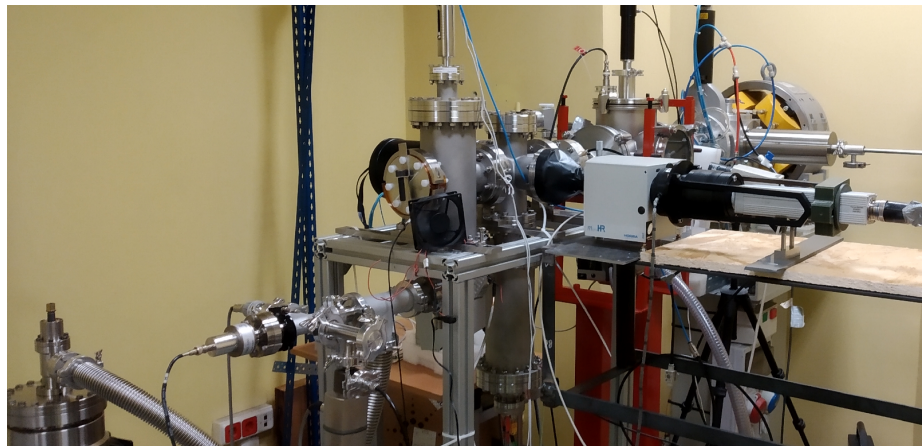
Figure 8.2: Picture of the full experiment line

8.1.2 Intensified Spectrometer

In order to study the contribution of the different emission lines to the beam profile, one of the FPM is an intensified spectrometer. We have chosen a microHR imaging spectrometer from Horiba Scientific [5], equipped with a 300 grooves/mm diffraction grating and a bandwidth of 500 nm (350-850 nm), whose quantum efficiency is displayed in Fig. 8.3. Front lens of the spectrometer is a 25 mm fixed focal length from Edmund Optics [96] with variable aperture. For the output a C-Mount thread has been selected where the detector has been installed. The detector itself is the ICID camera that was used during the LIPAc injector measurement campaign described in Chapter 6, with a BV 2581 BX-V 100 N MCP (with a P46 phosphor screen) based intensifier from Proxitronic (now Proxivision) [97], whose main characteristics are enumerated in Tab. 6.1, and its quantum efficiency displayed in Fig. 6.4. The CID camera is a 8726DX6 from Thermo Scientific [99] with its characteristics enumerated in Tab. 6.2.

The whole assembly is displayed in Fig. 8.4. The characterization of the system at the nominal working distance (180 mm) with both a LED array and a neon bulb yielded a calibration constant of 5.73 pixel/mm in the vertical plane. In the horizontal plane the spectral calibration was performed since the wavelength counter

126
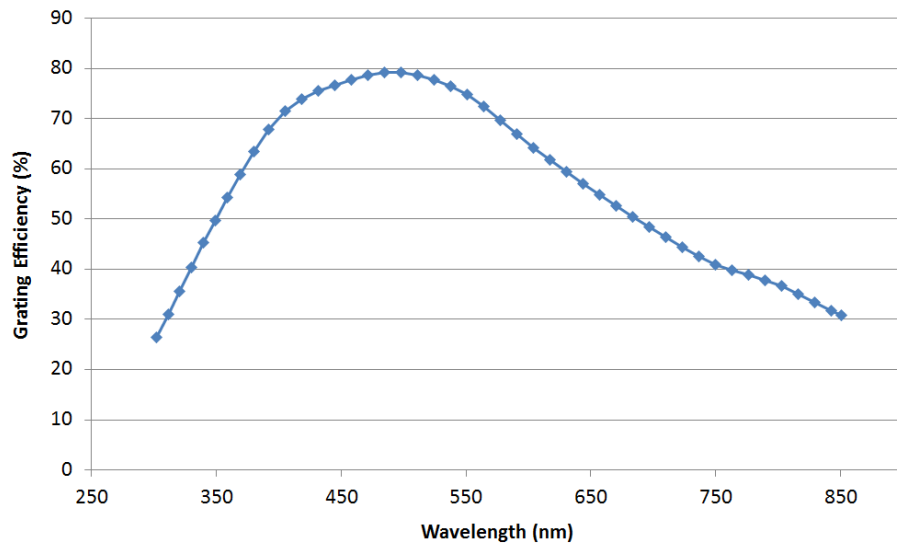
Figure 8.3: Diffraction grating efficiency according to the manufacturer [5].

did not correspond to the actual wavelength, as it is designed to be used with a 1200 lines/mm difraction grating, and we used one with 300 lines/mm to obtain wider spectral coverage. By rotating the grating and measuring the peak we obtained a relationship of 0.1597 nm/pixel between the counter and the pixel position. Figure 8.5 shows the LED board used for the dimensional calibration, as well as the zeroth and first orders of diffraction.
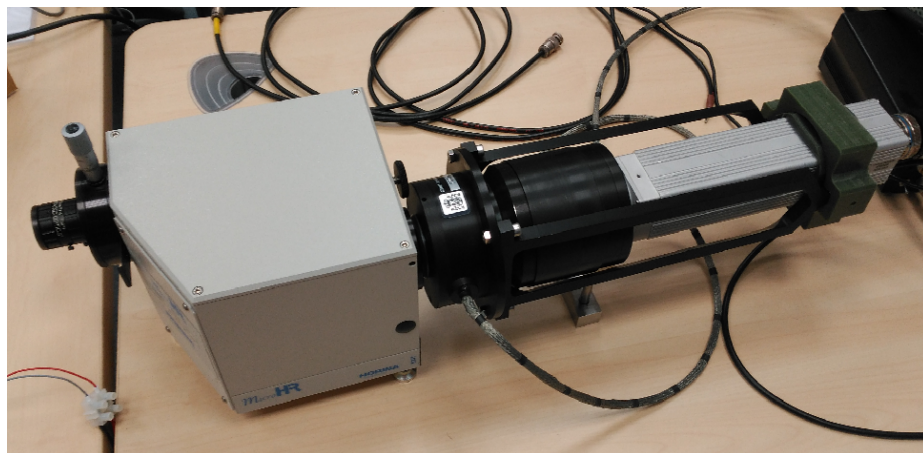
Figure 8.4: Assembly of microHR spectrometer with the image intensifier and the CID camera.
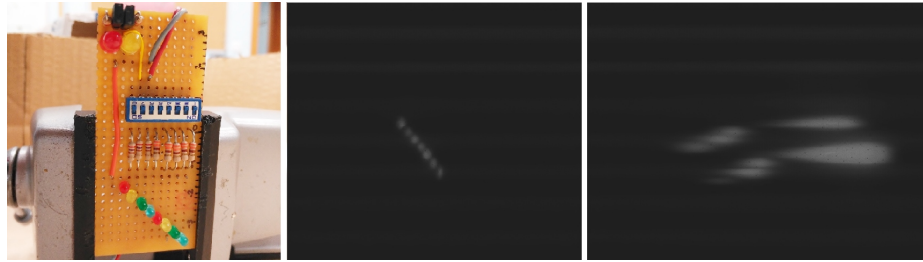
Figure 8.5: LED spatial calibration board (left). Zeroth order of diffraction (center). First order of difraction (right).

8.1.3 PMT based FPM

A PMT array was installed in front of the spectrometer, thus a direct measurement of the impact of lithium vapor and different working gases could be obtained. The PMT itself [53] is identical to the ones installed in LIPAc and one of the candidates to be installed in DONES. It was designed around a Hamamatsu H7260 32 channel PMT array [135], whose main specifications are described in Tab. 8.1. The system adjustment is done manually over a Carl Zeiss Planar T lens and a moveable carriage, with the posibility to change the focus and the position of the detector. A picture of the detector is found on Fig 8.6. The charge readout of the PMT is dones by a PhotoniQ IQSP 482 data acquisition system from the compary Vertilon [9], with its main specifications listed in Tab. 8.2. The system can be seen in Fig. 8.6.

Transmission window	Quartz
Photocathode material	Bialkali
Number of channels	32
Gain	$2 \cdot 10^6$
Channel area	0.8 x 7 mm^2
Channel separation	0.2 mm

Table 8.1: H7260 PMT array specifications.

Number of channels	64
Resolution	16 bits
Dynamic range	96 dB
Input noise charge (typical)	30 fC RMS
Channel cross talk (typical)	-84 dB
Maximum trigger rate	120 kHz

Table 8.2: Vertilon PhotoniQ IQSP482 specifications.

Figure 8.6: PMT array based FPM (left). Vertilon DAQ (right).

8.1.4 Wire grid

In order to cross check the profile measurements obtained with the PMT array and the imaging spectrograph it was decided to built a simple 15 horizontal wire SEM grid. The wires are made from tungsten in order to have a high melting point. To minimize energy deposition while keeping high signal the diameter of them is 80 μm, and they are spaced 2 mm. They are mechanically connected to the output wire and preloaded with a Cu-Be spring to keep the tension. The fifteen cables are connected to a multiplexer board and the reading is performed sequentially with a Keithley 6485 [136] picoammeter. The grid itself is shown in Fig. 8.7

Thermal simulations were performed using Ansys [137] considering the worst case: maximum surface, profile peak intercepted and the maximum extracted current from the CNA cyclotron (20 μA). The transverse beam profile of CNA for this exper-
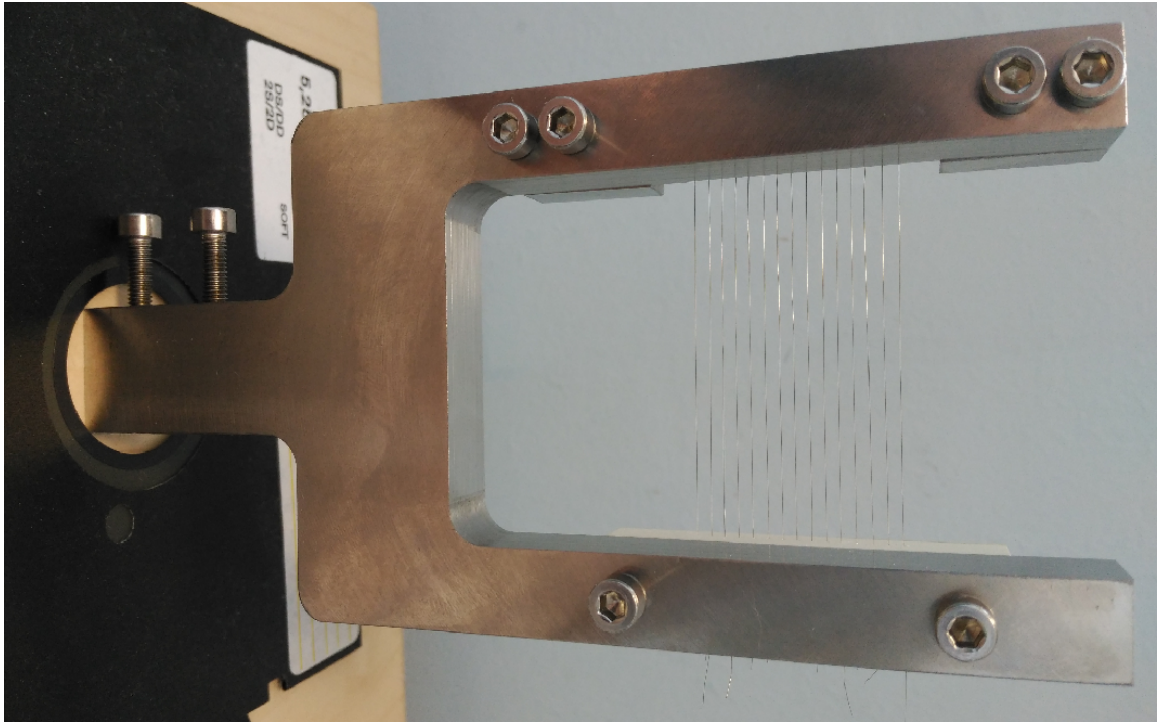
Figure 8.7: SEM grid assembly.

iment was a symmetric gaussian of $\sigma = 7$ mm. In our simulations we considered the case of a wire in the middle of the beam, intercepting the peak and a full diameter of the beam. In order to simplify the simulations while being conservatives the power deposition was considered constant in the volume of the wire. This assumption implies that the deposited energy is constant along the direction of the beam and the beam transverse profile is uniform. For this case the first hypothesis is justified, the power deposition varies slowly and we can average it, as seen in Fig. 8.8 the result of the SRIM calculation [116]. In the second case we will substitute the real transverse beam profile with the one corresponding to a circular uniform beam with the current density equal to the gaussian current density peak and with a radius $r_{uniform} = \sqrt{2}\sigma_{beam}$. The current density of the uniform beam is given by Eq. 8.2. The values used for the simulation where $r_{uniform} \approx 10$mm and $J_{peak} = 0.13$ μA/mm^2.

$$J_{peak} = \frac{I_b}{2\pi\sigma_b^2} \tag{8.2}$$

The protons come to our vacuum chamber with an energy of 15.5 MeV due to the losses in the vacuum windows, losing approximately $2.8 \cdot 10^4$ eV/μm (averaged)
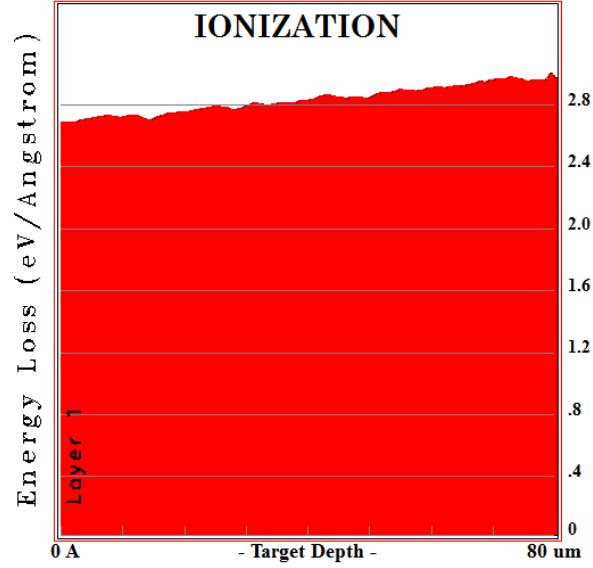
Figure 8.8: Energy deposition of 15.5 MeV protons along 80 μm of tungsten calculated using SRIM.

in their passage across the 80 μm tungsten wire. The total power deposition per unit volume P_{vol} is given by Eq. 8.3, where $\frac{\Delta E}{\Delta x}$ is the energy lost per unit length by ionization losses and J_{beam} the beam current density.

$$P_{vol} = \frac{\Delta E}{\Delta x} J_{beam} \tag{8.3}$$

The volumetric heat deposition in our case is $P_{vol} = 1.82$ W/mm^3. Only radiative losses have been considered in our model (worst case). The emissivity values, which are temperature dependent, are given by interpolating the values of Tab. 8.3. Conduction losses were discarded since on both ends the cable contact with the spring and the mechanical clamp is very small and all of the components are mounted on an insulator. Convection losses are not existent due to the high vacuum state, and losses due to electron emission (thermionic losses) have not been considered either, since results for the simulation yield temperatures low enough to release thermionic electrons.

The results obtained in the simulations, displayed on Fig. 8.9, guarantee a very high safety margin between the maximum temperature reached in the stationary state (1367 K) and the melting point of tungsten (3695 K). Temperature at the Cu-Be

ε	0.02	0.03	0.07	0.13	0.23	0.28
T (C)	25	100	500	1000	1500	2000

Table 8.3: Emissivity of unoxidized tungsten.
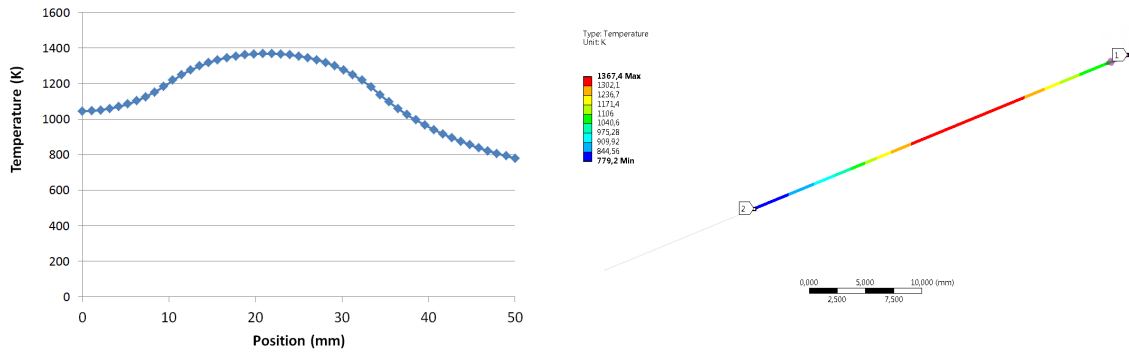
Figure 8.9: Temperature of the tungsten wire in the stationary state.

spring side (779 K) is also lower than the alloy melting point (1140 K). Transcient simulations (Fig. 8.10) show that the stationary temperature (global maximum) is obtained in a relatively short time, ≈ 3 s, and is located in the center of the beam. The minimum temperature did not change during that period of time, as the thermal wave did not have enough time to propagate due to the small diameter of the wire compared to its length.
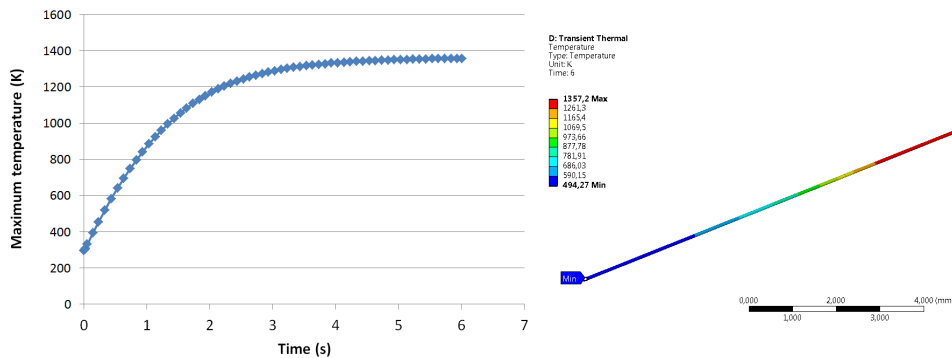
Figure 8.10: Temperature of the wire during a transient period of 6 seconds after applying the thermal impulse.

In order to crosscheck the simulations results with the theoretical values we calculated the temperature in the stationary state of an infinitely long cylinder of the same diameter and volumetric heat deposition, considering only radiative losses

given by the Stefan-Boltzmann law (Eq. 8.4) taking into account the temperature dependence of the emissivity given in Tab. 8.3. The temperature obtained was 1598 K, 231 K above the simulation one, which is quite a good agreement even though the full geometry has not been taken into account and conduction is neglected. A summary of the inputs and results is given in Tab. 8.4

$$P = A\sigma\varepsilon\left(T\right)T^4 \tag{8.4}$$

Beam Current (μA)	20
Time structure	CW
Beam Energy (MeV)	15.5
Energy Lost (eV/μm)	$2.4 \cdot 10^4$
σ_b (mm)	7
Maximum Temperature (K)	1367
Tungsten melting point (K)	3695
Temp. @ Spring side (K)	779
Spring melting point (K)	1140

Table 8.4: Inputs and results of the wire thermal simulation.

8.1.5 Vacuum system and Beam Window

The short beam line is kept under high vacuum during the experiment. Our vacuum system was a mobile pumping station composed of a turbomolecular pump (Agilent TV 551 Navigator) backed with a dry scroll pump [138]. The vacuum system is shown in Fig. 8.12. Although the pumping speed is relatively high, about 550 l s^{-}1 for N_2 and 510 l s^{-}1 for H_2, we only were able to reach about $8 \cdot 10^{-7}$ mbar due to the long connection with the KF40 pipe to the experiment.

In order to inject different gases in the beam line we choose a EVR 116 gas regulating valve from Pfeiffer [139], with a closed loop control using the RVC 300. Several test were performed using nitrogen to check the response of the system to
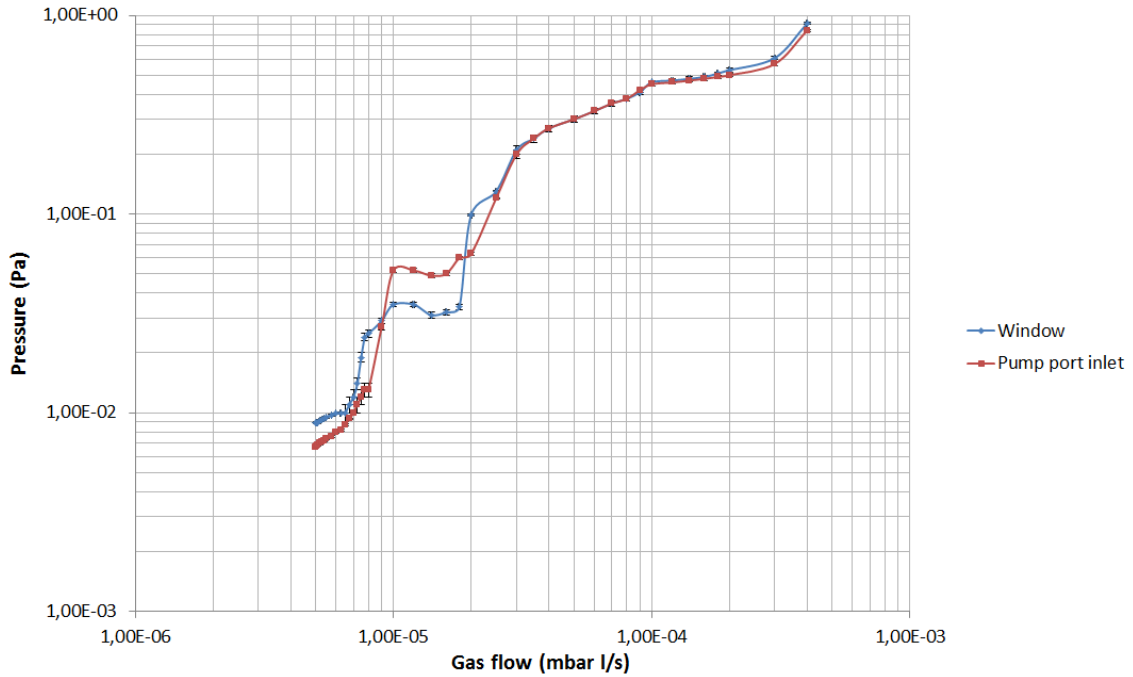
Figure 8.11: Pressure dependence on the injected gas flow measured with a cold cathode pressure gauge at the window location (blue) and pumping pipe inlet (red).

an increase of the gas flow measuring the pressure at the aluminium window and the pumping station connection. One of scans is shown in Fig. 8.11.

The most delicate part in our beam line are the vacuum windows, which are needed to let the beam pass to the chamber. In order to minimize risks a double window with a buffer of Argon gas at a pressure of 1.2 bar was constructed. Hence, if the inner window breaks, because is the one under the highest pressure and heat load, the chamber is filled with the pressurized Argon, thus avoiding any reaction with the molten lithium. We also added a pair of ring collimators made of graphite in order to reduce the activation of the material in case of an excesive size of the beam or undesired steering that causes the beam to hit on the window. Fig. 8.13 shows the full assembled window without the foils.

Based on previous experience from CNA, aluminium was selected as the window material, providing a good tradeoff between energy lost (6.8 keV/μm with protons at 18 MeV) and mechanical and thermal properties. The first approximation to determine the appropiate thickness was to consider a circular plate supported on the side under an uniform load, which can be solved anallitically [140] using Eqs. 8.5

Figure 8.12: Mobile pumping station used in the experiment.

and 8.6 to calculate the maximum stresses and deflection with respect to the Young's modulus E, the pressure p, the diameter a and window thickness t.

Figure 8.13: Assembled vacuum window without Aluminium foil.

$$S = 0.27 \left[E \left(\frac{pa}{t} \right)^2 \right]^{\frac{1}{3}} \tag{8.5}$$

$$w = 0.26 \left[K \frac{pa^4}{Et} \right]^{\frac{1}{3}} \tag{8.6}$$

The calculated maximum stress due to atmospheric pressure in the center is 82.8 MPa, with a maximum transverse deflection 0.428 mm. The aluminium mechanical properties considered were a Young's modulus of 70.6 GPa with an ultimate tensile strength (as specified by the vendor) between 130 and 180 MPa.
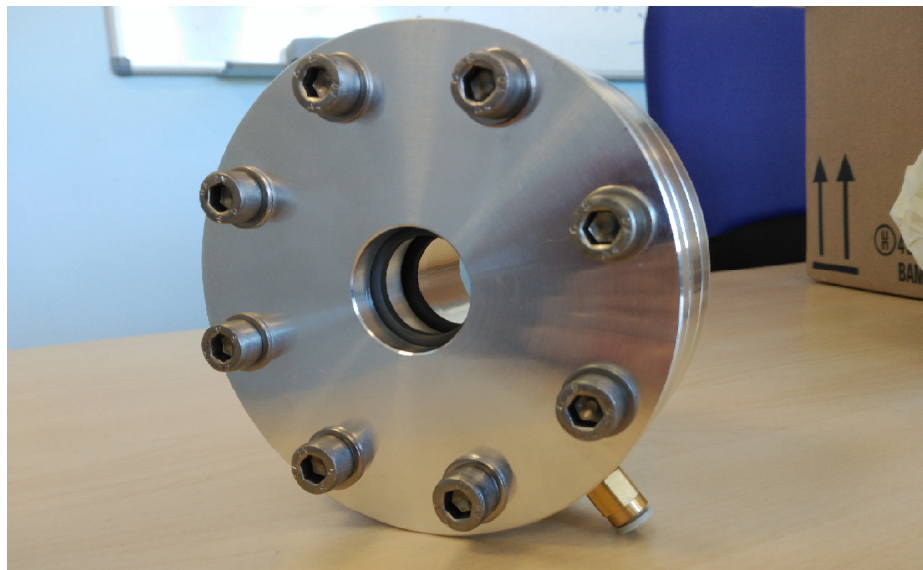
Following this analysis a thermomechanical simulation was done using ANSYS Mechanical [137]. In this simulation the heat load was calculated first, and then the mechanical load was applied. The circular gaussian profile was recreated using 7 concentric flat rings considering the maximum beam current case. The heat losses were considered only due to radiation, with $\varepsilon = 0.08$, and convection with air, only in one side and with a constant coefficient of 1 W/mm^{2}K (safe assumption for non forced flow). The results of the thermal simulation for the foil is shown in Fig. 8.14, where a maximum temperature of 183 ºC is obtained in the centre of the disk.

For the thermomechanical simulation the load applied was uniform and equal to 1.2 bar. For the sake of simplicity the isolating o-rings have not been included on the simulations and the whole window assembly has been removed. Results of the mechanical simulation using a shell model along a radius are displayed in Fig. 8.15 for the upper, middle and lower part of the foil. These result predicts a safe margin in the working point of the system for the middle of the shell, since the manufacturer specifies a yield strength between 110 and 170 MPa, and a tensile strength between 130 and 190 MPa. However, since these margins are quite wide and the simulations predict some values above the limits for the upper and bottom sides, it was decided to manufacture the window with collimators of different diameters and test them. The results were satisfying, but only after rounding the edge of the collimators, which was permanently deforming the foil, as it is shown in the simulations, where the peak of the top part exceed the yield strength limit.
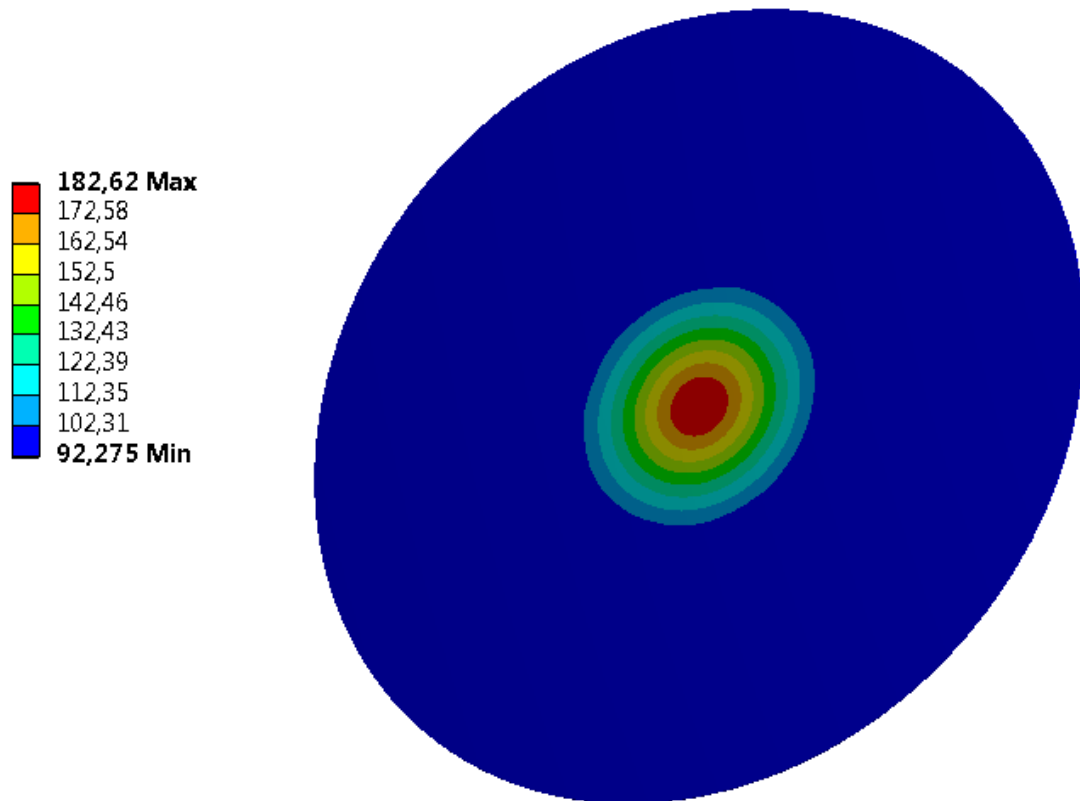
Figure 8.14: Temperature results (in °C) of the window's thermal simulation. Only the foil disk is shown for simplicity.
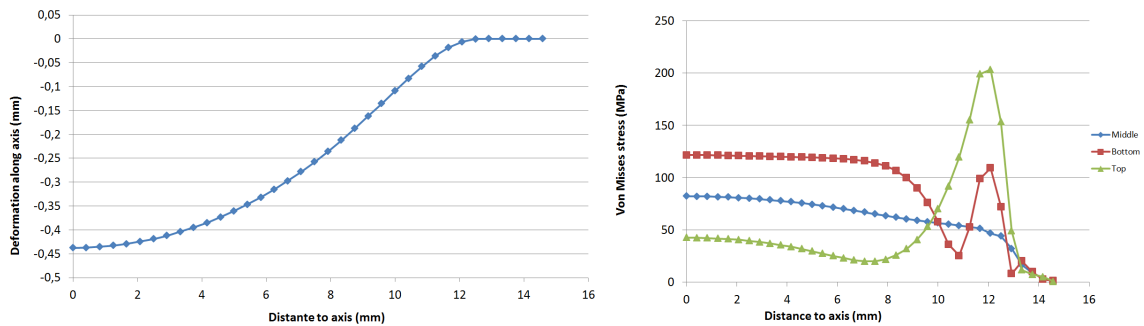

Figure 8.15: Radial profiles obtained with the mechanical simulation. Deformation along axis (left) and Von Misses stress (right).

8.1.6   Lithium Oven

At room temperature lithium is a white solid metal with a low melting point which reacts with air and water. Therefore it must be kept in a protective medium like a

137

noble gas or parafin. In our experiment we chose to use lithium pellets in an argon filled gas. Special care must be taken when manipulating lithium, as its dust affect the skin, lungs and eyes, and in contact with water it can catch fire. A dedicated in vacuum oven was manufactured at CIEMAT and installed in our short beam line in the bottom of the FPM chamber. The pellets are deposited in a cylindrical crucible, which is tightly held by a 550 W coil resistor, as can be seen in Fig. 8.16. The temperature of both the liquid lithium and resistor is read by a K-type thermocouple.
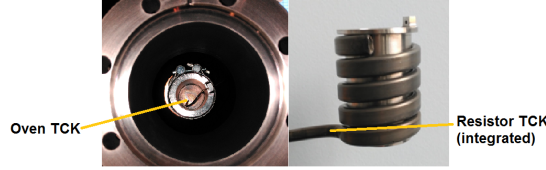
Figure 8.16: Lithium oven mounted on pipe (left) and stainless steel crucible with coil resistor extracted (right). One thermocouple is integrated in the resistance, the other is seen inside the oven in the left picture.

Experiments with liquid lithium in the frame of IFMIF-EVEDA [131] have shown that the evaporation of lithium j_{evap} can be accurately described by using the Hertz-Knudsen law (Eq. 8.7) and considering that in the evaporation process the directional dependence of the flow follows a cosine variation along the angle with respect to the normal to the surface.

$$j_{evap} = \eta \left(P_v \left(T_e \right) \sqrt{\frac{M}{2\pi R T_e}} + P \left(T_g \right) \sqrt{\frac{M}{2\pi R T_g}} \right) \tag{8.7}$$

In the previous equation j_{evap} is the evaporated mass flow per unit time, η the evaporation coefficient, P_v the vapor pressure of the liquid surface, P_g the partial pressure of the vapor, T_e the temperature of the liquid surface, T_g the temperature of the vapor, M the molecular mass and R the universal gas constant. In our setup we control the power in the resistor using the PWM technique, thus mantaining a stable temperature, which is associated to a certain partial pressure of the vapor, as is seen in Fig. 8.17. The total flow and its spatial variation is computed using the geometry of our oven and the distance to the beam.

Two different strategies, both based on PWM, were tested regarding the temperature control. First we tried to control using PI and PID controllers, but the
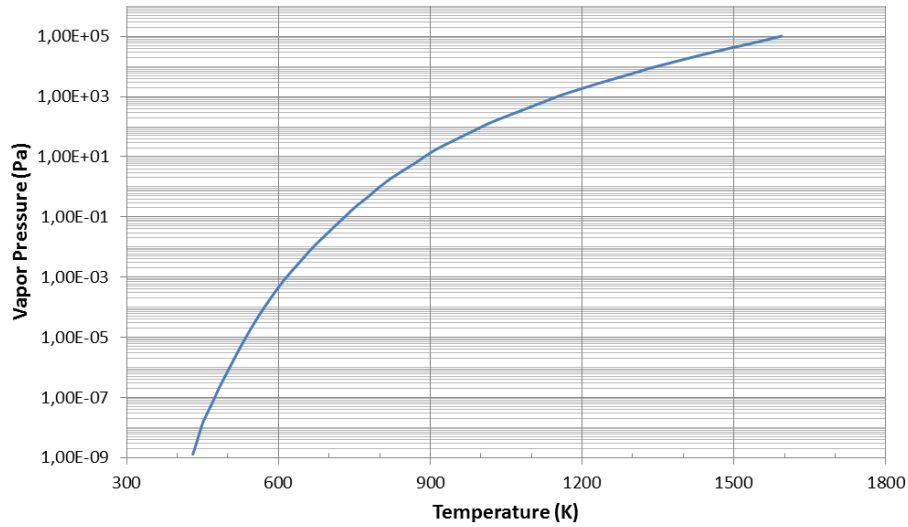
Figure 8.17: Lithium vapor pressure as a function of the temperature. Source: [10].

system proved to be very unstable in both cases. Hence we decided to control the temperature using an open loop control scheme by controlling the average power with PWM using a solid state relay. Using a 220 V AC power supply the maximum power in CW mode is 550 W. The results of the maximum temperature reached (at an ambient temperature of 27 °C) as a function of the duty cycle are displayed in Fig. 8.18. A temporal series with the transit time behaviour is displayed in Fig. 8.19.

8.1.7 Beam Dump

The beam is safely stopped at the end of the chamber, where a beam dump has been installed. Graphite was decided to be used in order to mitigate as much as possible the material activation. The beam dump itself is machined from a standard stainless steel CF63 flange, where the graphite plate, 5 mm thick, is fixed with four aluminum screws located radially, with enough space to compensate the expansion of the graphite plate. In order to achieve better heat disipation, a heat sink was installed in the back of the flange with an electrical fan. The Beam Dump is shown in Fig. 8.20.

The whole assembly is isolated from the rest of the beam line using a PTFE gasket and nylon bolts. A wire is attached to the assembly in order to measure the
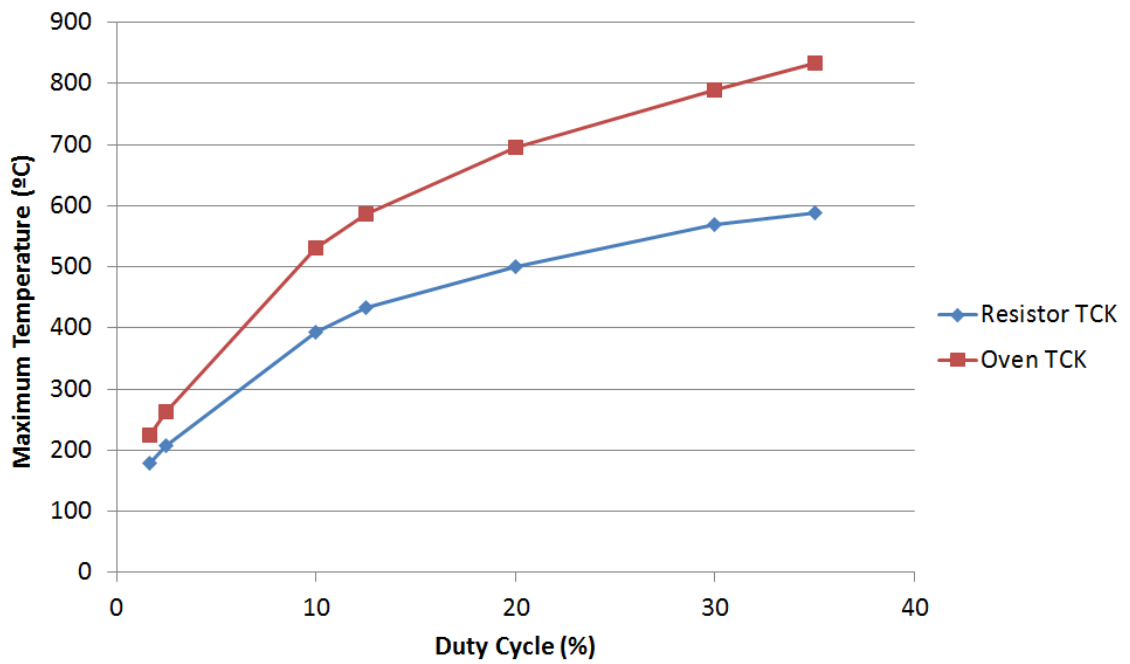
Figure 8.18: Maximum temperature reached as a function of the duty cycle.
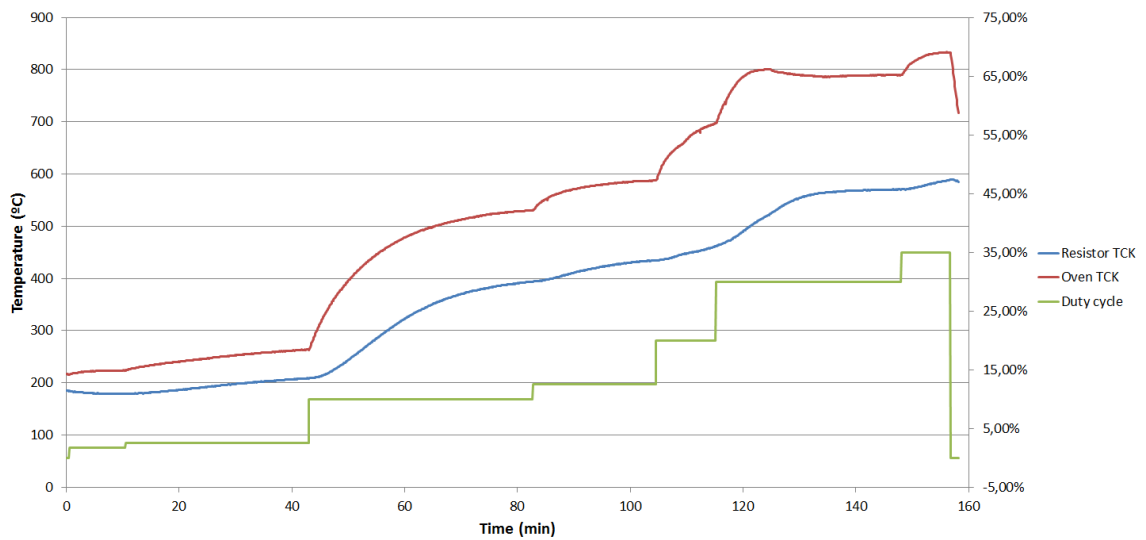
Figure 8.19: Time series of the temperature evolution of the oven at increasing duty cycles.

beam current, and secondary electron emission is supresed by the magnetic field of a Neodymium-Iron-Boron magnet inserted in the flange.
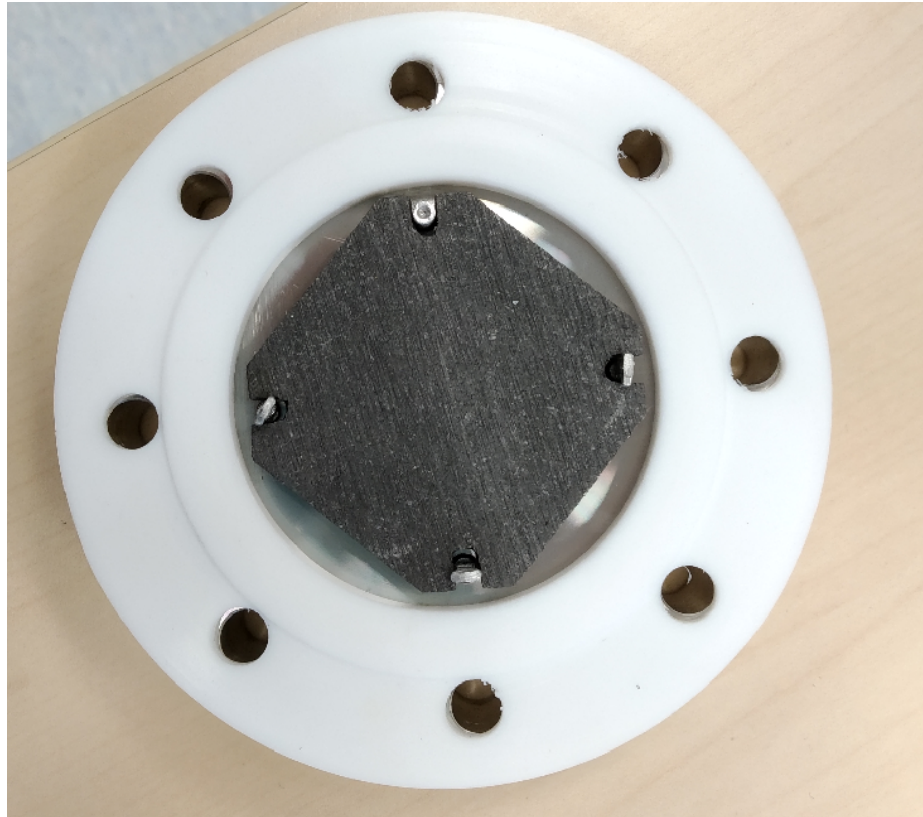
Figure 8.20: Beam Dump before the installation in the beam line.

8.1.8 Electronics and control system

For this experiment it was decided to integrate all of the systems in order to be able
to control it using only one PC. The full system is represented in Fig. 8.21. The main
components are the detectors: 1) the PMT array, 2) the intensified spectrograph and
3) the SEM grid. The PMT array (Hamamatsu H7260) along the Vertilon IQSP482,
are controlled directly with the PC via USB 2.0. The spectrograph itself is manually
set in a position to cover almost the whole visible spectrum (due to the appropiate
selection of diffraction grating and sensor size), but the MCP of the intensifier needs
the appropiate signals for controlling the gain (DC from 0 to 5 V) and gating (square
wave TTL 50 Ohm), whilst the CID has its own electronics box, providing a 30 fps
video via a USB 2.0 output, whose frames are recorded using the OpenCV library
of Python. The third detector is the 15-wire SEM grid, its current signals measured
with the single channel Keitley 6485 picoammeter and a multiplexer board. The gas
injection and the control oven are controlled by microcontrollers with the appropiate
interface circuits. The custom made boards fit in an electrical box, which is shown

in Fig. 8.22. A more in depth description of the control system and the low level hardware is given in Appendix 2.
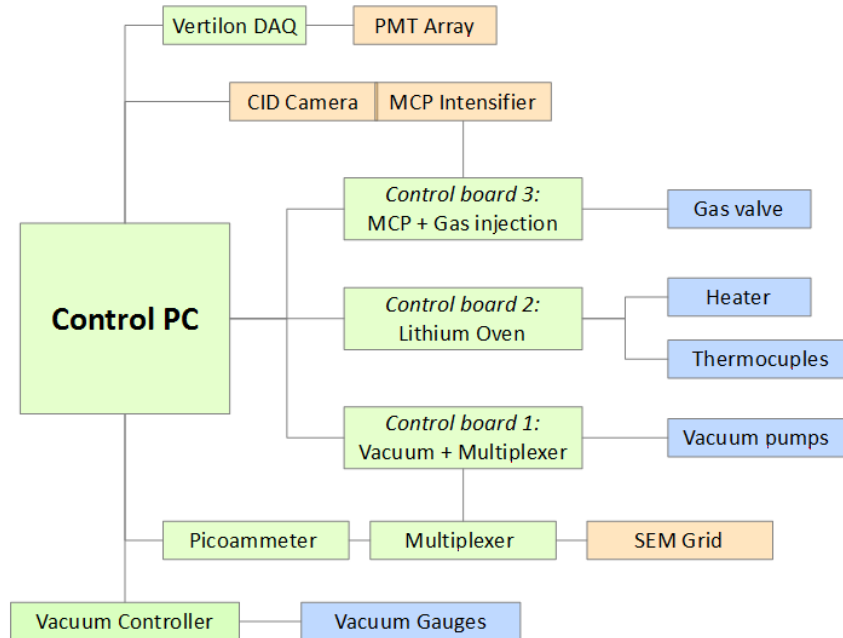
Figure 8.21: Box diagram of the control system.

8.2 Experimental Results

The first tests took place in March of 2019. Due to the limited available time, the assembly was done in one day and a half, and two days of beam time were used. During the assembly several test of the electronics were performed and nothing abnormal was found. Nitrogen was the selected gas to be injected at first. After the assembly we started the vacuum pumps, who were only able to pump up to slightly less to 10^{-3} Pa due to the limited time before performing the experiments. In order to avoid any kind of damage on the window, it was decided to start increasing the beam current slowly and perform first the measurements with the injected gas before proceeding with the lithium vapor.

The PMT array worked properly. It was controlled with a new version of the LIPAc FPM control system, which proved to be vastly superior to the software supplied by the manufacturer and with previous versions of the custom made software.

142
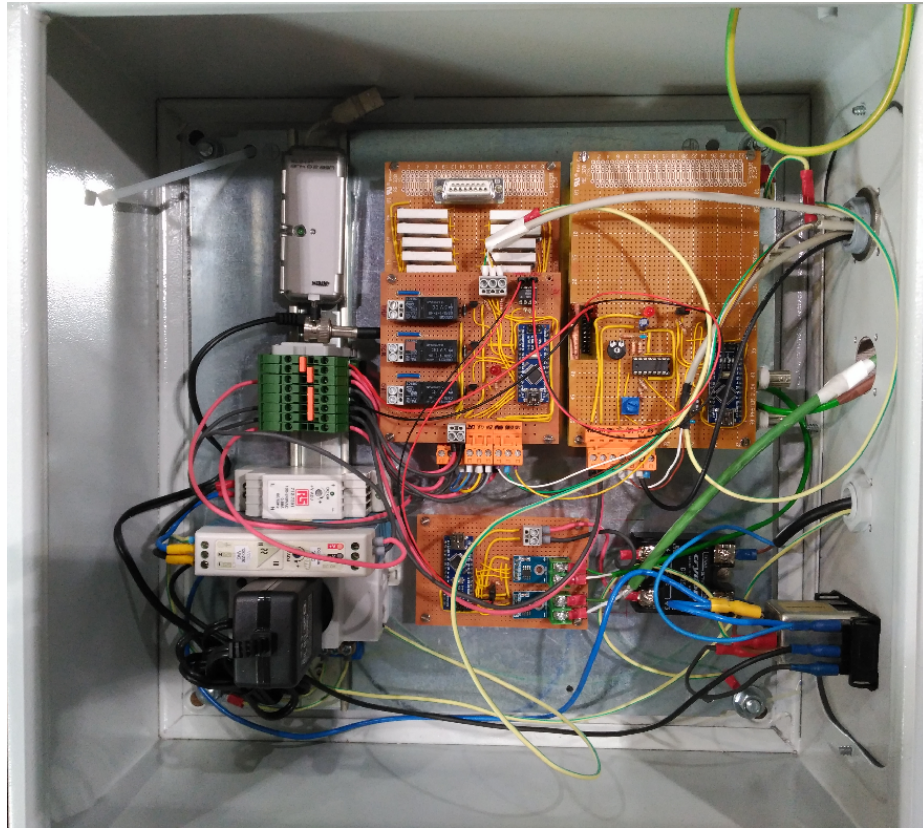
Figure 8.22: Electrical box containing the auxiliary electronics.

The first profile clear was observed with 150 nA and $9 \cdot 10^{-3}$ mbar of nitrogen. The conditions (number of emitted photons) under which the beam was observed were consequent with previous experiments performed at CNA and LIPAc. After playing with the current up to the allowed maximum, it was decided to settle the beam current at 1.1 μA in order to have a good compromise between signal, radiation background and thermal load at the windows and beam dump. Radiation levels at the FPM position due to the impact of the 15.5 MeV protons in the graphite target were 153 mSv/h and 207 mSv/h for neutrons and gamma respectively. Preliminary results from MCNP calculations in DONES give 1 Sv/h of gammas and 100 Sv/h of neutrons in the TIR room at the FPM position during normal operation. In the following discussion the beam profile are shown as obtained, with no gain uniformity correction due to the unavailability of a uniform light source.

Three different runs were done in order to characterize the response of the PMT array with injected gas. In the first we varied the gain voltage to observe the changes in the observed profile, offset and the RMS noise, in the second run we

143

observed the effects of the pressure and integration time at fixed beam current and gain voltage, whilst in the third test we changed the value of the steerers to measure the position resolution of the fitting algorithm.
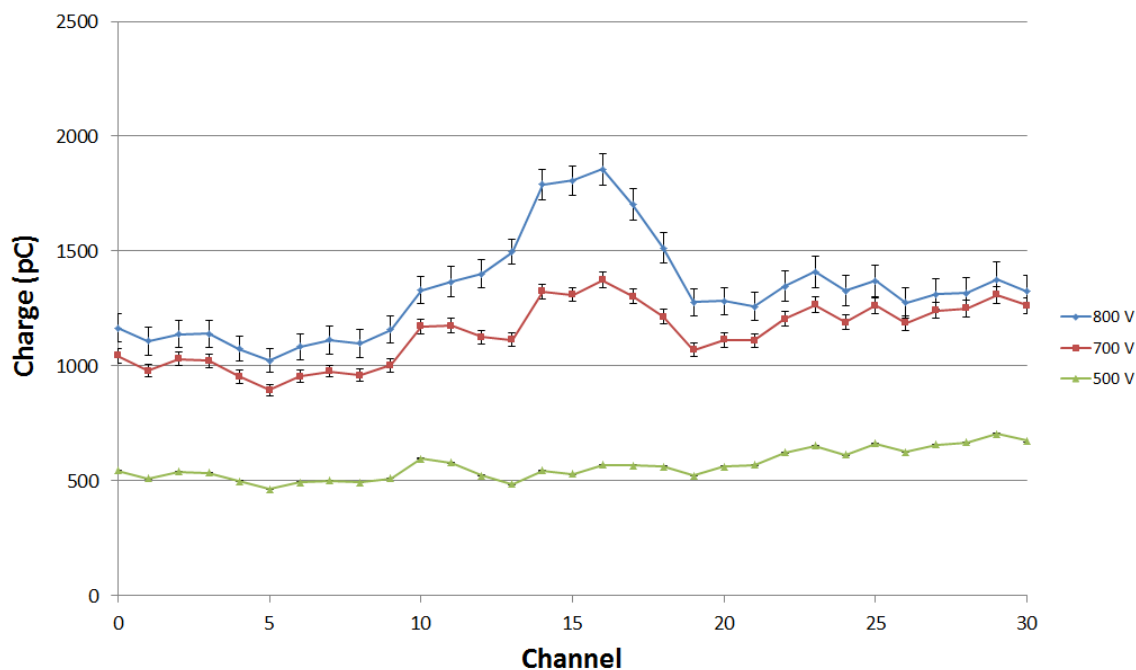
Figure 8.23: Measured beam profile at different gain voltage.

The results obtained in the first run are shown in Fig. 8.23. The pressure during these measurements was set at $1.0 \cdot 10^{-2}$ mbar and the integration time to 10 ms, with a trigger frequency of 1 Hz. As can be seen, the higher the gain the higher the current, but increase the offset and the error bars. At the lowest represented gain, 500 V, no beam could be seen, but as we increase the voltage the beam started to appear. However, both the background current and the error bars are greatly increased, as it is expected from the variation of the PMT gain with the polarization voltage, which is exponential according to the manufacturer, as it is shown in Fig. 8.24. If the RMS error (or noise) is represented as a function of the gain voltage, like in Fig. 8.24, its exponential growth is also clearly seen. It is also quite uniform along the channels. This kind of behaviour shows that the main source of noise is closely related is amplified by the PMT together with the signal. If the offset is represented as a function of the gain, an exponential behaviour is obtained, which asymptotically goes to 500 pC, the baseline level for our radiation background (the readout electronics were also inside the irradiation room).

144
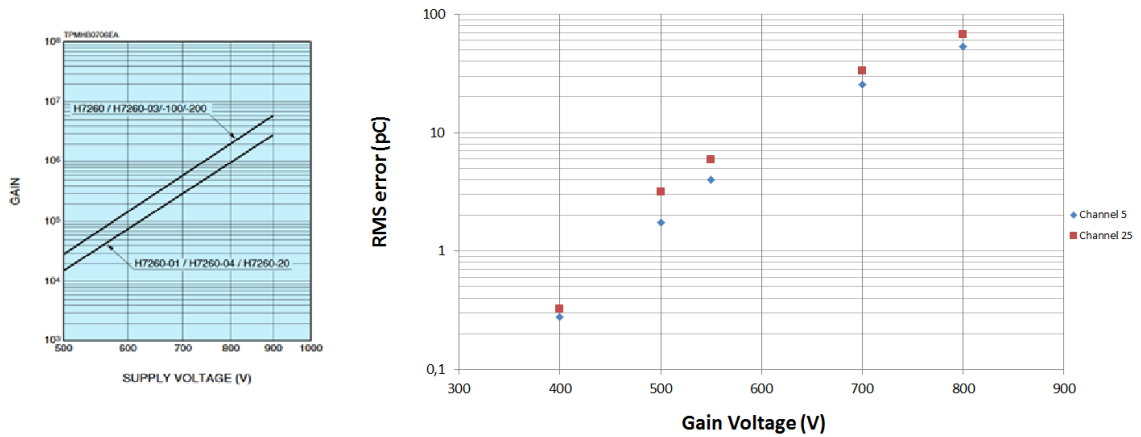
Figure 8.24: Gain voltage curve of the Hamamatsu H7260 PMT array (left) and RMS error of channels 5 and 25 (right).

Regarding the background, the detector manufacturer [135] specifies a dark current per channel typically of 0.2 nA and maximum of 2 nA. With our integration time of 10 ms, the contribution to the background would be 20 pC at maximum, which is clearly inferior to the offset voltage seen in Fig. 8.23. Since the readout electronics background is negligible, as it has an auto-zero functionality, and the chamber reflections are greatly reduced with the anti reflective coating, we think that the radiation background is the main culprit of both the high offset and RMS noise. This contribution to the signal is mainly generated by the gamma rays and neutrons which interact with the optical materials producing photons which travel through the optical system to the photocathode where they are later converted to electrons and enter into the dynode amplification system. This radioluminescence is isotropic and uniform, with a photon yield depending on the radiation type and energy and the optical material.

The profiles of the second run were obtained at fixed current (1.1 μA) and constant gain (550 V). Some of the results are summarised in Fig. 8.25. Only one profile is identified from the four represented, since we were on the verge of the beam detection, however, the effect of the pressure and integration time are clearly seen. Regarding the offset of the background, no clear change is observed when the pressure is varied, however the effect of changing the integration time is linear. In the last series of measurements the final steerer of the line was changed between different positions many times (within the allowable limits) and the beam center is obtained

145
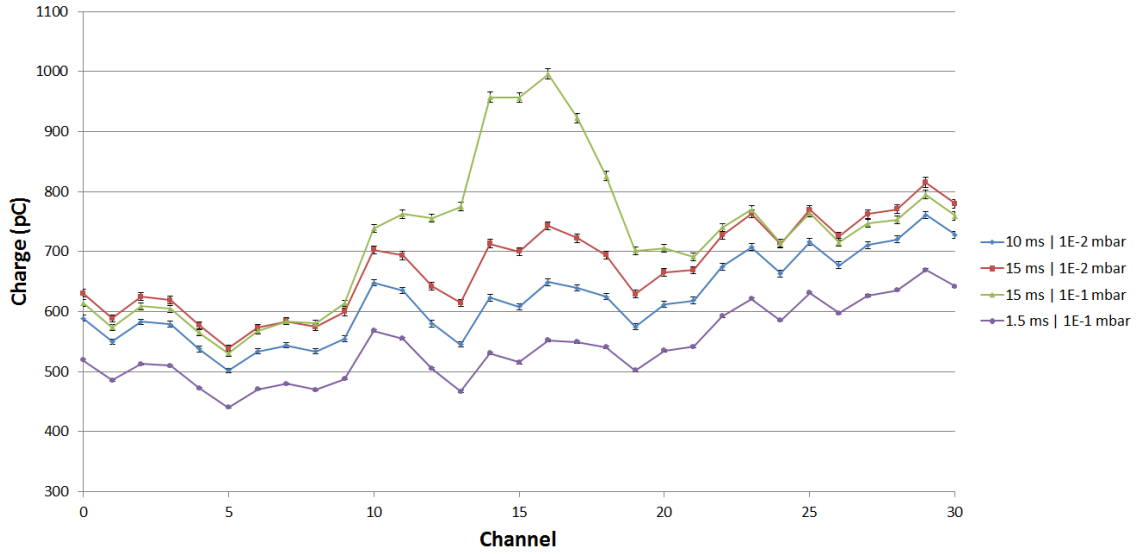
Figure 8.25: Profiles measured under different pressures (10^{-2} and 10^{-1} mbar) and different integration times (1.5, 10 and 15 ms).

using a gaussian fitting algorithm. The results of the position of the beam center as a function of the magnet current are plotted in Fig. 8.26, where we can see that the repetitibility is quite good. However, a linear behaviour should be expected, since we were only steering the beam, but is clearly not the case, as the trend seems to be parabolic. We have attributed this behaviour to the passage of the beam out of the center of the two quadrupoles, which were located downstream along the accelerator line.

Although electrical checks did not show any abnormal behaviour, we were not even able to record any image with the intensified spectrometer apart from black pictures. A fast disassembly was done and the camera was found to be working properly, but the intensifier did not show any kind of signal, not even noise from itself or from the radiation background. The intensifier itself will be put under investigation and characterization of its current state before later measurements will be done in the future, however, comparing the parameters used for the different measurements campaigns in which it has been used, it has been observed that as the time passed higher polarization voltages and integration times should be used in order to obtain good profiles, hence sensitivity degradation due to aging of the photocathode is the main suspect at the moment.
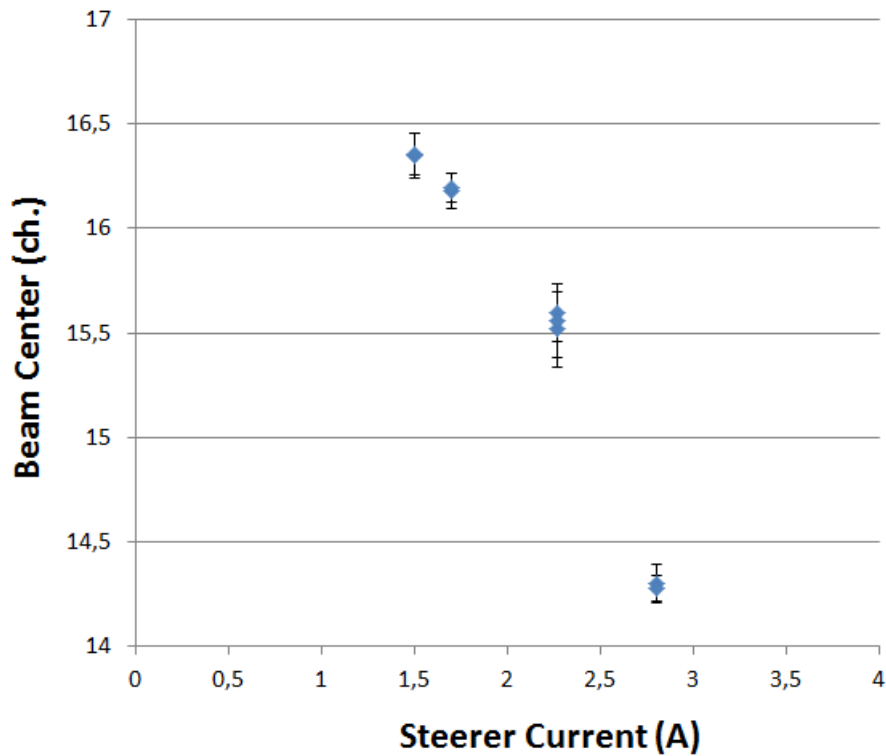
Figure 8.26: Beam position as a function of the steering current.

Finally, we switched on the lithium filled oven and started to slowly rise the temperature at a rate of 13 °C/min. During the ramp up the temperature of both the resistor and oven, as well as the pressure in the chamber between windows were continuously monitored. Beam current scans from 1 to 10 μA were performed every 50 °C, up to a oven temperature of 520 °C. During the experiment the PMT polarization voltage and integration times were kept high, but no beam profile could be seen even at the highest settings. The conditions in the experiment were comparable to the ones that will be in DONES, with a lithium vapor density more than four orders of magnitude higher in our experiment than in the DONES TIR, although the current in our experiment is $1.25 \cdot 10^4$ times smaller, but the cross section is slighly higher in our case due to the small velocity of our 15.5 MeV protons compared to the 40 MeV deuterons of DONES.

Even though interesting results have been obtained regarding the influence of the radiation background on the FPM and the lack of light emitted by the lithium, we were unable to measure any spectra with the intensified spectrometer. The device was examined again in the CIEMAT laboratory, where several test were done. The

test didn't show any abnormal electrical behaviour in neither the MCP nor the control electronics. What was observed comparing the measurements done in the past with the same unit was a tendency of increasing the gain to achieve the same performance, confirming the aging and lost of sensitivity of the intensifier.

Chapter 9

Conclusions

In the past years Fluorescence Profile Monitor have been under extensive study and have been proven to be a very useful diagnostics for particle accelerators. Our aim with this work was to push a step forward the developments on FPM, focusing on its applications in high current power hadron accelerators.

Chapter 5 is where the main sources of profile distortion due to the fluorescence process itself have been discussed. Whilst the effect of the electrons has to be studied in each particular case to take into account, as its generation and accumulations as they are very dependent on the beam current, energy and vacuum pressure, the distortion due to the particle movement is specially noticeable at small beam sizes in the order of millimiters or less, always depending on the lifetime of the transitions, which are typically less than microseconds. From the two proposed methods, although they require good knowledge of the spectrum and atomic/molecular transitions involved, the most directly applicable to a real life example is the one based on the profile deconvolution, whilst the other gives a quick estimation on how much our profile will change due to the movement of the excited particles. Both methods are based in the same hypothesis, and the rms of the propagated beam is the same in both cases. It is important to remark that the assumptions made during the derivation of the theory should be checked when applying this results.

In Chapter 6 an overview of the results obtained during the summer 2017 measurement campaign during the commissioning and characterization of the LIPAc injector is given. These measurements were done in the most basic configuration of the

injector, with no solenoids involved, only the plasma chamber, the accelerating column and a diagnostics chamber. During the measurements the total accelerating voltage was kept constant, but different parameters like the beam current or the intermediate electrode voltage were scanned. The FPM were very useful during the operation of the machine, and the analysis of the data allowed us to identify a misalignment of the electrodes which was latter corrected. Inconsistencies were found when comparing the FPM profiles with the ones obtained with the Emittance Measurement Unit, as well as a non symmetric profile which did not correspond to the radial symmetry of the system nor be attributed to the other species present in the beam. It has been found recently that the magnets installed for suppressing secondary electrons at the beam dump were influencing the beam more than what was expected. However, further work could be done regarding the spectral analysis with a more sensitive spectrometer, since if we were able to measure the light coming from the lines associated to spin flip transitions we could directly measure the electron distribution in the beam core and gain insight on the space charge compensation process.

Chapter 7 deals with the design of the profile monitors of the DONES HEBT. Regarding the interceptive profile monitors, a wire grid based approach has been selected, with 48 channels per profile at every position. Simulations have predicted safety duty cycles shorter than 1 % at full current, so their use will be limited to the commissioning and tune of the machine. Beam dynamics simulations are still ongoing since the definitive layout of the SRF linac is not fixed, thus the final wire spatial distribution at each position of the line has not been decided yet, but the overall diagnostic design idea is to use as few different chambers and actuators models as possible to reduce the problems associated with logistics and maintenance. In the case of the non interceptive profile monitors we started the work with the fluorescence based ones since they are more robust to the space charge problems, but the use of ionization based ones has not been discarded yet. During every step of the design feedback from the LIPAc commissioning is taken into account. At the moment a design based on the use of optical fibers has been proposed for the high radiation areas. In places where the enviroment is not that harsh the detector can be placed adjacent to the beam pipe, like in the typical implementations of this kind of profile monitors.

The next steps regarding the profile monitors for DONES are twofold: 1) continue the development of the regular profile monitors, both interceptive and non-interceptive, and 2) testing the multimode fiber array with SiPM and the intensifier

based camera developed for the high radiation areas, with a special focus in studying the influence of the high radiation background in the noise level of the optical system. Moreover, information coming from the LIPAc comissioning will still be very valuable, specially during operation at high current with deuterons, where the radiation background is the highest.

Lastly, in order to evaluate the impact of lithium vapor on the FPM and to measure the proportion between the different spectral lines of the emitted light an experiment was designed, built and performed, all of which is described in chapter 8. The whole system was designed from scratch and built using both off-the-self and custom-made parts according to the specifications required by the CNA. Extensive tests and simulations were done prior to the experiment in order to assess the good performance of the vacuum window, the lithium oven and the electronic system. Two fluorescence detectors were used: an intensified spectrograph and the LIPAc prototype using a PMT array.

The experiment was assembled and took place within four days at CNA. Preliminary tests of both the detectors and ancillary systems were successful, but once the beam was on we were only able to acquire profiles with the PMT array. We suspect that the problem with the intensified spectrograph lies within the PMT, because not even noise coming from the radiation background was detected, even at maximum settings (gain and duty cycle), although signal could be detected if exposed to ambient light. After the experiments we compared the parameters required to obtain a good profile of the several times that the image intensifier was used, realising that the gain and duty cycle had to be increased as the time passed, thus confirming the degradation of the the MCP.

Nevertheless, interesting results had been obtained with the PMT array. Apart from comparing the minimum gains and integration times with the ones obtained in LIPAc (after taking into account the difference in the current, pressure and cross section), we could do extensive tests to the new and updated FPM control system and, most important, we were able to have a rough estimation of the impact that the radiation will play in the future FPM located in the high radiation areas of DONES, which was previously underestimated.

As a wrap up conclusion, this work contains two well defined part: the first includes the basis of theoretical and practical aspects of the fluorescence profile

monitors as well as a theory to take into account distortions due to the movement of excited particles before emission. The second part presents the experimental work that has been carried out in the frame of this theses, including the participation in the LIPAc comissioning, the design of an experiment to measure the spectral light of lithium vapor and different gases and the preliminary design of the profile monitors for the DONES HEBT. The next steps of the work will be focused on pushing forward the limits of the Fluorescence Profile Monitors to measure the transverse beam profile in very high radiation areas, whilst continuing the development of standard profile monitors for the parts of the accelerator with less strict requirements.

Appendix A

Spectral measurements of 100 keV Deuteron fluorescence
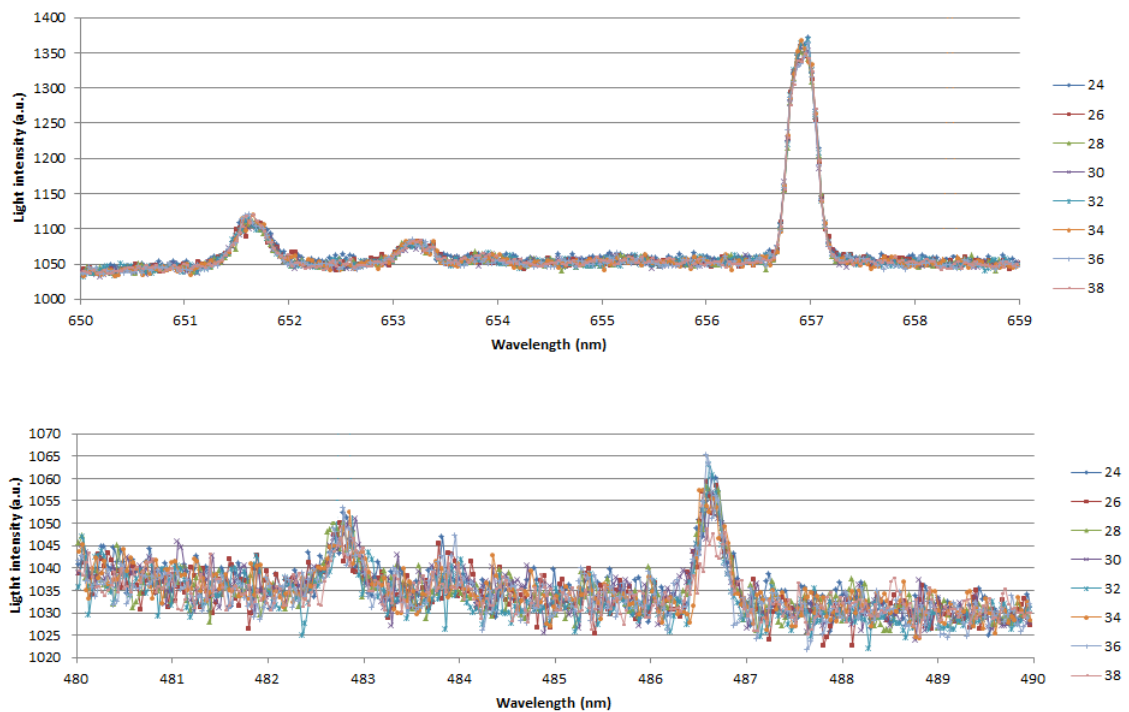
Figure A.1: Spectrum measurement of the D_α (top) and D_β (bottom) lines for different Intermediate Electrode voltages (in kV).
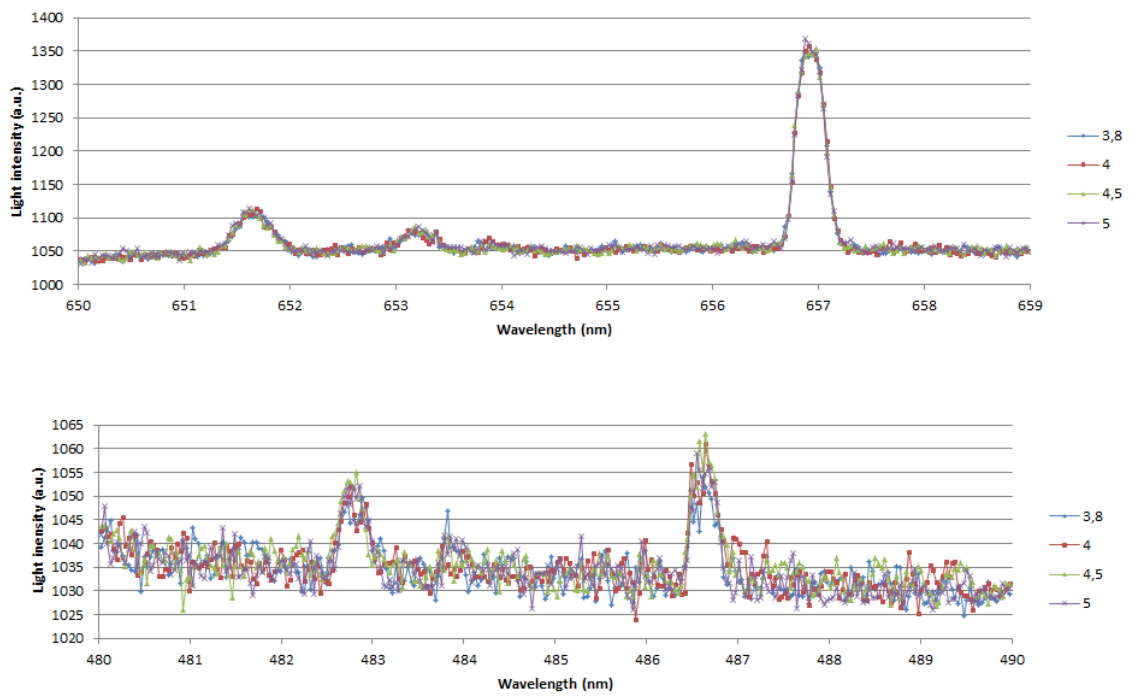
Figure A.2: Spectrum measurement of the D_α (top) and D_β (bottom) lines for different Repeller Electrode voltages (in kV).

Figure A.3: Spectrum measurement of the D_α line for different beam currents (in mA).
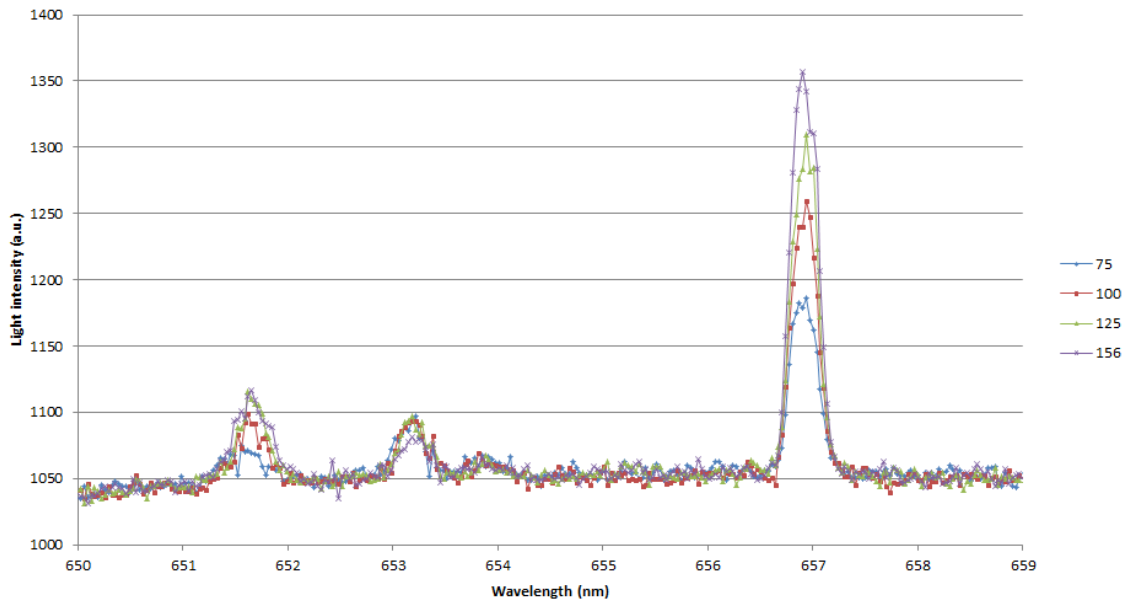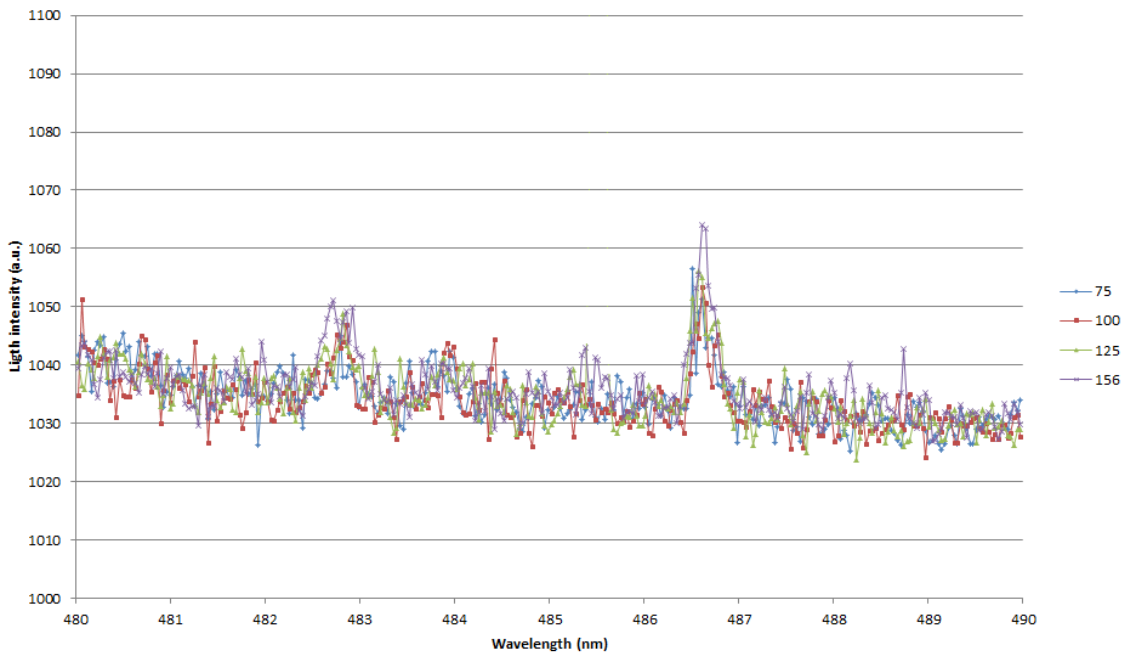

Figure A.4: Spectrum measurement of the D_β line for different beam currents (in mA).
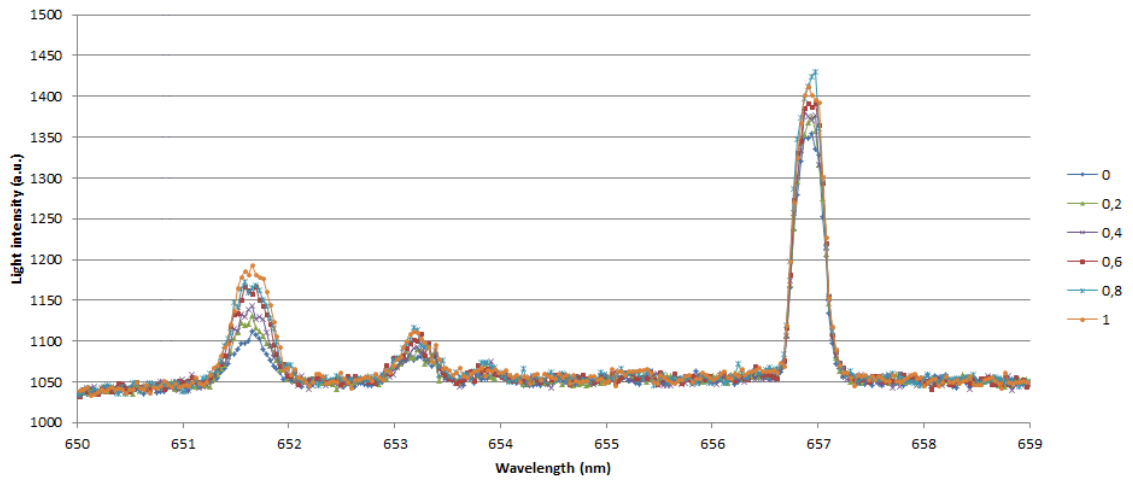
Figure A.5: Spectrum measurement of the D_α line for different Kr flow (in sccm).
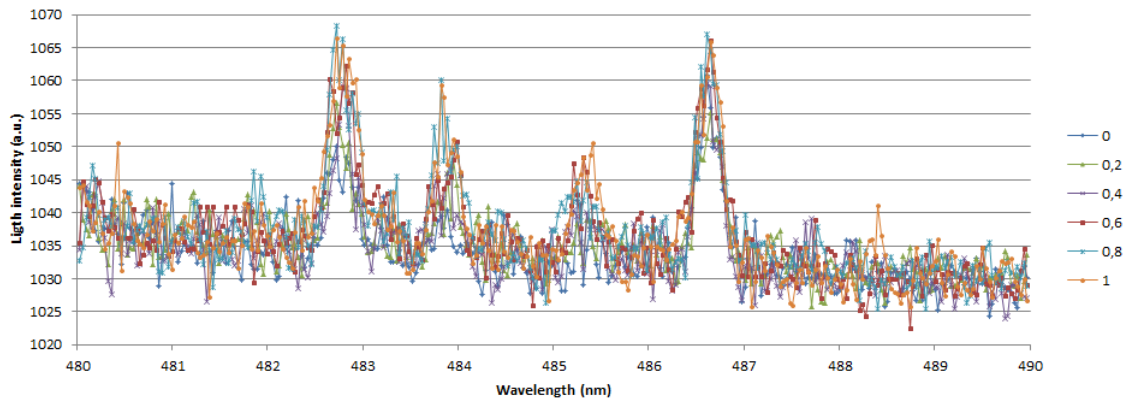
Figure A.6: Spectrum measurement of the D_β line for different Kr flow (in sccm).
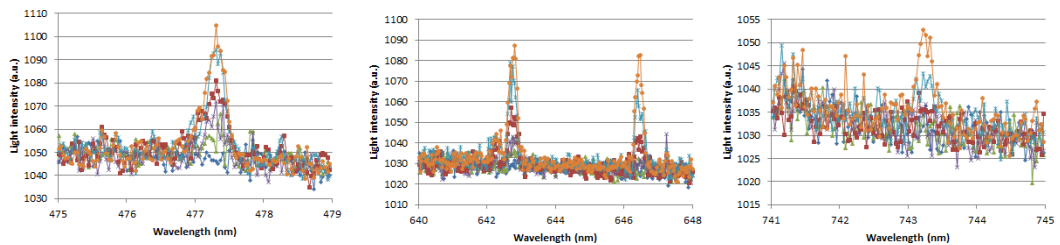
Figure A.7: Change of the four selected Krypton lines with respect to the injected flow (sccm).

Appendix B

Control system detailed description

In order to interface the PC with the low level components and provide the required signal three interface boards and two auxiliary boards were manufactured. The communication between each board and the PC was done using a serial port using USB to Serial bridge by FTDI [141]. In order to stick to open source platforms it was decided to use the ATMega328 [142], an inexpensive 8-bit microcontroller which features UART, SPI and I2C communication pheriferals, a six channel ADC and six PWM channels.

The first board manages the communication between the PC and the vacuum system and the multiplexer. Vacuum components are activated and deactivated using relays driven by 2N3904 transistors directly connected to the ATMega328, due to the maximum current limitation on the outputs of 40 mA. The pressure read in the vacuum window is done using the MPX4250AP piezoelectric pressure sensor. The fifteen relay multiplexer is controlled with two serial to parallel 8 bit registers with a transistor driven output. Both board are pictured in Fig. B.1.

The second control board is dedicated to the oven temperature control. Temperature reads from the liquid lithium and resistors are obtained using two K-type thermocouple input channels, implemented using the MAX6675 Cold Junction Compensated thermocouple to digital converter with 12 bits resolution. Power on the 550W resistor is controlled with a Crydom D2425 solid state relay. A PID has been implemented to keep the oven temperature stable around the desired value, which outputs an ON-OFF state for the relay. The PWM output signal frequency is high
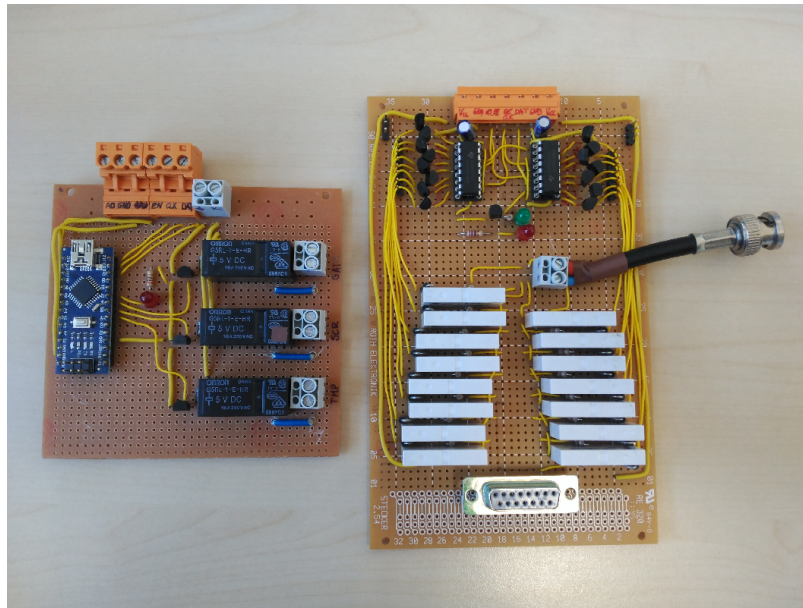
Figure B.1: Vacuum board (left) and multiplexer (right).

enough to emulate an variable analog current due to the slow response time of the system (which acts as a low pass filter). However, preliminary test showed a unstable behaviour of the system due to the long delay times, and for the experiment an open loop control was used where the period and duty cycle of the signal were manually introduced.
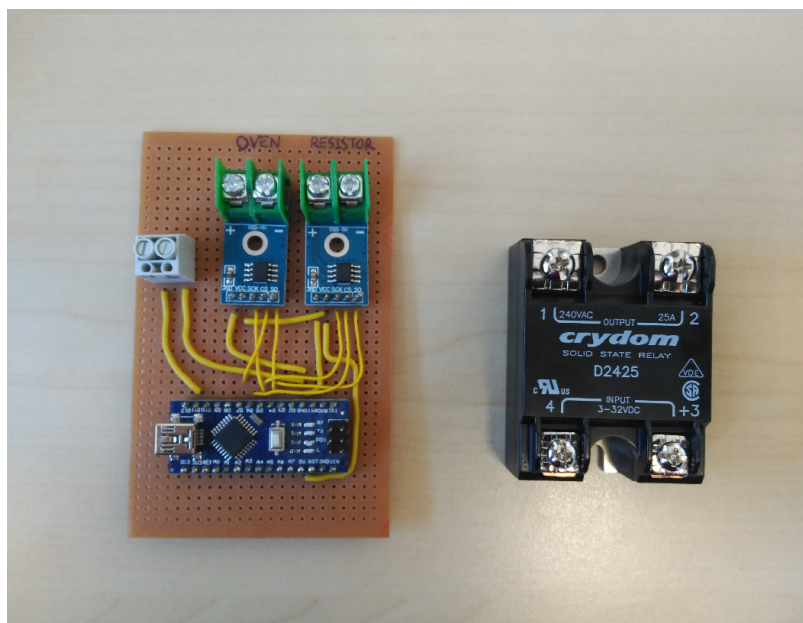
Figure B.2: Oven board and Solid State Relay.

The last board is dedicated to control the gas injection and the MCP. This time a 2 channel DAC (MCP4822) is controlled by the ATMega328 with using the SPI protocol. The two outputs are multiplied to obtain the required voltage ranges (0-10 V for the gas valve and 0-5 V for the MCP gain) using an operational amplifier with independently adjustable feedback network. The microcontroller itself is capable of creating the square wave needed for the MCP gating with a frequency higher than the maximum frequency accepted by the intensifier, which is 14 kHz. The signal is transformed into a 50 Ohm signal using an auxiliary board which also serves as an interface with the timing system. Due to the CW beam the synchronization capability with an external timing system has been disabled for our experiment.
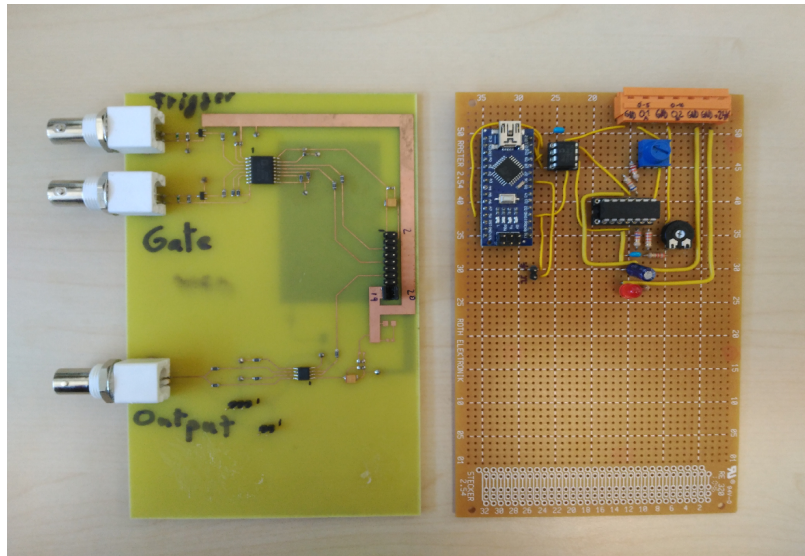
Figure B.3: Auxiliary timing board (left) and MCP control board (right).

Bibliography

[1] A. Ibarra. A neutron source for fusion: The DONES Project. *CERN seminar, Geneva, Switzerland*, 2019.

[2] Hamamatsu Photonics. `https://www.hamamatsu.com/`.

[3] H. Tawara, Y. Itikawa, H. Nishimura, and M. Yoshino. Cross Sections and Related Data for Electron Collisions with Hydrogen Molecules and Molecular Ions. *Journal of Physical and Chemical Reference Data*, 19(3):617–636, 1990.

[4] J.D. Jackson. *Classical Electrodynamics*. Wiley, 1975.

[5] Horiba Scientific. `http://www.horiba.com/scientific/`.

[6] O. Nomen. D. Sanchez. Preliminary Design Description Document (DDD) of the High Energy Beam Transport line (HEBT) of the Accelerator System (AS). Technical report, EUROFusion-WPENS, 2019. EFDA_D_2N8VS4.

[7] F. Ogando et al. Nuclear analysis of the Accelerator System of the ENS. Technical report, EUROFusion-WPENS, 2016. EFDA_D_2KW2MA.

[8] C. Oliver. Private communication.

[9] Vertilon. `https://vertilon.com/`.

[10] D.E. Gray. *American Institute of Physics Handbook*. McGraw-Hill, 1957.

[11] A. R. Steere. *A timeline of major particle accelerators*. MSc Thesis. 2005.

[12] TIARA. `http://www.accelerators-for-society.org`.

[13] Helmut Wiedemann. *Particle Accelerator Physics*. Graduate Texts in Physics. Springer, 2015.

[14] CERN Accelerator School. `http://cas.web.cern.ch/cas`.

[15] Bernhard H Wolf. *Handbook of ion sources*. CRC Press, 1995.

[16] Eurostat. `https://ec.europa.eu/eurostat/`.

[17] J. Knaster et al. IFMIF the European Japanese efforts under the Broader Approach agreement towards a Li(d,xn) neutron source: Current status and future options. *Nuc. Mat. and Energy*, 9:46–54, 2016.

[18] P Vladimirov and Anton Möslang. Comparison of material irradiation conditions for fusion, spallation, stripping and fission neutron sources. pages 233–237, 08 2004.

[19] A. Ibarra et al. A stepped approach IFMIF/EVEDA towards IFMIF. *Fusion Sci. Technol.*, 66(1):252–259, 2014.

[20] P. Cara et al. The Linear IFMIF Prototype Accelerator design development under the European-Japanese colaboration. *Proceedings of IPAC2016, Korea*, 2016.

[21] Y. Okumura et al. Operation and commissioning of IFMIF LIPAc injector. *Proceedings of ICIS2015, New York, USA*, 2015.

[22] A. Pisen et al. IFMIF-EVEDA RFQ design. *Proceedings of EPAC2008, Genoa, Italy*, 2008.

[23] I. Podadera et al. The Medium Energy Beam Transport line (MEBT) of IFMIF/EVEDA LIPAc. *Proceedings of IPAC2011, Bilbao, Spain*, 2011.

[24] H. Dzitko et al. Design and manufacturing status of the IFMIF-LIPAc SRF Linac. *Proceedings of IPAC2015, Richmond, USA*, 2015.

[25] J. Marroncle et al. IFMIF-LIPAc Diagnostics and its challenges. *Proceedings of IBIC2012, Tsukuba, Japan*, 2012.

[26] Peter Forck. *Lecture notes on Beam Instrumentation and Diagnostics*. JUAS Lecture notes. GSI, 2016.

[27] Peter Strehl. *Beam Instrumentation and Diagnostics*. Particle Accelerator and Detection Series. Springer, 2006.

[28] E. J. Sternglass. Theory of Secondary Electron Emission by High-Speed Ions. *Phys. Rev.*, 108:1–12, Oct 1957.

[29] H. Bethe and J. Ashkin. E. Segre (editor). *Experimental Nuclear Physics*. J. Wiley, 1953.

[30] H C Appelo. The zero-flux DC current transformer: a high precision bipolar wide- band measuring device. *IEEE Trans. Nucl. Sci.*, 24(3):1810–11, 1977.

[31] Robert E. Shafer. Beam position monitoring. *AIP Conference Proceedings*, 212(1):26–58, 1990.

[32] G.F. Knoll. *Radiation Detection and Measurement*. Wiley, 2000.

[33] E. Gütlich et al. Light yield, imaging properties and spectral response of inorganic scintillators under intense ion irradiation. *Proceedings of BIW2010, Santa Fe, USA*, 2010.

[34] P. Forck. Minimal invasive Beam Profile Monitors for high intense ion beams. *Proceedings of IPAC2010, Kyoto, Japan*, 2010.

[35] G. Kube. Review of synchrotron radiation based diagnostics for transverse profile measurements. *Proceedings of DIPAC2007, Venice, Italy*, 2007.

[36] V. L. Ginzburg. Transition Radiation and Transition Scattering. *Physica Scripta*, 1982(T2A):182, 1982.

[37] M. Zhang. Emittance formula for slit and pepper-pot measurements. *FERMILAB-TM-1988*, 1996.

[38] S Hancock, Shane Rupert Koscielniak, and M Lindroos. Longitudinal phase space tomography with space charge; rev. version.

[39] A. V. Feschenko. Methods and instrumentation for Bunch Shape Measurements. *Proceedings of PAC2001, Chicago, USA*, 2001.

[40] D. Doyle. Optical materials. *3rd Europa Jupiter system mission instrument workshop, ESA ESTEC*, 2010.

[41] J.J. Livingood. *Principles of Cyclic Particle Accelerators*. Van Nostrand, 1961.

[42] J. S. Fraser. Developments in non-destructive beam diagnostics. *IEEE Trans. Nucl. Phys*, NS-82(3), 1989.

[43] D. D. Chamberlin. Noninterceptive transverse beam diagnostics. *IEEE Trans. Nucl. Phys*, NS-82(3), 1989.

[44] K. Zankel B. Vosicki. The sodium courtain beam profile monitor of the ISR. *IEEE Trans. Nucl. Phys*, NS-22(3), 1975.

[45] F. Becker. Beam induced fluorescence monitors. *Proceedings of DIPAC2011, Hamburg, Germany*, 2011.

[46] L. Rezzonico. A profile monitor using residual gas. *Proceedings of Cyclotrons1989, Berlin, Germany*, 1989.

[47] D. P. Sandoval et al. Fluorescence-based video profile for beam diagnostics: theory and experience. *Proceedings of BIW1993, Santa Fe, United States*, 1993.

[48] T. Tsang et al. Optical beam profile monitor and residual gas fluorescence at the RHIC polarized hydrogen jet. *Rev. Sci. Inst.*, 79:105103–12, 2008.

[49] M.A Plum, E Bravin, J Bosser, and R Maccaferri. N2 and Xe gas scintillation cross-section, spectrum, and lifetime measurements from 50 MeV to 25 GeV at the CERN PS and Booster. *Nuclear Instruments and Methods in Physics Research Section A: Accelerators, Spectrometers, Detectors and Associated Equipment*, 492(1):74 – 90, 2002.

[50] A. Variola et al. Characterization of a non-destructive beam profile monitor using luminescent emission. *Phys. rev. ST-AB*, 10:1 – 14, 2007.

[51] A. Bank P. Forck. Residual gas fluorescence measurements at the GSI UNILAC. *Proceedings of EPAC2002, Paris, France*, 2002.

[52] J. Dietrich. Non-destructive beam position and profile measurements using light emitted by residual gas in a cyclotron beam line. *Proceedings of EPAC2008, Genoa, Italy*, 2002.

[53] J. M. Carmona, I. Podadera, A. Ibarra, A. Bocci, M. C. Jiménez-Ramos, J. García López, Z. Abou-Haïdar, M. A. G. Álvarez, and B. Fernández. Measurements of noninterceptive fluorescence profile monitor prototypes using 9 MeV deuterons. *Phys. Rev. ST Accel. Beams*, 15:072801, Jul 2012.

[54] P. Ausset et al. Optical Transverse Profile measurements for high power proton beams. *Proceedings of EPAC2002, Paris, France*, 2002.

[55] H. Reichau et al. Estimation of profile width in hybrid ion beam tomography. *Proceedings of BIW2010, Santa Fe, US*, 2010.

[56] F. Becker et al. Beam induced fluorescence monitors for FAIR. *Proceedings of IPAC2012, New Orleans, US*, 2012.

[57] R. Gobin et al. Final design of the IFMIF injector at CEA/Saclay. *Proceedings of IPAC2013, Shanghai, China*, 2013.

[58] F. Senee et al. Increase of IPHI beam power at CEA Saclay. *Proceedings of IPAC2018, Vancouver, Canada*, 2018.

[59] B. Bolzon et al. Beam diagnostics of an ECR ion source on LIPAc injector for prototype IFMIF beam accelerator. *Fusion Engineering and Design*, 2018.

[60] T. J. Shea. Overview and status of the diagnostics for the ESS project. *Proceedings of IBIC2017, Grand Rapids, US*, 2017.

[61] S. Cao. Optical system of Beam Induced Fluorescence monitor toward MW beam power at the J-PARC neutrino beamline. *Proceedings of IBIC2018, Shanghai, China*, 2018.

[62] L. Rossi et al. The High Luminosity challenge: potential and limitations of high intensity, high brightness beams in the LHC and its injectors. *Proceedings of HB2014, East-Lansing, US*, 2014.

[63] S. Udrea et al. Development of a fluorescence based gas sheet profile monitor for use with electron lenses: optical system design and preparatory experiments. *Proceedings of IBIC2017, Grand Rapids, US*, 2017.

[64] H.D. Zhang et al. 3D Density Scans of a Supersonic Gas Jet for Beam Profile Monitoring. *Proceedings of IBIC2016, Oxford, UK*, 2016.

[65] E. Bravin. Overview of imaging sensors and systems used in beam instrumentation. *Proceedings of IBIC2013, Oxford, UK*, 2013.

[66] James R Janesick. *Scientific charge-coupled devices*, volume 83. SPIE press, 2001.

[67] Hubert K Burke and Gerald J Michon. Charge injection imaging: Operating techniques and performances characteristics. *IEEE Journal of Solid-State Circuits*, 11(1):121–128, 1976.

[68] M. Bigas, E. Cabruja, J. Forest, and J. Salvi. Review of CMOS image sensors. *Microelectronics Journal*, 37(5):433 – 451, 2006.

[69] Hamamatsu Photonics. MCP assembly. technical information. Technical report, Hamamatsu Photonics, 2006.

[70] F. Becker et al. Beam Induced Fluorescence Monitor & Imaging Spectrography with different working gases. *Proceedings of DIPAC2009, Basel, Switzerland*, 2009.

[71] Hamamatsu Photonics. Optosemiconductor Handbook. Technical report, Hamamatsu Photonics, 2016.

[72] Hamamatsu Photonics. Photomultiplier Tubes. principles and Applications. Technical report, Hamamatsu Photonics, 2007.

[73] J. M. Carmona. *Caracterizacion y Analisis de Iones en Plasmas de TJ-II mediante Espectroscopia Activa por Intercambio de Carga*. PhD Thesis. 2008.

[74] F. Senee et al. Beam Species fraction measurements using Doppler shift method with Fujikura fiberscope for IFMIF-EVEDA injector. *Proceedings of DIPAC2011, Hamburg, Germany*, 2011.

[75] T. Buzug. *Computed Tomography*. Springer, 2008.

[76] C. Wagner et al. First measurements with the test stand for optical beam tomography. *Proceedings of DIPAC2011, Hamburg, Germany*, 2011.

[77] V. Dudnikov et al. Residual Gas Beam Profile Monitors for intense beams in transfer lines. *Proceedings of IPAC2017, Copenhagen, Denmark*, 2017.

[78] J.W. Goodman. *Introduction to Fourier Optics*. McGraw-Hill physical and quantum electronics series. W. H. Freeman, 2005.

[79] C. Cohen-Tannoudji, B. Diu, and F. Laloe. *Quantum Mechanics*. Quantum Mechanics. Wiley, 1991.

[80] R.L. Brooks. *The Fundamentals of Atomic and Molecular Physics*. Undergraduate Lecture Notes in Physics. Springer New York, 2014.

[81] J.J. Sakurai and J. Napolitano. *Modern Quantum Mechanics*. Addison-Wesley.

[82] M. Alonso, H. Valk, and J.M. Martin. *Mecanica Cuantica: fundamentos y aplicaciones*. Manual Universitario. Ediciones Universidad de Salamanca, 2009.

[83] B. Pottin. *Etude d'un profileur optique de faisceaux intenses de protons par absorption laser*. PhD Thesis. 2002.

[84] M. Reiser. *Theory and design of charged particle beams*. Wiley series in beam physics and accelerator technology. Wiley, 1994.

[85] R. Ferdinand et al. Space-charge neutralization measurement of a 75-keV, 130-mA hydrogen ion beam. *Proceedings of PAC1997, Vancouver, Canada*, 1997.

[86] J. L. Lemaire et al. Self-consistent effects of space charge compensation on intense ion beams. *Proceedings of LINAC1996, Geneva, Switzerland*, 1996.

[87] Y. D. et al. Wang. Analysis of final-state momentum distributions of ionization products in ion-atom collisions. *Phys. Rev. A*, 53:3278–3286, May 1996.

[88] F. Becker et al. Beam induced fluorescence profile monitoring for targets and transport. *Proceedings of HB2012, Beijing, China*, 2012.

[89] S. Udrea et al. Preparatory work for a Fluorescence based Profile Monitor for an electron lens. *Proceedings of IBIC2016, Barcelona, Spain*, 2016.

[90] Th. Weber et al. Kinematically complete investigation of momentum transfer for single ionization in fast proton-helium collisions. *Journal of Physics B: Atomic, Molecular and Optical Physics*, 33(17):3331, 2000.

[91] D. Hoffman, B. Singh, and J.H. Thomas. *Handbook of Vacuum Science and Technology*. Elsevier Science, 1997.

[92] F J Sacherer. RMS envelope equations with space charge. (CERN-SI-INT-DL-70-12):17 p, Nov 1970.

[93] Pierre M Lapostolle. Possible emittance increase through filamentation due to space charge in continuous beams. (CERN-ISR-DI-71-2. ISR-DI-71-2), 1971.

[94] Tracewin. `http://irfu.cea.fr/en/Phocea/Page/index.php?id=780`.

[95] B. Bolzon et al. Beam diagnostics of the LIPAc injector with a focus on the algorithm developed for emittance data analysis of high background including species fraction calculation. *Proceedings of IBIC2015, Melbourne, Australia*, 2015.

[96] Edmund Optics. `https://www.edmundoptics.com/`.

[97] Proxitronic. `http://www.proxivision.de/`.

[98] Schneider Kreuznach. `https://schneiderkreuznach.com/en`.

[99] Thermo Fisher Scientific. `https://www.thermofisher.com/`.

[100] National Instruments. `http://www.ni.com/`.

[101] STMicroelectronics. `http://www.st.com/`.

[102] B. Bolzon. Private communication.

[103] Fujikura. `https://www.fujikura.co.uk/`.

[104] A. V. Phelps. Cross Sections and Swarm Coefficients for H^+, H_2^+, H_3^+, H, H_2 and H^- in H_2 for energies from 0.1 eV to 10 keV. *Journal of Physical and Chemical Reference Data*, 19(3):653–675, 1990.

[105] NIST. `https://physics.nist.gov/PhysRefData/ASD/lines_form.html`.

[106] N. Bazin et al. Status of the IFMIF LIPAc SRF linac. *Proceedings of SRF2017, Lanzhou, China*, 2017.

[107] E. Wakai et al. Engineering validation for Lithium target facility of the IFMIF in the IFMIF/EVEDA project. *Nuclear Materials and Energy*, 9:278–285, 2016.

[108] I. Podadera et al. Detailed engineering design of HEBT diagnostics. Technical report, EUROFusion-WPENS, 2019. EFDA_D_2N3TLB.

[109] C. Oliver. CIEMAT contribution to Beam Dynamics preliminary design analysis. Technical report, EUROFusion-WPENS, 2017. EFDA_D_2MM3WG.

[110] J. Horne. Preliminary RH procedures for the maintenance of components in the TIR. Technical report, EUROFusion-WPENS, 2017. EFDA_D_2MSH8V.

[111] K. Kondo et al. Dose Rate Analyses for the High Energy Beam Transport Section of IFMIF. *Nuclear Science and Technology*, 62(1):226–232, 2012.

[112] T. Matyas. Development of a data base for common Rad Hard devices systems and sensors for the design of RHE. Technical report, EUROFusion-WPENS, 2017. EFDA_D_2N9KLH.

[113] Y. Qiu. Report on beam position and beam shape assessment. Technical report, EUROFusion-WPENS, 2017. EFDA_D_2MCAEB.

[114] M. Sapinski et al. Application of machine learning for the IPM-based profile reconstruction. *Proceedings of HB2018, Daejeon, Korea*, 2019.

[115] R. Ferdinand et al. Test of wire sublimations very close to SPIRAL2 superconducting cavity. *Proceedings of LINAC08, Victoria (BC), Canada*, 2008.

[116] SRIM. `http://www.srim.org/`.

[117] V.P. Budaev et al. Tungsten recrystallization and cracking under ITER-relevant heat loads. *Journal of Nuclear Materials*, 463:237 – 240, 2015.

[118] P. Mateljak. T. Tádic. Industry contribution to preliminary test acceptance procedures for components of the TIR after the installation. Technical report, EUROFusion-WPENS, 2017. EFDA_D_2MQ6YL.

[119] I. Podadera et al. Shape of the diagnostics to be integrated in the 3DMU. Technical report, EUROFusion-WPENS, 2018. EFDA_D_2MS2MW.

[120] T. Iida et al. Effects of 14-MeV Neutron Irradiation on Optical Components for Fusion Diagnostics. *Nuclear Science and Technology*, 27(7):651–662, 2012.

[121] D. Bachiller-Perea. *Ion-irradiation-induced damage in nuclear materials: Case study of a-SiO2 and MgO*. PhD Thesis. 2016.

[122] C. Ito et al. Development of radiation-resistant optical fiber for application to observation and laser spectroscopy under high radiation dose. *Journal of Nuclear Science and Technology*, 51:944–950, 05 2014.

[123] C. Day. V. Hauer. Vacuum modelling: Vacuum preliminary design. Technical report, EUROFusion-WPENS, 2017. EFDA_D_2MMU6W.

[124] J. Egberts. *IFMIF-LIPAc Beam Diagnostics: Profiling and Loss monitoring systems*. PhD Thesis. 2012.

[125] Thorlabs. `https://www.thorlabs.com/`.

[126] Photonis. `https://www.photonis.com/`.

[127] Hamamatsu. `https://www.hamamatsu.com/resources/pdf/ssd/s13361-3050_series_kapd1054e.pdf`.

[128] Hamamatsu. `https://www.hamamatsu.com/resources/pdf/etd/II_TII0007E.pdf`.

[129] R. Varela et al. Preliminary assessment of beam profile monitors for IFMIF DONES. Technical report, EUROFusion-WPENS, 2017. EFDA_D_2MN9TH.

[130] K. Battes et al. Outgassing rate measurements of stainless steel and polymers using the difference method. *Journal of Vacuum Science & Technology A: Vacuum, Surfaces, and Films*, 33:021603, 03 2015.

[131] T. Kanemura, H. Kondo, T. Furukawa, Y. Hirakawa, E. Wakai, and J. Knaster. Analytical and experimental study of the evaporation and deposition rates from a high-speed liquid lithium jet. *Fusion Engineering and Design*, 122:176 – 185, 2017.

[132] F. Becker et al. Beam Induced Fluorescence Monitor - spectroscopy in Nitrogen, Helium, Argon, Krypton and Xenon gas. *Proceedings of BIW, Santa Fe, USA*, 2010.

[133] Centro Nacional de Aceleradores. `http://cna.us.es/`.

[134] U.S. Department of Health and Human services. `https://www.cdc.gov/`.

[135] Hamamatsu Photonics. `https://www.hamamatsu.com/`.

[136] Keithley. `https://uk.tek.com/keithley`.

[137] ANSYS. `https://www.ansys.com/`.

[138] Agilent Vacuum Technologies. `https://www.agilent.com/en/products/vacuum-technologies`.

[139] Pfeiffer Vacuum. `https://www.pfeiffer-vacuum.com/en/`.

[140] S. Timoshenko and S. Woirosk-Kriegher. *Theory of plates and shells*. McGraw-Hill, 1959.

[141] FTDI. `http://www.ftdichip.com/`.

[142] Microchip. `https://www.microchip.com/`.